



## **Terms and Conditions of Use of Digitised Theses from Trinity College Library Dublin**

### **Copyright statement**

All material supplied by Trinity College Library is protected by copyright (under the Copyright and Related Rights Act, 2000 as amended) and other relevant Intellectual Property Rights. By accessing and using a Digitised Thesis from Trinity College Library you acknowledge that all Intellectual Property Rights in any Works supplied are the sole and exclusive property of the copyright and/or other IPR holder. Specific copyright holders may not be explicitly identified. Use of materials from other sources within a thesis should not be construed as a claim over them.

A non-exclusive, non-transferable licence is hereby granted to those using or reproducing, in whole or in part, the material for valid purposes, providing the copyright owners are acknowledged using the normal conventions. Where specific permission to use material is required, this is identified and such permission must be sought from the copyright holder or agency cited.

### **Liability statement**

By using a Digitised Thesis, I accept that Trinity College Dublin bears no legal responsibility for the accuracy, legality or comprehensiveness of materials contained within the thesis, and that Trinity College Dublin accepts no liability for indirect, consequential, or incidental, damages or losses arising from use of the thesis for whatever reason. Information located in a thesis may be subject to specific use constraints, details of which may not be explicitly described. It is the responsibility of potential and actual users to be aware of such constraints and to abide by them. By making use of material from a digitised thesis, you accept these copyright and disclaimer provisions. Where it is brought to the attention of Trinity College Library that there may be a breach of copyright or other restraint, it is the policy to withdraw or take down access to a thesis while the issue is being resolved.

### **Access Agreement**

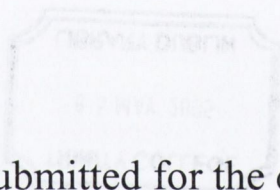
By using a Digitised Thesis from Trinity College Library you are bound by the following Terms & Conditions. Please read them carefully.

I have read and I understand the following statement: All material supplied via a Digitised Thesis from Trinity College Library is protected by copyright and other intellectual property rights, and duplication or sale of all or part of any of a thesis is not permitted, except that material may be duplicated by you for your research use or for educational purposes in electronic or print form providing the copyright owners are acknowledged using the normal conventions. You must obtain permission for any other use. Electronic or print copies may not be offered, whether for sale or otherwise to anyone. This copy has been supplied on the understanding that it is copyright material and that no quotation from the thesis may be published without proper acknowledgement.

# Issues Relating to the Application of Monolithic Tuneable Laser Diodes to Multi- Species Gas Detection

by

Richard P. Phelan



A thesis submitted for the degree of  
Doctor of Philosophy  
in the University of Dublin

Department of Physics  
Trinity College  
University of Dublin

February 2005

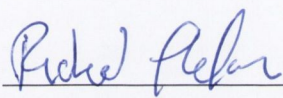




THOS  
7585

## *Declaration*

This thesis has not been submitted as an exercise for a degree in this or any other university. The work described is entirely my own, with exception of assistance and the collaborative work mentioned in the acknowledgements. I agree that Trinity College Library may lend or copy this thesis upon request.

A handwritten signature in blue ink, appearing to read "Richard Phelan", is written above a horizontal line.

Richard P. Phelan



## Summary

Tunable Diode Laser Absorption Spectroscopy (TDLAS) technology for gas sensing has had reliance on, and has benefited from, devices developed for the optical communications sector, namely distributed feedback laser diodes. The range in wavelengths of available DFB lasers coincides with absorption spectra of many gases of environmental and industrial interest. However, since the distributed feedback laser diode has a narrow wavelength tuning range, only one gas can be targeted without changing the laser. The objective of this thesis is to advance the strategic capability required to allow development of TDLAS multi-species gas detection systems using widely tuneable laser diodes recently developed for the telecommunication sector.

In this thesis, the application of widely tuneable laser diodes and a single frequency tuneable laser diode to trace gas detection in the near infrared region of the spectrum is reported.

High-resolution absorption measurements of the H<sub>2</sub>O line in the  $\nu_1+\nu_3$  band at 1.3928 $\mu\text{m}$  were made in the temperature range 296K - 1100K using an InGaAsP distributed feedback laser diode operating at 1.39 $\mu\text{m}$ . Spectral line shift as a function of temperature and pressure and line strength measurements on the water vapour line and their impact on the accuracy of optical absorption based gas sensing have been investigated. The results obtained were compared with values obtained from the HITRAN database and values reported in the literature for H<sub>2</sub>O. The results, facilitates H<sub>2</sub>O sensing in a non-standard temperature and pressure environment.

The application of a strongly gain coupled three-section distributed feedback laser cascade operating in the 1575-1585 nm region to multi-gas detection is reported for the first time. Simultaneous detection of Hydrogen Sulphide and Carbon Dioxide by dual wavelength operation of the three-section laser cascade is detailed. The device consisted of three cascaded sections ( $S_1$ ,  $S_2$  and  $S_3$ ) and an optical amplifier. Dual wavelength operation was achieved by biasing  $S_1$  and  $S_2$  above threshold. By precise dual independent wavelength tuning of the laser diode, both gases were simultaneously detected using wavelength modulation spectroscopy. The use of a strongly gain coupled laser in a dual wavelength mode has the potential to eliminate the need for multiple laser devices to simultaneously monitor more than one gas. However, when operating the device in a dual wavelength emission mode, thermal cross-talk between the lasing sections complicates somewhat the setting of the



emission wavelength of  $S_1$  and  $S_2$ . We have investigated stabilisation techniques to minimise the effect of this cross-talk.

The application of a sampled grating distributed Bragg reflector and modulated grating Y-branch laser as widely tuneable sources to a multi-species gas detection was investigated. In particular, the use of these widely tuneable laser diodes as sources in a multi-gas analysing system using wavelength modulation spectroscopy and second harmonic detection of acetylene hydrogen cyanide and ammonia has been investigated. The critical issues relevant to the application of such widely tuneable diode lasers to spectroscopic based high selectivity multi-gas sensing are outlined. The general emphasis of the work described here is not on detection limits but to selectively detect three gases with overlapping absorption bands.

A simple and straightforward method using multiple reference gases for wavelength characterisation and monitoring of the spectral emission from a SGDBR is next outlined. This method requires measurements of the gas absorption lines, an etalon trace and comparison of the separations between gas absorption lines and the corresponding separations from a database (HITRAN) to determine the emission wavelength of the SGDBR.

The results of the experiments reported in this thesis make a significant contribution to advancing the capability required to allow development of a TDLAS multi-species sensor. In addition it has been shown that the tuning behaviour of the SGDBR can be characterised using a combination of reference gases to provide unique wavelength identifiers to characterise the device and provide monitoring of the lasing wavelength.



## *Acknowledgements*

In the four years and that it took to complete the research presented in this thesis, it gives me great pleasure to thank the many people who made it all possible. I am extremely grateful for having had the opportunity to complete my thesis at Trinity College. The excellent facilities and many brilliant people that I have encountered here over the years have made it a most enjoyable experience.

Firstly I would like to acknowledge my supervisor Prof. John Donegan for his continuous work behind the scenes, to create and maintain a stimulating working environment in the semiconductor photonics group and for giving me the opportunity to come to Trinity and complete this Ph.D.

It gives me great pleasure to acknowledge Dr Vincent Weldon and Mick Lynch, who helped set out the goals for my research and gave constructive feedback along the road. Their combined experience in gas sensing and photonics always formed a reliable touchstone for new ideas to which I am indebted. The generosity with which Vincent and Mick gave of their time and patience went far beyond the call of duty.

I would like to say thanks to Karl Boylan for sourcing the strongly gain coupled DFB laser diode used in this research.

At this point, I would like to thank the members of the group both past and present. especially Canice, Alan, Cian, Andrea and John P who provided support in the early feet-finding days of the lab. To the present group members a special thanks goes to Torsten, Mathias, Laura, Severine, Aoran, for all the help. A special thanks to Dave and Seve better known as 'the Dude', the frustrations of life underground never seemed quite as bad after talking to these two guys.

Thanks also to the technical staff of the Physics Department, Dave Grouse, Mick O'Reilly, Ken Concannon and John Kelly.

To all my teammates from the St Judes hurling team for all the highs and lows of championship hurling throughout the last four years.

To my friends for putting up with me when work wasn't going so well, thanks to Dermot, Larry, Ken and the rest of the gang, and especially Helen.

Finally I wish to thank my parents and family, to whom this thesis is dedicated, for their support and financial assistance throughout my academic career.

## *Publications*

R. Phelan, V. Weldon, M. Lynch, and J. F. Donegan, "Simultaneous multigas detection with cascaded strongly gain coupled DFB laser by dual wavelength operation," *Electronics Letters*, vol. 38, pp. 31-32, 2002.

R. Phelan, M. Lynch, J. F. Donegan, and V. Weldon, "Investigation of a strongly gain coupled DFB laser cascade for simultaneous multigas sensing," *Optoelectronics, IEE Proceedings-*, vol. 150, pp. 182-186, 2003.

R. Phelan, M. Lynch, J. F. Donegan, and V. Weldon, "Absorption line shift with temperature and pressure: impact on laser-diode-based H<sub>2</sub>O sensing at 1.393  $\mu\text{m}$ ," *Applied Optics*, vol. 42, pp. 4968-4974, 2003.

R. Phelan, M. Lynch, J. F. Donegan, and V. Weldon, "Investigation of widely tuneable laser diodes for spectroscopic based multigas sensing at 1.5  $\mu\text{m}$ ," presented at Lasers and Electro-Optics Europe, 2003. CLEO/Europe. 2003.

R. Phelan, M. Lynch, J. F. Donegan, and V. Weldon, "Simultaneous multi-species gas sensing using a sampled grating-DBR and modulated-grating Y laser diode" submitted to *Applied Optics December 2004*.



# Table of Contents

<b>1 Introduction</b>	1
1.1 Background	1
1.2 Thesis Overview	4
1.3 References.	6
<b>2 Principles of Absorption Spectroscopy</b>	7
2.1 Introduction	7
2.2 Beer-Lambert law	7
2.3 Linestrength	8
2.3.1 Measuring Linestrength.	9
2.4 Spectral Lineshapes	9
2.4.1 Doppler broadening	10
2.4.2 Pressure broadening and shift	12
2.4.3 Voigt Profile	14
2.5 Dicke Narrowing	15
2.6 Sensitivity of Direct detection	17
2.7 Modulation Spectroscopy	19
2.7.1 Introduction	19
2.7.2 WMS	20
2.7.3 FMS	26
2.8 References.	30
<b>3 Widely Tuneable Semiconductor Lasers</b>	35
3.1 Introduction	35
3.2 Basic Concept of tuneable laser	36
3.3 Wave propagation in periodic structures	37
3.3.1 Distributed Bragg reflectors	38
3.3.2 Distributed feedback lasers	40
3.4 Carrier-induced index change	43
3.4.1 Band-filling	43
3.4.2 Band-gap shrinkage	43
3.4.3 Free-carrier absorption	43
3.4.4 Temperature tuning	43
3.5 Extending the tuning range of DBR-type lasers	44
3.5.1 Vernier effect between two comb reflectors	44
3.5.2 Sampled Grating DBR	46
3.5.3 Modulated Grating Y-Laser	49
3.6 Characteristics of tuneable lasers for gas sensing.	51
3.6.1 Tuning Range	51
3.6.2 Spectrum and Side Mode suppression ratio	53
3.6.3 High FM/AM ratio	55
3.6.4 Spectral Linewidth	56
3.7 Conclusions	63
3.8 References.	65

<b>4 Absorption Line Shift with Temperature and Pressure Impact on Laser Diode based H<sub>2</sub>O Sensing at 1.393 μm</b>	71
4.1 Introduction	71
4.2 Experimental	72
4.2.1 Gas cell	72
4.2.2 Laser diode	73
4.3 Near-Infrared Spectra of H <sub>2</sub> O	76
4.4 Direct-Detection Measurements	77
4.5 Direct-Detection Results	78
4.6 WMS 2f measurements	85
4.7 WMS 2f Results	86
4.8 Conclusions	89
4.9 References.	90
<b>5 Simultaneous Multi-Gas Sensing using a Strongly Gain Coupled DFB laser diode</b>	93
5.1 Introduction	94
5.2 SGC-DFB Device	95
5.3 Near-Infrared Spectra of Target gases	97
5.3.1 Hydrogen Sulphide	97
5.3.2 Carbon dioxide	97
5.4 Experimental Details	99
5.5 Simultaneous detection of H <sub>2</sub> S and CO <sub>2</sub>	100
5.6 Feed-back control and stabilisation	104
5.7 Conclusion	108
5.8 References.	109
<b>6 Multi-Species Gas Sensing using a SG-DBR and MG-Y laser Sensing and Absorption Line Identification</b>	112
6.1 Introduction	112
6.2 Advanced static characterisation	113
6.2.1 Characterisation methods to generate a frequency look-up tables	120
6.3 Application to gas sensing	125
6.3.1 Experimental	126
6.3.2 Results	127
6.3.2.1 Grating Modulation	127
6.3.2.2 Multiple-species gas sensing	129
6.4 Line Identification	134
6.4.1 Introduction	134
6.4.2 Identification of Gas Lines	135
6.5 Conclusions	142
6.6 References.	143
<b>7 Conclusions</b>	146
7.1 Overview	146
7.2 Future work	148
7.3 References.	150



# Chapter 1

## Introduction

### 1.1 Background

Significant demand exists for gas-sensing techniques that are fast, selective and compact, and laser-based approaches are attractive because they offer the promise of meeting these criteria. For these systems, near infrared diode lasers are popular as sources because they have the beneficial feature of narrow linewidth, compact size, cost-effectiveness and compatibility with optical fibres, which enables convenient alignment and multiplexing. Historically, the first measurements with diode-lasers have been made with mid-infrared lead-salt devices [1, 2]. Lead-salt lasers cover the 3 to 30  $\mu\text{m}$  spectral region, which overlaps with the fundamental absorption bands of a number of important molecular species. For industrial applications the use of lead-salt diode-lasers is limited due to the need for cryogenic cooling, occurrence of multimode emission and low power levels [2]. Several molecular species have absorption features in the near infrared spectral region. Telecommunication lasers operate at near infrared wavelengths (generally 1.5 $\mu\text{m}$ ), and therefore overlap with the spectra of vibrational overtones, which are 10-200 times weaker than the spectra resulting from fundamental vibrations. To compensate for these small absorption strengths, high sensitivity detection techniques such as Frequency Modulation Spectroscopy (FMS) and Wavelength Modulation Spectroscopy (WMS) are employed [3].

Sensors based on these lasers have found applications in, toxic emission monitoring, monitoring of the levels of explosive hydrocarbon gases, monitoring of background vapour concentrations in semiconductor device fabrication lines, and continuous emission monitoring in smokestacks. These tuneable laser diode absorption spectrometers (TDLAS) can identify the gases with high precision because the optical absorption spectrum of most gases consists of many sharp individual lines. The laser



diode can lock on the unique fine structure of the target gas absorption spectrum and use it as a fingerprint to measure the gas absorption spectrum with high specificity and high sensitivity [4].

Recently, industrial and private capital investment in the commercialisation of diode laser sensors has surged, providing an end-use for the development of sensors in research laboratories. The uptake of TDLAS is currently buoyant due to the increased availability of single frequency laser diodes at lower cost, which is a result of the growth in optical fibre communications. Today diode lasers dominate the overall laser market, representing over \$1.6 billion in 2003 sales [5], as illustrated in Fig 1.1. The majority of these sales are in the optical storage and telecommunication industries, comprising devices operating between 400-700 nm and 950-1600 nm respectively. The requirements of the telecommunication industry for devices operating near room temperature, with a wavelength tuning, high spectral purity, long-term stability, and compatibility with fibre-optic networks are all consistent with practical spectroscopic absorption sensors.

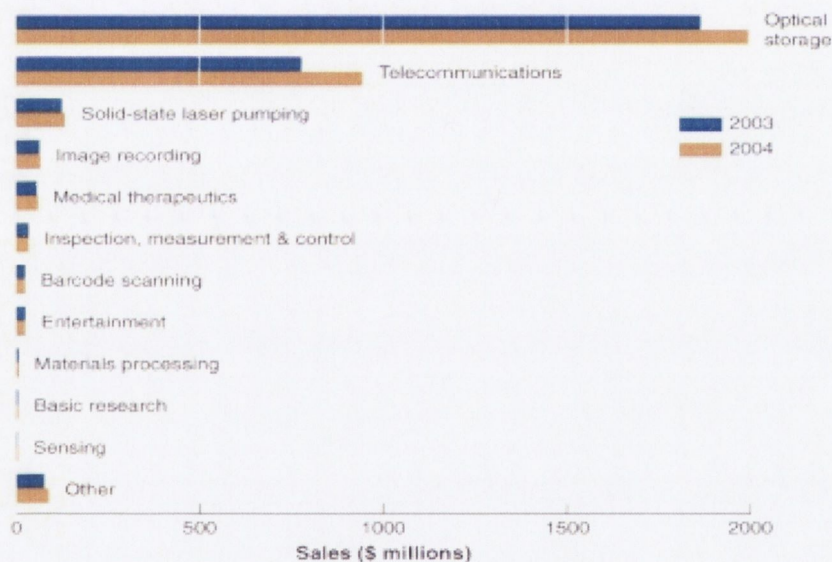


**Figure 1.1** Worldwide diode-laser sales by application [5].

Because of the large market potential for dense wavelength division multiplexing in telecommunication, the availability and quality of these devices near 1.55 $\mu\text{m}$  can be expected to improve considerably. Also technology for fibre manufacturing has been significantly improved recently. The water concentration in some fibre, e.g. Lucent Technologies All-Wave optical fibre, can be made so low that the entire range 1285



nm to 1625 nm can now be used for laser transmission with reasonably low attenuation. Therefore, telecom lasers are likely to be available over this larger wavelength range in the near future to take full advantage of these new fibres. Many important gas species have transitions in this wavelength range, and thus this extension of telecom wavelength range can be valuable to the gas sensing community. The current state-of-the-art in the application of TDLAS is single species limited, due to the narrow tune ability of distributed feedback laser diodes, which limits detection to a single gas. This has prevented the widespread uptake of TDLAS technology in multi-gas detection applications despite the strong demand and the demonstrated TDLAS capability in respect of single gas detection. Fortunately, the insatiable demand for bandwidth in optical communications has driven the development of widely tuneable laser diodes for incorporation in optical networks as back-up systems. This is a major growth area in optical communications technology. These single frequency laser diodes, because they are widely tuneable, present opportunities for applications in absorption based multi-gas sensing regime. Sampled grating distributed Bragg reflector, Modulated Grating Y-branch and Strongly Gain Coupled cascaded distributed feedback laser diodes, with typical tuning ranges of 50nm, 50nm and 15nm respectively, are examples of monolithic integrated widely tuneable devices developed for optical communications. Lasers in which the wavelength selection and tuning functions are external to the semiconductor structure are not discussed here since they are considered not compatible with the requirements for industrial deployment. Future development of quantum cascade lasers will bring the benefits of room temperature operation to the longer wavelengths that are most useful for sensitive gas detection

Research on monolithically integrated tuneable laser diodes has a fairly long history (more than 20 years) [6]. However until recently tuneable laser diodes were deemed unsuitable for applications in multi-species gas sensing due to their complex control and the stringent requirements posed on devices for gas sensing applications.

The aim of this project is to advance the strategic capability required to allow development of TDLAS multi-species gas detection systems using widely tuneable laser diodes. Such detection systems will enable the real time simultaneous monitoring of multi-gas species, by taking advantage of the new widely tuneable laser diodes which have emerged in the past few years. A considerable advantage over the existing arrangement where monitoring is limited to a single gas



## 1.2 Thesis Overview

*Chapter 2* provides a general introduction to absorption spectroscopy in the near infrared region. Spectral line intensity and lineshape theories are briefly outlined.

*Chapter 3* provides a general introduction to single frequency laser diodes and monolithically integrated widely tuneable laser diodes that are available for applications in multi-species gas sensing. The relevant physical mechanisms enabling electronic control of the emission frequency of these widely tuneable lasers is next outlined followed by the main requirements for applications in multi-species gas sensing.

*Chapter 4.* High-resolution absorption measurements of the H<sub>2</sub>O line in the  $\nu_1+\nu_3$  band at 1.3928 $\mu\text{m}$  were made in the temperature range 296K - 1100K using an InGaAsP distributed feedback laser diode operating at 1.39 $\mu\text{m}$ . Spectral line shift as a function of temperature and pressure and line strength measurements on the water vapour line and their impact on the accuracy of optical absorption based gas sensing has been investigated. The results obtained were compared with values obtained from the HITRAN database and values reported in the literature for H<sub>2</sub>O. The results, facilitates H<sub>2</sub>O sensing in a non-standard temperature and pressure environment.

*Chapter 5.* The use of a strongly gain coupled (SGC) three-section DFB laser cascade operating in the 1575-1585 nm region to multi-gas detection is reported for the first time. Simultaneous detection of Hydrogen Sulphide and Carbon Dioxide by dual wavelength operation of SGC three-section DFB laser cascade is detailed. The device consisted of three cascaded sections ( $S_1$ ,  $S_2$  and  $S_3$ ) and an optical amplifier. Dual wavelength operation was achieved by biasing  $S_1$  and  $S_2$  above threshold. By precise dual independent wavelength tuning of the laser diode, both gases were simultaneously detected using wavelength modulation spectroscopy. The use of a SGC DFB laser in a dual wavelength mode has the potential to eliminate the need for multiple laser devices to simultaneously monitor more than one gas. However, when operating the SGC in a dual wavelength emission mode, thermal cross talk between the lasing sections complicates somewhat the setting of the emission wavelength of  $S_1$



and  $S_2$ . We have investigated stabilization techniques to minimise the effect of this cross talk.

*Chapter 6* outlines the application of a sampled grating distributed Bragg reflector and a modulated grating Y-branch laser as a widely tuneable source in a multi-species gas detection system. The use of widely tuneable laser diodes as sources in a multi-gas analysing system using wavelength modulation spectroscopy and second harmonic detection of acetylene hydrogen cyanide and ammonia have been investigated. The critical issues relevant to the application of such widely tuneable diode lasers to spectroscopic based high selectivity multi-gas sensing are outlined. The general emphasis of the work described in this chapter is not on detection limits but to selectively detect three gases with overlapping absorption bands.

A simple and straightforward method using multiple reference gases for wavelength characterisation and monitoring of a SGDBR is next outlined. This method requires measurements of the gas absorption lines, an etalon trace and comparing the separations between gas absorption lines and the corresponding separations from a database (HITRAN) to determine the emission wavelength of the SGDBR.

Chapter 7 Presents our conclusions and suggestions for future work.

### 1.3 References

- [1] R.T. Ku, E.D Hinkley, and J.O. Sample, "Long-path monitoring of atmospheric carbon monoxide with a tunable diode laser system," *Applied Optics*, vol. 14, pp. 854, 1975.
- [2] P. Hering, *Laser in Environmental and Life Sciences*: Springer, 2004.
- [3] J. A. Silver, "Frequency-Modulation Spectroscopy for Trace Species Detection - Theory and Comparison among Experimental Methods," *Applied Optics*, vol. 31, pp. 707-717, 1992.
- [4] V. Weldon, "Spectroscopic Based Gas Sensing using Single Frequency Near Visible/Infrared Laser Diodes," Ph.D thesis: Trinity College Dublin, 1997
- [5] R. Steele, "Review and forecast of the laser markets: Part II: Diode lasers," in *Laser focus world*. February, 2004.
- [6] L. A. Coldren, "Monolithic tunable diode lasers," *Selected Topics in Quantum Electronics, IEEE Journal of*, vol. 6, pp. 988-999, 2000.



# Chapter 2

## Principles of Absorption Spectroscopy

### 2.1 Introduction

This chapter provides an introduction to tuneable diode laser absorption spectroscopy in the near-infrared region. This is important since, in the work described here, narrow linewidth, single frequency, wavelength tuneable laser diodes are used to target individual rotational absorption lines. The fundamentals of absorption spectroscopy and the dominant broadening mechanisms which determine the spectral width of absorption lines are introduced. In addition, to spectral line broadening due to collisions, collisions can also result in a narrowing of spectral profiles. In this work two techniques for diode-laser absorption spectroscopy were used: direct absorption spectroscopy and wavelength modulation spectroscopy. Their essential characteristics and limitations will be discussed in the following sections.

### 2.2 Beer-Lambert law

When monochromatic radiation of frequency  $\nu$  ( $\text{cm}^{-1}$ ) passes through an absorbing gas of path length  $L$  (cm), the transmission coefficient  $\tau(\nu)$ , according to the Beer-Lambert law, is defined as

$$\tau(\nu) = \left( \frac{I_T}{I_0} \right) = \exp[-\kappa(\nu)] \quad (2.1)$$

where  $I_0$  and  $I_T$  are the incident and transmitted intensities, respectively. The spectral dependence of the absorption coefficient  $\kappa(\nu)$  can be expressed as

$$\kappa(\nu) = Sn\phi(\nu)L \quad (2.2)$$

where  $S$  (cm/molecule) is the spectral line intensity, and  $n$  [molecule/cm<sup>3</sup>] is the number density of the absorbing species. Lineshape function  $\phi(\nu)$  (cm) represents the probability of finding absorbing events between frequencies  $\nu$  and  $\nu + d\nu$  and satisfies the normalization condition

$$\int_{-\infty}^{+\infty} \phi(\nu)d\nu \equiv 1 \quad (2.3)$$

## 2.3 Linestrength

Specifying the maximum value of the absorption coefficient is not a satisfactory measure of the total absorption intensity since no inclusion of the width of the spectral feature is made. The intensity of a spectral feature must therefore be specified by the area under the absorption curve over the wavelength region of interest. The strength  $S$ , is defined as

$$S = \int_{-\infty}^{+\infty} \kappa(\nu)d\nu \quad (2.4)$$

The line strength or line intensity is a direct measure of the ability of a molecule to absorb photons corresponding to a given transition. The intensities of spectral lines depend not only on the population density of the molecules in the absorbing or emitting level which is a function of the Boltzmann fraction, but also on the transition probabilities of the corresponding molecular transitions.

The typical units for linestrength include a pressure-dependent version,  $S$  (cm<sup>-1</sup>atm<sup>-2</sup>), and a number-density dependent version used by Hitran,  $S^*$  (cm mol<sup>-1</sup>) [1, 2]. For gases obeying the ideal gas law ( $PV=nkT$ ), the conversion between  $S$  and  $S^*$  is given by,

$$S(T) = n_L \frac{T_0}{T} S^*(T) \square \frac{7.34 \times 10^{21}}{T} S^*(T) \quad (2.5)$$

where  $n_L$  is the Loschmidt's number, and  $T_0$  is the absolute temperature [3]. For converting room-temperature linestrength ( $T=296K$ ), the conversion is

$$S = S^* \times (2.488 \times 10^{19}) \quad (2.6)$$



It must be remembered that since the transition probabilities corresponding to overtone bands is much less than corresponding fundamental transitions, absorption band strengths at these overtone/combination wavelengths are significantly weaker than at fundamental wavelengths.

### 2.3.1 Measuring Linestrength.

The linestrength of an absorption transition is a key parameter for designing absorption based gas sensors. Though published linestrengths are available for many molecules in the 1.5 $\mu\text{m}$  region [2, 4], there are still a considerable number of molecules where no linestrength information is available or are often based on calculations or low-resolution measurements. Thus, high-resolution tuneable laser diodes can be used to improve linestrength estimates.

The line strength  $S$  ( $\text{cm}^{-1}\text{atm}^{-2}$ ), for a particular transition can be determined from the integrated area  $A$  of the transition [5], divided by the partial pressure of the absorbing species  $P_J$  and the path length  $L$ .

$$S = \frac{A}{P_J L} \quad (2.7)$$

The integrated area is measured by scanning the emission wavelength of the laser and measuring the transmitted light attenuation as a function of wavelength. Thus the lineshape profile of the absorption feature can be recorded and fitted to extract the area.

## 2.4 Spectral Lineshapes

A typical lineshape of an isolated absorption line centred at  $\nu_0$  at low pressure, as a function of frequency is shown in Fig. 2.1. The width of the feature,  $\Delta\nu$ , is defined by the full width at half the maximum value (FWHM). Broadening of an absorption feature occurs due to phenomena in the medium that perturb the transition's energy levels or the way in which individual atoms and molecules interact with light. The dominant broadening mechanisms are collisional or pressure broadening (homogeneous) and Doppler broadening (inhomogeneous), which are described below.

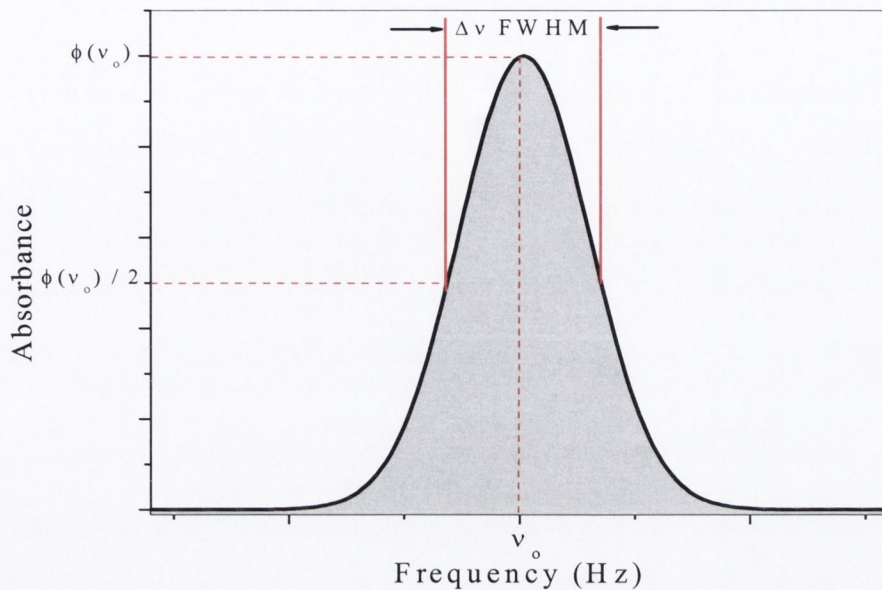


**Figure. 2.1** Sample lineshape as a function of frequency

### 2.4.1 Doppler broadening

When a molecule has a velocity component in the same direction as the propagation of a beam of light, there will be a shift in the frequency at which it will absorb a photon. This effect is called the Doppler shift [6]. The molecules of any gas are in constant thermal motion and the distribution of their random velocities is described by the Maxwell velocity distribution function. We can consider each group of molecules with the same velocity component to be part of a velocity class. The Maxwellian velocity distribution function tells us what portion of the molecules are in each class. Each velocity class will have its own Doppler shift. Thus the distribution function leads directly to a lineshape function with a Gaussian form:

$$\phi_D(\nu) = \frac{2}{\Delta\nu_D} \left( \frac{\ln(2)}{\pi} \right)^{1/2} \exp \left( -4 \ln 2 \left( \frac{\nu - \nu_0}{\Delta\nu_D} \right)^2 \right) \quad (2.8)$$



Where  $\nu_0$  is the line-centre frequency and  $\Delta\nu_D$  is the Doppler full width half maximum (FWHM) linewidth.

The magnitude of the Gaussian lineshape function at line centre is

$$\phi_D(\nu_0) = \frac{2}{\Delta\nu_D} \left( \frac{\ln 2}{\pi} \right)^{1/2} \quad (2.9)$$

The Doppler fullwidth (FWHM)  $\Delta\nu_D$  is given by

$$\Delta\nu_D = \nu_0 \left( \frac{8kT \ln 2}{mc^2} \right)^{1/2} \quad (2.10)$$

for which a more convenient form is

$$\Delta\nu_D = \nu_0 (7.1623 \times 10^{-7}) \left( \frac{T}{M} \right)^{1/2} \quad (2.11)$$

where T is in Kelvin and M is the molecular weight in grams/mole [7]. Fig. 2.2 illustrates the increasing Doppler width with temperature for H<sub>2</sub>O at 940nm, H<sub>2</sub>O at 1.39 $\mu$ m and CO<sub>2</sub> at 1.39 $\mu$ m. As can be seen from Fig. 2.2, thermal broadening affects H<sub>2</sub>O much more than CO<sub>2</sub> due to the formers comparatively small mass. It affects shorter wavelengths more than longer wavelengths for the same molecule due to the frequency-dependence of the broadening mechanism.

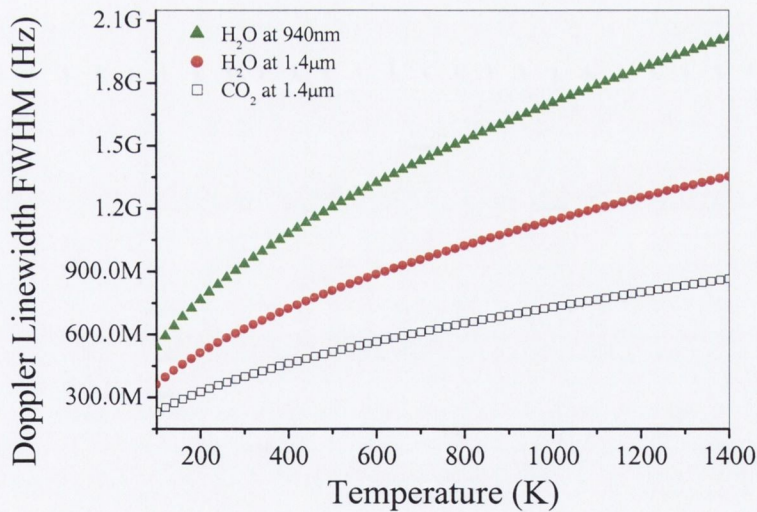


**Figure 2.2** Comparison of Doppler widths for H<sub>2</sub>O and CO<sub>2</sub> for a range of temperatures calculated using equation 2.11.

## 2.4.2 Pressure broadening and shift

It is well known that the dominant absorption line broadening mechanism at pressures above a few tens of mbars is collision broadening. Since most optical absorption based gas sensing is carried out at atmospheric pressure the effect of collision line broadening is very important. Molecules in a gas are in continual motion and collide with each other at a rate  $1/\tau_c$ , which increases with gas pressure where  $\tau_c$  is the mean time between collisions. Vibrational and rotational energies of the molecules are perturbed by these collisions, which interrupt the dipole oscillation resulting in a broadening of the vibrational/rotational lineshape. The largest source of line shift is associated with energy level shift caused by the interaction of the molecules during elastic collisions as shown in Fig 2.3 [8]. The collisional shift can be explained with the aid of potential curves. In a gas mixture of atoms A and B the mutual separation  $R(A,B)$  show random fluctuations with a distribution around a mean value  $R$  which depends on temperature and pressure. Accordingly  $\omega_{ik} = |E_i(R) - E_k(R)|/\hbar$  yields a corresponding frequency distribution around a most probable value  $\omega_{ik}(R_m)$ , which may be shifted against the frequency  $\omega_0$  of the unperturbed atom A. The shift  $\Delta\omega = \omega_0 - \omega_{ik}$  depends on how differently the two energy levels  $E_i$  and  $E_k$  are shifted at a distance  $R_m(A,B)$  where the emission probability has a maximum. The elastic collisions change not the amplitude, but the phase of the damped oscillator, due to the frequency shift  $\Delta\omega(R)$  during the collision. They are often termed phase-perturbing collisions. A pressure-broadened line has a Lorentzian profile expressed as

$$\phi_C(\nu) = \frac{1}{2\pi} \frac{\Delta\nu_C}{(\nu - \nu_0 - \Delta_S)^2 + (\Delta\nu_C/2)^2} \quad (2.12)$$

where  $\Delta\nu_C$  is the collision FWHM and  $\Delta_S$  is the pressure-induced shift [6]. Because the collision interactions are proportional to the density of the perturbing species,  $\Delta\nu_C$  and  $\Delta_S$  are related to the pressure broadening coefficient,  $\gamma$  (Hz/atm), and shift coefficient by  $\delta$  (Hz/atm), by

$$\Delta\nu_C = \gamma.P \quad (2.13)$$

$$\Delta_S = \delta.P \quad (2.14)$$



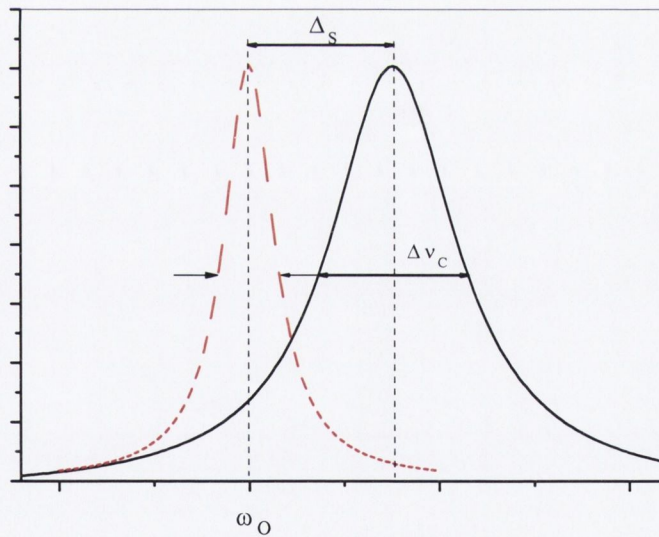
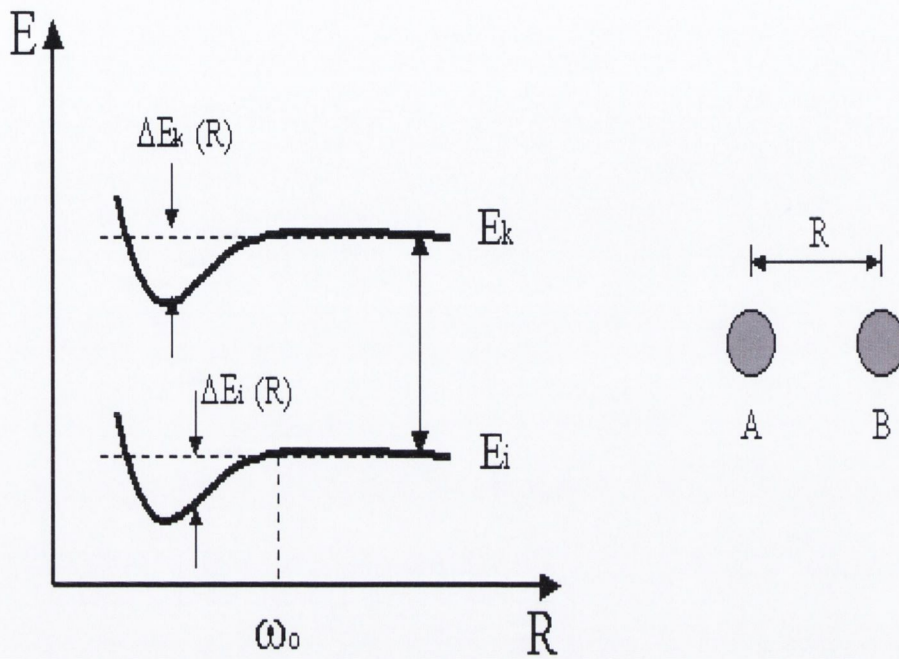


**Figure 2.3.** (a) Illustration of collisional line broadening and shift explained with the potential curves of the collision pair A, B. The energy shifts  $\Delta$  may be positive as well as negative.  $\Delta E$  is positive if the interaction between A and B is repulsive and negative if it is attractive [8]. (b) Shift and broadening of a Lorentzian line profile by collision.

where P is the perturber pressure in atmosphere. The temperature dependence of  $\gamma$  and  $\delta$  are often modelled as

$$\gamma(T) \propto T^{-n} \quad (2.15)$$

$$\delta(T) \propto T^{-m} \quad (2.16)$$

where n and m are called temperature exponents [7]. Values of n and m depend on the absorber and perturber species and the rotational-vibrational quantum numbers.

### 2.4.3 Voigt Profile

In the gas pressure range between the above two cases where neither collision nor Doppler broadening dominate, the absorption lineshape can be described by a Voigt profile. The Voigt profile  $\phi_V$  is the convolution of the Doppler  $\phi_D$  and the Lorentzian  $\phi_L$  profile as indicated in the following equation,

$$\phi_V(\nu) = \int_{-\infty}^{+\infty} \phi_D(u) \phi_L(\nu - u) du \quad (2.17)$$

For this reason, it assumes Doppler characteristics at low pressure and Lorentzian characteristics at higher pressures. Therefore, one single expression for the lineshape can be used throughout a wide range of pressures. The Voigt y parameter indicates the relative significance of Doppler and collisional broadening, with y increasing as the effects of collisional broadening increase.

$$y = \sqrt{\ln 2} \frac{\gamma_C}{\gamma_D} \quad (2.18)$$

The x parameter is a dimensionless measure of the distance from line centre and is defined as follows

$$x = \frac{2\sqrt{\ln 2}(\nu - \nu_0)}{\Delta\nu_D} \quad (2.19)$$

defining an integral variable t as

$$t = \frac{2u\sqrt{\ln 2}}{\Delta\nu_D} \quad (2.20)$$

The Voigt profile is defined as



$$V(x, y) \equiv \frac{y}{\pi} \int_{-\infty}^{\infty} \frac{\exp(-t^2)}{y^2 + (x-t)^2} dt = \text{Re}[w(x, y)], \quad (2.21)$$

The Voigt function is conveniently expressed as the real part of the complex probability function  $w(x, y)$ . The real and imaginary parts of the complex probability function  $w(x, y)$  were calculated using a routine by Humlicek [9]. Fig 2.4 compares the standardised Gaussian, Lorentzian, and Voigt profiles. Note the Gaussian profile decays rapidly (exponential) from the line centre while the Lorentzian profile decays slowly (quadratic).

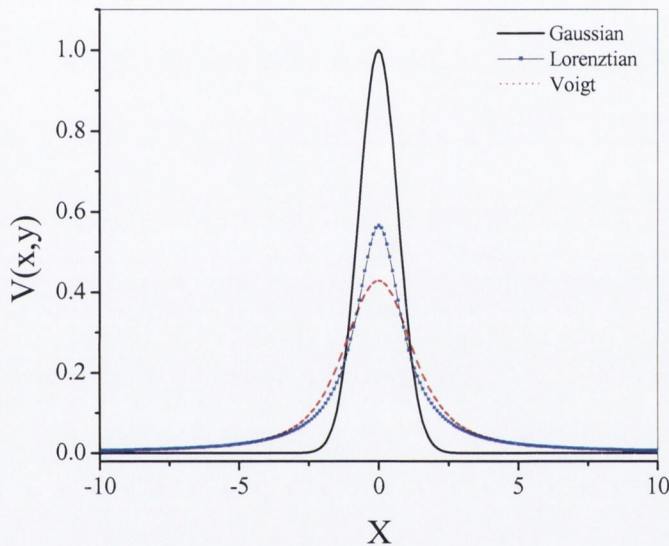


**Figure 2.4** Calculated lineshapes for Gaussian, Lorentzian and Voigt profiles ( $y=1$ ).

## 2.5 Dicke narrowing

In addition to spectral line broadening due to phase-changing collisions, collisions can also narrow spectral profiles [10]. Dicke first predicted the narrowing of the Doppler profile when he considered a radiating atom bouncing back and forth within a one-dimensional box. The mean free path ( $\Lambda$ ) in this approach is equal to the box dimension since the atom can only collide with the walls. When the dimension of the box is much larger than the wavelength of radiation ( $\Lambda \gg \lambda$ ) a detector on the wall observes distinct red and blue shifts from the centre frequency (Doppler principle). However, when  $\Lambda \sim \lambda$ ,

the radiating frequencies are shifted and modulated by the frequent collisions. If this effect is averaged over a Maxwellian velocity distribution, the result is a normal Doppler line with a sharp non-Doppler centre peak. The Dicke narrowing effect is also referred to as the collisional, motional, or confinement narrowing effect.

In the presence of the Dicke narrowing effect, a lineshape may vary appreciably from the Voigt profile. In this case the Galatry soft-collision profile [11] and the Rautian-Sobelman hard-collision profile [11] are appropriate to facilitate the inclusion of collisional-narrowing effects and it is possible to extract line parameters with high accuracy.

The model of Rautian considers that the mass of the active molecule is much smaller than the mass of the perturber. This is the reason why this model is called the hard collision model. This profile can be expressed as:

$$R(x, y, z) \equiv \text{Re} \left[ \frac{w(x, y + z)}{1 - \sqrt{\pi} z w(x, y + z)} \right] \quad (2.22)$$

where  $x$  and  $y$  have the same definition as in equation 2.21, and where  $z$  is the narrowing parameter. This additional parameter is describing the Dicke effect and is given by

$$z = 2\sqrt{\ln 2} \frac{\beta_C}{\Delta_D} \quad (2.23)$$

where  $\beta_C$  is the coefficient of collisional narrowing [12]. Galatry has developed a model considering that the mass of the active molecule is much larger than the mass of the perturber. This profile can be expressed as:

$$G(x, y, z) = \frac{1}{\sqrt{\pi}} \text{Re} \left\{ \exp \left[ (-ix - y)t + \frac{1}{2z^2} (1 - zt - e^{-zt}) \right] dt \right\} \quad (2.24)$$

where  $x$ ,  $y$  and  $z$  have the same definitions as above.

The real and imaginary parts of the complex probability function  $w(x, y)$  are calculated using a routine by Humlicek [9, 13] and the calculation of the Galatry profile according to Varghese and Hanson [14, 15] in subsequent parts of this thesis.



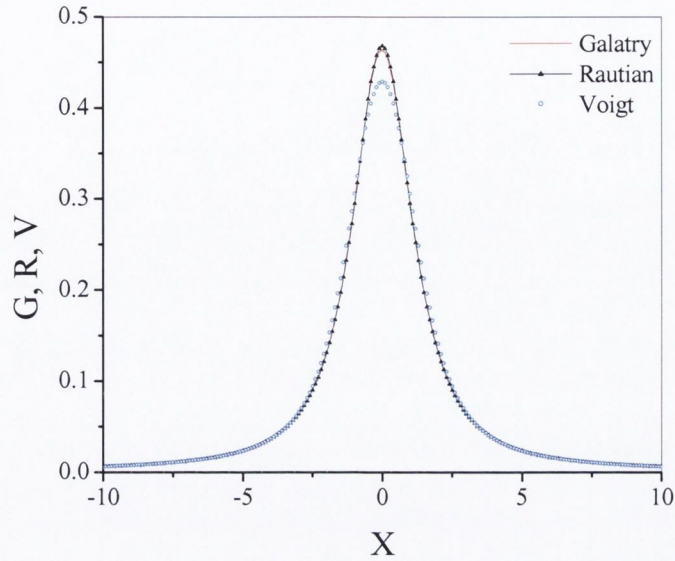


**Figure 2.5** Calculated lineshapes for Voigt, Galatry and Rautian profiles (for  $y = z = 1$ ). Theoretical Voigt, Rautian and Galatry profiles are compared and shown. Due to the Dicke narrowing effect, the Rautian and Galatry profiles are narrower and sharper than the Voigt profile. Both the Galatry and Rautian profiles collapse into the Voigt profile when  $z=0$ .

## 2.6 Sensitivity of Direct detection

Typically, in a laser based gas sensing study the output of the laser is directed through the target gas and the transmitted light is measured as a function of wavelength by a photo detector. A typical detector consists of a photodiode, which converts photons into hole-electron pairs, and a load resistor, which converts current signals to voltage signals. The intrinsic noises in the output voltage consist of shot noise and thermal noise. Shot noise originates from intrinsic random photon generation and annihilation processes in the laser cavity [16]. If shot noise is the dominant noise source, an achievable minimum detectable absorbance where  $\alpha_{\min}$  is

$$\alpha_{\min} = \frac{\sqrt{2ei_{ph}B}}{i_{ph}} = \sqrt{\frac{2eB}{\eta P_0}} \quad (2.25)$$

where  $e$  is the charge on the electron,  $B$  [Hz] is the detection bandwidth,  $\eta$  [A/W] is the photodiode responsivity,  $P_0$  [W] is the incident power, and  $I_{ph}$  [A] ( $= \eta P_0$ ) is the photocurrent [17]. For a 1-Hz bandwidth,  $\alpha_{min}$  is  $\sim 2 \times 10^8$  (using  $P_0 = 1\text{mW}$  for a typical diode laser and  $\eta = 1$  A/W for a typical InGaAs photodiode). Inherent thermal noise in a pn junction diode and a load resistor  $R$  is usually characterized by a Johnson-Nyquist formula [17]. Detection sensitivity in the thermal-noise limit is

$$\alpha_{min} = \frac{\sqrt{4kTRB}}{i_{ph}} = \frac{1}{\eta P_0} \sqrt{\frac{4kTB}{R}} \quad (2.26)$$

where  $T$  is the equilibrium temperature of the junction. For  $P_0 = 1$  mW,  $\eta = 1$  A/W,  $T = 300$  K, and  $R = 1$  k $\Omega$ ,  $\alpha_{min}$  is  $\sim 4 \times 10^9$  for a 1-Hz bandwidth. Fig 2.6 shows the calculated  $\alpha_{min}$  at various incident laser power. Note that  $\alpha_{min}$  decreases with increasing incident laser power. At low power,  $\alpha_{min}$  is thermal-noise limited and decreases with  $1/P_0$ . When  $P_0 \geq 1\text{mW}$ , shot noise becomes the dominant noise source and  $\alpha_{min}$  scales with  $1/\sqrt{P_0}$ . For typical diode lasers with mW output power, theoretical  $\alpha_{min}$  is limited by the shot noise. In practice, achievable  $\alpha_{min}$  is orders of magnitude larger than the shot-noise limited sensitivity, mainly due to a considerable  $1/f$  intensity noise in the diode laser output, which dominates at low frequencies in the range of 0.1-10 MHz. Models have been proposed to explain the  $1/f$  intensity noise in diode lasers, but the physical origin is not yet clear [18].



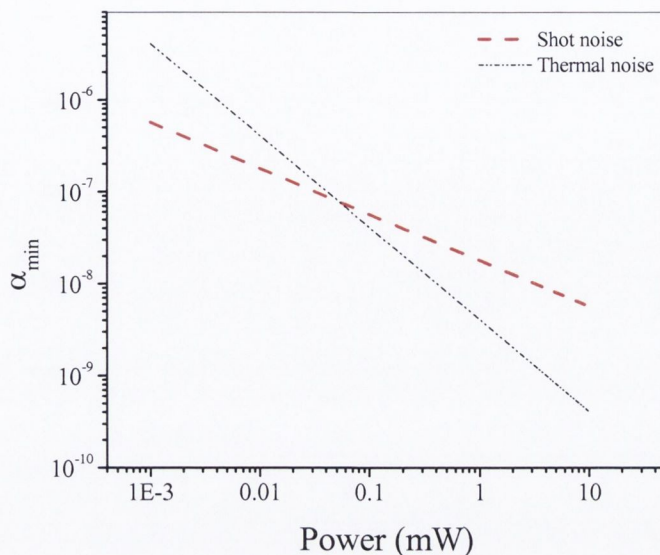


**Figure 2.6** Calculated minimum detectable absorbance,  $\alpha_{min}$ , with 1Hz bandwidth as a function of laser incident power. ( $\eta = 1 A/W$ ,  $T=300K$ , and  $R=1 k\Omega$ )

## 2.7 Modulation Spectroscopy

### 2.7.1 Introduction

The vibrational overtone/combination absorption line-strengths of gases in the near-infrared region of the spectrum are significantly less than the fundamental line-strengths in the mid-infrared. Hence, to measure these weak absorption signals high sensitivity techniques known as Wavelength Modulation Spectroscopy (WMS) or Frequency Modulation Spectroscopy are required (FMS) [19-24]. The key difference between these two methods is that for FMS the modulation frequency is equal to or greater than the absorption linewidth whereas for WMS the modulation frequency is much less than the gas linewidth. In brief the basic principle of WMS, is to probe a gas absorption line while modulating the emission wavelength of the laser diode. The detected output is processed by a lock-in-amplifier at the modulation frequency,  $f$  or  $n$  times the modulation frequency where  $n$  is an integer [25]. Its advantage over direct detection is twofold in that it shifts the detection to higher frequencies where the  $1/f$  laser excess noise is reduced. It also removes much of the base line slope seen in direct detection. Diode-laser WMS and

FMS can be treated with a uniform approach using the electric field of laser radiation [19, 20]. However, since only WMS was used in this thesis, the traditional mathematical approach using the intensity of laser radiation is used here [21]. A brief outline of FMS is also included.

### 2.7.2 WMS

The emission wavelength of a diode laser can be conveniently modulated by modulating the injection current at frequencies from sub Hz to their relaxation resonance frequency, that is typically in the range 1-10GHz. Although the name of the technique suggests that it is the wavelength that is modulated, it has been found more convenient to treat the modulation process in frequency units [21]. The instantaneous diode laser light frequency,  $\nu(t)$ , can therefore be written:

$$\nu(t) = \bar{\nu} + a \cos \omega t \quad (2.27)$$

where  $\bar{\nu}$  is the laser mean emission frequency and  $a$  is the modulation amplitude. We can assume the mean frequency and the laser intensity are independent of each other. If we now substitute the time-dependent term  $I(\nu(t))$  into the equation 2.1,

$$I(\nu) = I_o(\nu) \left[ 1 - k(\bar{\nu} + a \cos \omega t)nL \right] \quad (2.28)$$

This time varying function (2.28) is a periodic and even function in  $\omega t$  and can be expanded by Fourier cosine series as

$$k(\bar{\nu} + a \cos \omega t) = \sum_{n=0}^{\infty} H_n(\bar{\nu}) \cos n\omega t \quad (2.29)$$

where  $\bar{\nu}$  is considered to be constant over a modulation period.  $H_n(\bar{\nu})$  is the  $n^{\text{th}}$  Fourier component of the modulated absorption coefficient. Individual Fourier components can be selected using a lock-in amplifier at the  $n^{\text{th}}$  harmonic of the modulation frequency. This term is ultimately dependent on the absorption lineshape. If the pressure is such that collision broadening is dominant, then the absorption coefficient is described by a Lorentzian function



$$k_L(\nu) = \frac{1}{1 + \left[ \frac{\nu(t) - \nu_0}{\gamma_L} \right]^2} \quad (2.30)$$

where  $\gamma_L$  is the Half Width at Half Maximum (HWHM) of the absorption line. The absorption coefficient at line centre is normalised to unity. Two dimensionless parameters are defined as

$$x = \frac{\bar{\nu} - \nu_0}{\gamma_L} \quad (2.31)$$

$$m = \frac{a}{\gamma_L} \quad (2.32)$$

where  $m$  is the modulation index and the absorption coefficient becomes

$$k_L(x, m) = \frac{1}{1 + (x + m \cos \omega t)^2} \quad (2.33)$$

The second harmonic (Fourier coefficient) for the Lorentzian lineshape is given by

$$H_2(x, m) = \frac{2}{\pi} \int_0^\pi \frac{\cos 2\theta}{1 + (x + m \cos \theta)^2} d\theta \quad (2.34)$$

The first three harmonic signals are calculated and shown in Fig 2.7. The shape of  $H_n$  depends on both the absorption lineshape function and the modulation index.

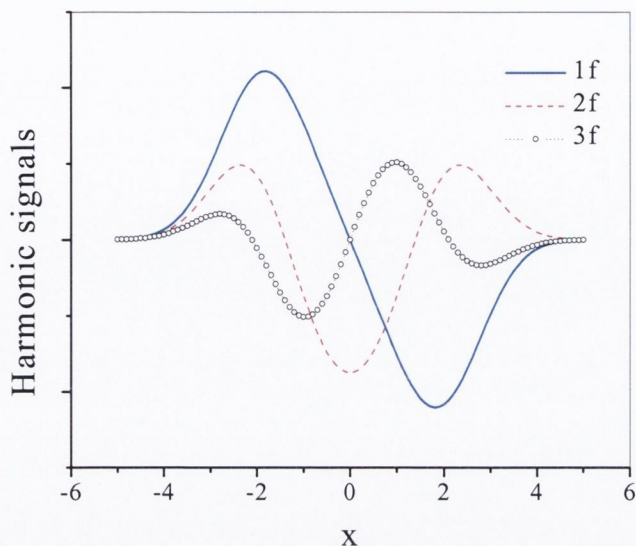


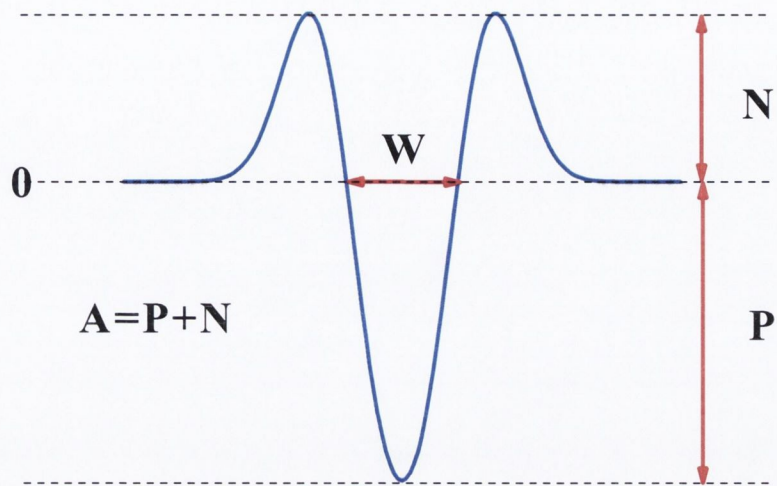
**Figure 2.7** Calculated harmonic signal for a Lorentzian line. ( $m=2.2$ )

## 2f Lineshape and modulation index

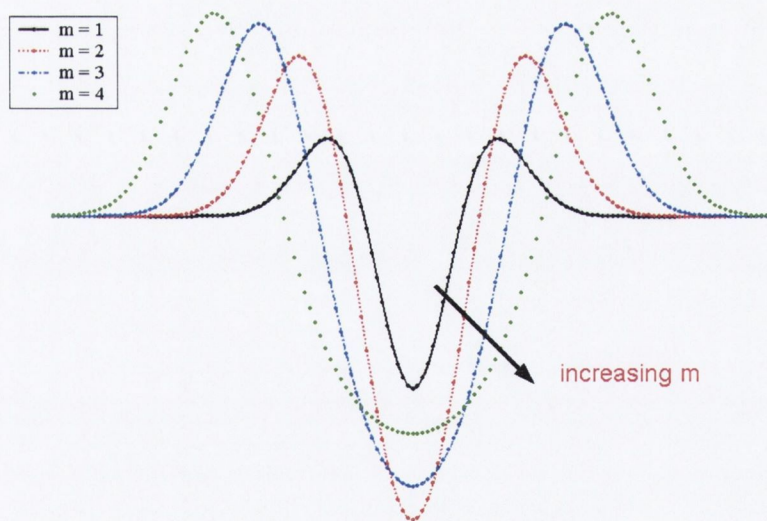
Harmonic signals, described by Eq. 2.34, depend on both the absorbance  $\alpha$  (including the specific absorption lineshape) and the modulation index  $m$ .  $2f$  lineshape is often characterised by its positive peak (P), negative peak (N), width (W), and the total signal amplitude (A) as shown in Fig. 2.8a. The effects of modulation index  $m$  on the  $2f$  signals (of a Lorentzian absorption line) are illustrated in Fig. 2.8(b). When  $m$  increases, W increases due to the modulation broadening effect [3]. P and A increase with  $m$  when  $m \leq 2$ , then decrease at larger values of  $m$ . When  $m$  is larger than an optimum value, the  $2f$  signal spreads out in frequency rather than building up in amplitude.

Variations in  $2f$  parameters of a Lorentzian absorption line over a range of  $m$  are calculated and shown in Fig. 2.9. Note that for a Lorentzian absorption line, the maximum positive peak (P) and the total amplitude (A) occur at  $m = 2.2$  and  $3.1$ , respectively.  $2f$  parameters for absorption lines with other profiles can be calculated similarly.





(a)



(b)

**Figure 2.8** (a) Definition of 2f lineshape parameters (b) Calculated 2f lineshape at various values of modulation index  $m$ .

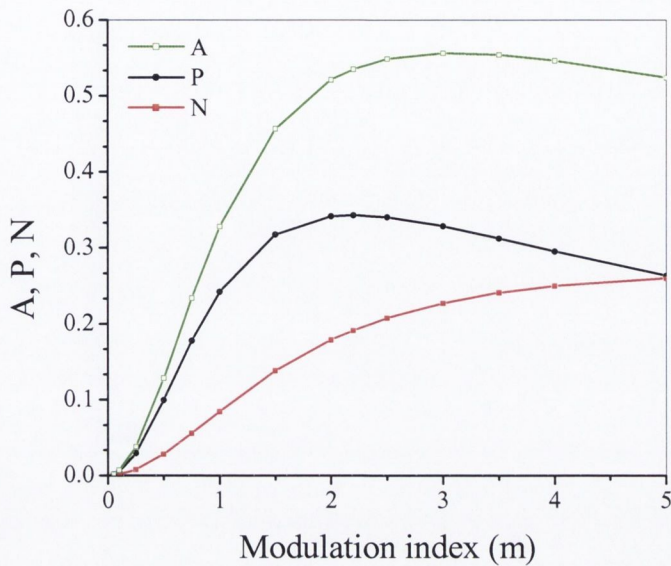


**Figure 2.9.** Calculated  $2f$  parameters of a Lorentzian absorption line at various values of  $m$ .

### Limiting Factors in WMS technique.

There are two limiting factors in WMS, which might prevent shot noise limited sensitivity, they are residual amplitude modulation (RAM) and Fabry-Perot fringes. In semiconductor lasers a change in the real part of the refractive index due to a change in carrier density is accompanied by a corresponding change in the imaginary part, and this is expressed by the phase-amplitude coupling coefficient ( $\alpha_H$ -parameter) defined as,

$$\alpha_H = \frac{2\omega}{c} \frac{dn/dN}{dg/dN} \quad (2.35)$$

where  $n$  is the real part of the refractive index,  $g$  is the imaginary part of the refractive index,  $c$  is the speed of light,  $N$  is the carrier density and  $\omega$  the angular frequency. Therefore in addition to the modulation of optical frequency, the current modulation



induces an intensity modulation. When RAM is larger than the absorption signal the detection becomes RAM-limited. Non-linearity in the output power versus current characteristics of the laser diode also gives rise to an unwanted RAM contribution to the WMS harmonic signal even in the absence of absorption by the target gas. It results in an offset in the detected WMS signal at the fundamental frequency  $f$ .

Also of note is at low modulation frequencies ( $< 10$  MHz) the temperature of the laser diode is also modulated by the current modulation. Since the refractive index varies with temperature, the laser wavelength is also modulated via this thermal effect. The temperature and carrier effects are opposite in sign. The total modulation amplitude of the laser optical frequency is the sum of these two contributions.

Fabry-Perot fringes, due to interference of transmitted and partially reflected fields between two surfaces, are commonly observed in laser spectroscopy [26, 27]. These fringes are characterised by the Airy function [28]

$$\frac{I_t}{I_i} = \frac{1}{1 + F \sin^2(2\pi\nu nD/c)} \quad (2.36)$$

where  $I_i$  is the maximum transmitted intensity,  $D$  the distance between the two reflecting surfaces, and  $n$  is the refractive index of the medium between the reflecting surfaces. A coefficient  $F$  describing the reflectivity of the surfaces is defined as

$$F = \left( \frac{2r}{1-r^2} \right)^2 \quad (2.37)$$

where  $r$  is the surface reflectivity intensity. The frequency spacing between two fringe peaks, denoted by

$$\Delta\nu = \frac{c}{2nD} \equiv FSR \quad (2.38)$$

is the free spectral range (FSR). The amplitude of the fringes can be reduced by angular mis-alignment and the use of reflective and anti-reflection coated optics. However fringes due to small reflections can be readily detected, a surface reflectivity of  $3 \times 10^{-5}$  results in

a change of  $\sim 10^{-4}$  in the transmitted intensity, which is orders of magnitude larger than the small signals to be measured.

### 2.7.3 FMS

The main advantage of FMS over WMS is that noise is much less at higher frequencies. Many excellent theoretical descriptions of FMS can be found in the literature [20, 29-31], a summary of which is briefly given here. For FMS, the laser is modulated at high frequency  $\omega_m$  ( $\omega_m > \gamma$  (HWHM)), and the instantaneous electric field of the laser output can be described as

$$E(t) = E_0 \left\{ 1 + M \sin(\omega_m t + \psi) \exp\left(i\omega_0 t + i\beta \sin(\omega_m t)\right) \right\} \quad (2.39)$$

where  $\omega_m$  is the modulation frequency,  $\omega_0$  is the optical frequency,  $M$  is the amplitude modulation depth,  $\beta$  describes the phase modulation (or frequency modulation) and is usually called the frequency modulation depth, and  $\psi$  gives the phase difference between the amplitude and phase modulation.

Equation 3.5 can be transformed to an optical carrier and sidebands as

$$E(t) = E_0 e^{i\omega_0 t} \sum_{l=-\infty}^{\infty} r_l e^{il\omega_m t} \quad (2.40)$$

where

$$r_l = \frac{M}{2i} e^{i\psi} J_{l-1}(\beta) + J_l(\beta) + \frac{-M}{2i} e^{-i\psi} J_{l+1}(\beta) \quad (2.41)$$

and  $J_l(\beta)$  is the  $l^{\text{th}}$  order Bessel function. For FMS,  $\beta$  is typically much less than unity, and thus the only significant components in the expansion are the carrier ( $l=0$ ) and the first order sideband pair ( $l = \pm 1$ ), as illustrated in Fig 2.10. If the amplitude modulation effect is negligible then  $M=0$ , and

$$r_l = J_l(\beta) = -J_{-l}(\beta) = -r_{-l} \quad (2.42)$$



the two side-bands have the same amplitude, but they are 180° out of phase. A gas absorption line will act on each of the above frequency components with an amplitude and phase response  $\alpha(\omega)$  and  $\varphi(\omega)$ . The demodulated signal can be obtained by squaring  $E(t)$ , retaining only those components at the demodulation frequency ( $\omega$  for first harmonic detection,  $n\omega$  for  $n$ th harmonic). This gives a complex amplitude of

$$Q = 2Ze^{i\theta}$$

$$Z = \sum_l r_l r_{l-n}^* \exp\left\{-\alpha(\omega_0 + l\omega_m)/2 - \alpha(\omega_0 + (l-n)\omega_m)/2\right\} \quad (2.43)$$

$$\exp\left\{-i\varphi(\omega_0 + l\omega_m) + i\varphi(\omega_0 + (l-n)\omega_m)\right\}$$

where  $r^*$  is the complex conjugate of  $r$ . The detector phase angle  $\theta$  relates the phase of the detected signal to that of the reference frequency in the lock-in amplifier. The in-phase component corresponds to pure absorption, and the quadrature component corresponds to dispersion. Therefore, not only the absorption but also the dispersion information may be obtained. Fig 2.11 shows calculated absorption and dispersion waveforms for first-harmonic detection of a Gaussian absorption line as a function of increasing modulation frequency.

In the near-infrared region, the Doppler HWHM of molecular transitions are ~100-300MHz. Thus FMS implies a modulation frequency  $\omega_m$  in the 100MHz-GHz range. Even higher  $\omega_m$  may be required when the transition is pressure-broadened. This high frequency is more effective in avoiding excess laser noise and can achieve sensitivity near the shot noise limit. Table 2.1 lists important features of WMS and FMS techniques for comparison. The instrumentation of an FMS system, includes high-speed detectors and RF circuit components, which becomes expensive.

	WMS	FMS
$\omega_m$	$\ll \Delta\nu$	$\geq \Delta\nu$
Modulation index	$>1$	$<1$
Side bands	Multiple	1 pair
Harmonic detection	Usually $2f$	$1f$
Instrumentation	Easy	Difficult
Cost	Low	High
$\alpha_{\min}$	$1 \times 10^{-6}$	$1 \times 10^{-7}$

**Table 2.1** Comparisons of WMS and FMS

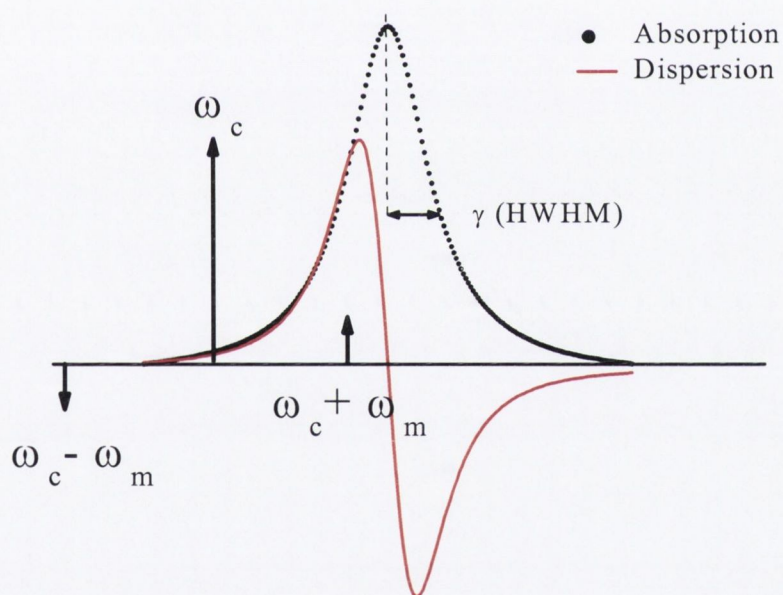
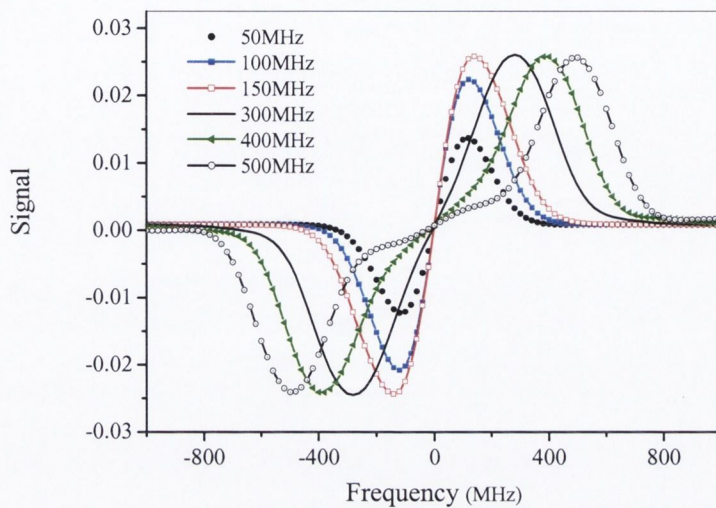
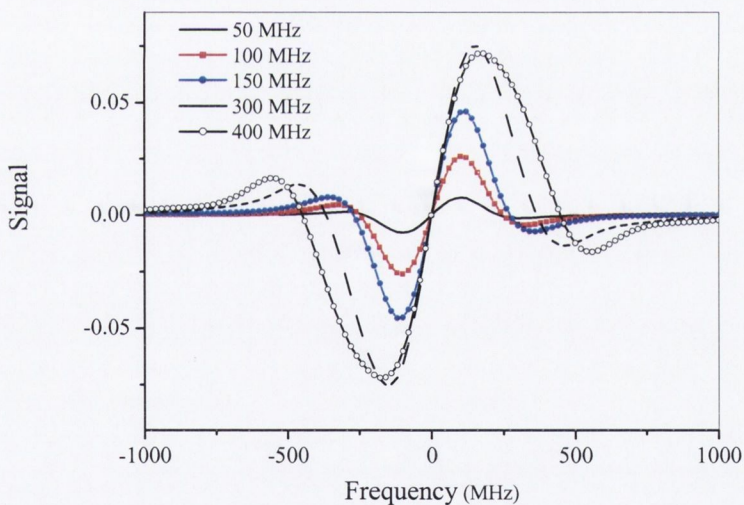


**Figure 2.10.** Spectral view of FMS





(a)



(b)

**Figure 2.11** Calculated absorption (a) and dispersion (b) waveforms for first-harmonic detection of a Gaussian absorption line as a function of increasing modulation frequency. The HWHM of the Gaussian lineshape is 150MHz. At modulation frequencies much greater than the linewidth, the absorption peaks are separated by approx twice the modulation frequency.

## 2.8 References.

- [1] L. S. Rothman, C. P. Rinsland, A. Goldman, S. T. Massie, D. P. Edwards, J. M. Flaud, A. Perrin, C. Camy-Peyret, V. Dana, J. Y. Mandin, J. Schroeder, A. McCann, R. R. Gamache, R. B. Wattson, K. Yoshino, K. V. Chance, K. W. Jucks, L. R. Brown, V. Nemtchinov, and P. Varanasi, "The HITRAN molecular spectroscopic database and HAWKS (HITRAN Atmospheric Workstation): 1996 edition," *Journal of Quantitative Spectroscopy & Radiative Transfer*, vol. 60, pp. 665-710, 1998.
- [2] L. S. Rothman, A. Barbe, D. C. Benner, L. R. Brown, C. Camy-Peyret, M. R. Carleer, K. Chance, C. Clerbaux, V. Dana, V. M. Devi, A. Fayt, J. M. Flaud, R. R. Gamache, A. Goldman, D. Jacquemart, K. W. Jucks, W. J. Lafferty, J. Y. Mandin, S. T. Massie, V. Nemtchinov, D. A. Newnham, A. Perrin, C. P. Rinsland, J. Schroeder, K. M. Smith, M. A. H. Smith, K. Tang, R. A. Toth, J. Vander Auwera, P. Varanasi, and K. Yoshino, "The HITRAN molecular spectroscopic database: edition of 2000 including updates through 2001," *Journal of Quantitative Spectroscopy & Radiative Transfer*, vol. 82, pp. 5-44, 2003.
- [3] R. M. Measures, *Laser Remote Chemical Analysis*, vol. 94: John Wiley & sons, 1988.
- [4] N. Jacquinet-Husson, E. Arie, J. Ballard, A. Barbe, G. Bjoraker, B. Bonnet, L. R. Brown, C. Camy-Peyret, J. P. Champion, A. Chedin, A. Chursin, C. Clerbaux, G. Duxbury, J. M. Flaud, N. Fourrie, A. Fayt, G. Graner, R. Gamache, A. Goldman, V. Golovko, G. Guelachvili, J. M. Hartmann, J. C. Hilico, J. Hillman, G. Lefevre, E. Lellouch, S. N. Mikhailenko, O. V. Naumenko, V. Nemtchinov, D. A.



- Newnham, A. Nikitin, J. Orphal, A. Perrin, D. C. Reuter, C. P. Rinsland, L. Rosenmann, L. S. Rothman, N. A. Scott, J. Selby, L. N. Sinitza, J. M. Sirota, A. M. Smith, K. M. Smith, V. G. Tyuterev, R. H. Tipping, S. Urban, P. Varanasi, and M. Weber, "The 1997 spectroscopic GEISA databank," *Journal of Quantitative Spectroscopy & Radiative Transfer*, vol. 62, pp. 205-254, 1999.
- [5] M. E. Webber, S. Kim, S. T. Sanders, D. S. Baer, R. K. Hanson, and Y. Ikeda, "In situ combustion measurements of CO<sub>2</sub> by use of a distributed-feedback diode-laser sensor near 2.0 μm," *Applied Optics*, vol. 40, pp. 821-828, 2001.
- [6] P. W. Miloni. and J. E. Eberely, *Lasers*: John Wiley & Sons, 1988.
- [7] Schalow and Townes, *Microwave Spectroscopy*: Dover Publications, 1975.
- [8] Demtroder, *Laser Spectroscopy*, 2<sup>ed</sup>. Berlin: Springer Verlag, 1998.
- [9] J. Humlicek, "An efficient method for evaluation of the complex probability function: the Voigt function and its derivative," *J Quant Spectrosc Radiat Transfer*, vol. 21, pp. 309-313, 1979.
- [10] R. H. Dicke, "The effects of Collisions upon the Doppler Width of Spectral Lines," *Physical Review*, vol. 89, pp. 472-305, 1953.
- [11] L. Galatry, "The Effects of Collisions upon the Doppler Width of Spectral Lines," *Physical Review*, vol. 122, pp. 1218-1223, 1961.
- [12] M. Lepere, "Line profile study with tunable diode laser spectrometers," *Spectrochimica Acta Part A: Molecular and Biomolecular Spectroscopy*, vol. In Press, Corrected Proof.
- [13] W. Ruyten, "Comment on "A new implementation of the Humlicek algorithm for the calculation of the Voigt profile function" by M. Kuntz JQSRT 57(6) (1997)

819-824," *Journal of Quantitative Spectroscopy & Radiative Transfer*, vol. 86, pp. 231-233, 2004.

- [14] P. L. Varghese and R. K. Hanson, "Collisional narrowing effects on spectral line shapes measured at high resolution," *Appl Opt*, vol. 23, pp. 2376-2385, 1983.
- [15] X. Ouyang and P. L. Varghese, "Reliable and Efficient Program for Fitting Galatry and Voigt Profiles to Spectral Data on Multiple Lines," *Applied Optics*, vol. 28, pp. 1538-1545, 1989.
- [16] E. Rosencher. and. B. Vinter, *Optoelectronics*: Cambridge University Press, 2002.
- [17] Yariv, *Quantum Electronics*: Wiley, 1989.
- [18] P. Signoret, M. Myara, J.-P. Turrenc, B. Orsal, M.-H. Monier, J. Jacquet, P. Leboudec, and F. Marin, "Bragg section effects on linewidth and lineshape in 1.55  $\mu\text{m}$  DBR tunable laser diodes," *Photonics Technology Letters, IEEE*, vol. 16, pp. 1429-1431, 2004.
- [19] D. S. Bomse, A. C. Stanton, and J. A. Silver, "Frequency-Modulation and Wavelength Modulation Spectroscopies - Comparison of Experimental Methods Using a Lead-Salt Diode-Laser," *Applied Optics*, vol. 31, pp. 718-731, 1992.
- [20] J. A. Silver, "Frequency-Modulation Spectroscopy for Trace Species Detection - Theory and Comparison among Experimental Methods," *Applied Optics*, vol. 31, pp. 707-717, 1992.
- [21] J. Reid and D. Labrie, "Second-Harmonic Detection with Tunable Diode Lasers - Comparison of Experiment and Theory," *Applied Physics*, vol. B, pp. 203-210, 1981.



- [22] P. Kluczynski, J. Gustafsson, A. M. Lindberg, and O. Axner, "Wavelength modulation absorption spectrometry - an extensive scrutiny of the generation of signals," *Spectrochimica Acta Part B-Atomic Spectroscopy*, vol. 56, pp. 1277-1354, 2001.
- [23] P. Kluczynski, A. M. Lindberg, and O. Axner, "Background signals in wavelength-modulation spectrometry with frequency-doubled diode-laser light. I. Theory," *Applied Optics*, vol. 40, pp. 783-793, 2001.
- [24] P. Kluczynski, A. M. Lindberg, and O. Axner, "Background signals in wavelength-modulation spectrometry with frequency-doubled diode-laser light. II. Experiment," *Applied Optics*, vol. 40, pp. 794-805, 2001.
- [25] K. Boylan, "The Application of Tunable and Widely Tunable Single Frequency Laser Diodes to Trace Gas Detection in the near infrared," M.Sc thesis, Trinity College Dublin, 2000,.
- [26] H. C. Sun and E. A. Whittaker, "Novel Etalon Fringe Rejection Technique for Laser-Absorption Spectroscopy," *Applied Optics*, vol. 31, pp. 4998-5002, 1992.
- [27] N. Kagawa, O. Wada, and R. Koga, "Suppression of the etalon fringe in absorption spectrometry with an infrared tunable diode laser," *Optical Engineering*, vol. 36, pp. 2586-2592, 1997.
- [28] Hecht, *Optics*, 4th ed: Addison Wesley, 2003.
- [29] U. Gustafsson, G. Somesfalean, J. Alnis, and S. Svanberg, "Frequency-modulation spectroscopy with blue diode lasers," *Applied Optics*, vol. 39, pp. 3774-3780, 2000.

- [30] H. Riris, C. B. Carlisle, D. F. McMillen, and D. E. Cooper, "Explosives detection with a frequency modulation spectrometer," *Applied Optics*, vol. 35, pp. 4694-4704, 1996.
- [31] G. C. Bjorklund, W. Zapka, M. D. Levenson, A. C. Tam, W. Lenth, F. M. Schellenberg, T. F. Gallagher, R. Kachru, and F. Gounand, "Recent Progress in Frequency-Modulation Spectroscopy," *Applied Physics B-Photophysics and Laser Chemistry*, vol. 28, pp. 299-300, 1982.



# Chapter 3

## Widely Tuneable Semiconductor Lasers

### 3.1 Introduction

The main aim of this chapter is to give an overview of the monolithically integrated tuneable laser diodes that were commercially available during the course of this work and are considered suitable for applications in multi-gas sensing. For a more thorough review of integrated tuneable laser diodes, the reader is referred to the excellent book by Amann and Buus [1]. All of these tuneable lasers consist of a longitudinal integration of sections with different functionality. Typically, one has an active section providing the optical gain for the laser oscillator, one or more filter sections with a frequency selective reflection characteristic, and a phase shifter section for fine-tuning of the cavity resonance frequencies [2].

Widely tuneable laser diodes are very attractive for molecular spectroscopy because their tuning ability allows scanning of a large spectral interval, which makes it possible to detect several species of a gas mixture simultaneously. Commercially available widely tuneable laser diodes are optimised for the communications market, which favours other parameter settings of the laser device than those desired for spectroscopic use [3]. To improve the performance of semiconductor lasers for multi-gas sensing, parameters such as wide and mode-hop-free wavelength tuning, narrow laser linewidth, high FM/AM index ratio and the side mode suppression ratio should be optimised.

In the first section of this chapter, the basic concepts for the tuneable lasers are described. The distributed feedback and distributed Bragg reflector lasers are then introduced followed by more advanced laser structures for achieving a wide tuning range. Two such lasers are discussed, the sampled grating distributed Bragg reflector and the modulated grating Y-branch laser. These are the devices used throughout this thesis and so an overview of their tuning operation is presented. The relevant physical mechanisms enabling electronic control of the emission frequency of monolithic semiconductor lasers are presented. Finally the main requirements for the application of tuneable laser diodes to gas sensing are outlined.



### 3.2 Basic Concept of tuneable laser

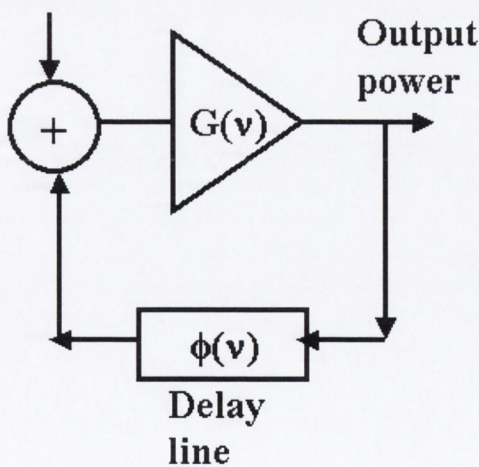
For laser operation at a frequency  $\nu$  two requirements need to be fulfilled simultaneously: the roundtrip cavity gain  $G(\nu)$  should be unity and the roundtrip phase  $\phi(\nu)$  should be an integer multiple of  $2\pi$ .

$$G(\nu) = r_1 r_2 \exp(-2i\beta L) = 1 \quad (3.1)$$

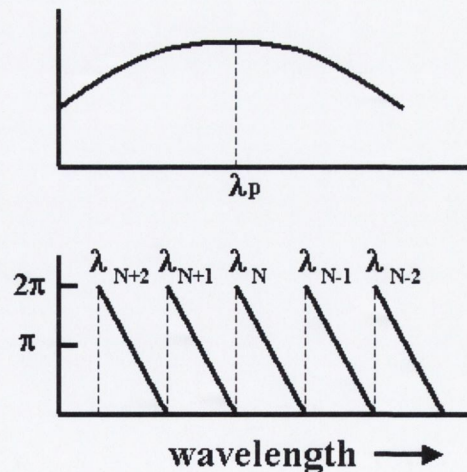
$$\phi(\nu) = \frac{2\pi\nu}{c} 2 \sum_l n_l L_l = 2\pi \quad (3.2)$$

here  $c$  is the speed of light in vacuum,  $r_1 r_2$  are the mirror power reflectivity and  $\beta$  is the propagation constant. The summation over  $l$  represents the optical length of the laser cavity, i.e. the sum of the optical lengths of the different concatenated sections. The phase condition defines the set of discrete frequencies  $\nu_k$ , the so-called cavity modes. The laser will oscillate at the frequency  $\nu_n$  among this set of frequencies which requires minimal pumping of the laser to fulfil the gain condition  $G(\nu)=1$ . Fig 3.1 shows a simplified equivalent circuit of a laser oscillator. It consists of the cavity roundtrip gain and the phase shifting function by the cavity transit time, and the spontaneous emission input. The oscillator amplitude and phase conditions are depicted schematically in Fig 3.1 (b), where the frequency of the dominant laser mode is roughly defined to within  $\Delta\lambda/2$  by the gain peak frequency  $\nu$  of the cavity roundtrip gain  $G(\nu)$ .

**Spontaneous emission**



(a)



(b)

**Figure 3.1** Simplified equivalent model of a laser, (b) cavity gain curve versus phase shift [1].



If we look at the above model in Fig. 3.1 (a), we will find that the tuning of the laser frequency can be done either by varying the cavity roundtrip gain characteristic or by adjusting the phase shift, or by varying both parameters. This is the basic principle of the tuneable laser.

### 3.3 Wave propagation in periodic structures

After introducing the basic concept of the tuneable laser, we now give an overview of the gratings used to create single-mode operation in semiconductor lasers over wide tuning ranges. A summary of Buus's analysis in chapter 3, section 3.2 [1] is outlined here. The aim of the analysis is to illustrate the reflection variation as the wavelength is varied about the Bragg frequency of a grating. All transverse and lateral directions are neglected in this analysis. The refractive index of the periodic grating varies according to

$$n(z) = n'_{eff} + \frac{\Delta n}{2} \cos(2\beta_0 z) \quad (3.3)$$

It is assumed that the amplitude of the periodic term is smaller than the steady term, which represents the real part of the effective refractive index  $n_{eff}$  of the structure without the grating. The Bragg propagation constant  $\beta_0$  is related to the grating period by

$$\beta_0 = \frac{M\pi}{\Lambda} = \frac{2\pi}{\lambda_B} n'_{eff} \quad (3.4)$$

where  $\lambda_B$  is the Bragg wavelength in free space and  $M$  is the period order. For a first order grating we have

$$\Lambda = \frac{\lambda_B}{2n'_{eff}} \quad (3.5)$$

which simply means the period is equal to half a wavelength in the structure. The model is based on the scalar wave equation for the electric field

$$\frac{\partial E}{\partial z^2} + (n(z)k)^2 E = 0 \quad (3.6)$$

where  $E$  is the complex amplitude of the field with frequency  $\nu$  and  $k=2\pi\nu/c$  is the free space propagation constant. Using  $\beta = n_{eff}k$

$$\left( n(z) \frac{2\pi}{\lambda} \right)^2 = \beta^2 + 4\beta\kappa \cos(2\beta_0 z) \quad (3.7)$$

The new term introduced here is the coupling coefficient  $\kappa$ , a useful and important parameter in describing periodic grating structures. The coupling coefficient is given by

$$\kappa = \frac{\pi \Delta n}{\lambda} \quad (3.8)$$

and describes the amount of reflection per unit length. Only wavelengths close to the Bragg wavelength are considered and hence  $\Delta\beta = \beta - \beta_0$  is the deviation from the Bragg wavelength. These are the two counter-propagating waves, which are coupled due to the Bragg scattering. We can therefore expand the electric field in the forward and backward propagating modes

$$E(z) = R(z) \exp(-j\beta_0 z) + S(z) \exp(j\beta_0 z) \quad (3.9)$$

where the functions  $R(z)$  and  $S(z)$  vary slowly as a function of  $z$ , so that their second derivatives in equation 3.6 can be neglected. If we insert equation 3.9 into the wave equation 3.6, take into account all the above assumptions, and collect terms with all the same phase factors  $(-j\beta_0 z)$  and  $(j\beta_0 z)$  respectively, we obtain the coupled mode equations [4],

$$\frac{dR}{dz} - (\alpha_0 - j\Delta\beta)R = -j\kappa S \quad (3.10)$$

$$\frac{dS}{dz} + (\alpha_0 - j\Delta\beta)S = -j\kappa R \quad (3.11)$$

When the coupling coefficient vanishes, these equations are simply the equations of two independent waves travelling in opposite directions.

### 3.3.1 Distributed Bragg reflectors

The basic DBR laser consists of two longitudinally integrated sections, an active section and a reflector section as shown in Fig. 3.2. The waveguide core of the active section has a bandgap matching the desired emission frequency and hence provides optical gain if sufficient carriers are injected. The core material of the reflector in contrast has a higher bandgap, such that the material is transparent (passive) for laser light. Along the reflector section, a diffraction grating is embedded in the waveguide yielding a periodic modulation of the effective refractive index of the waveguide. Because of the grating, the passive section reflects light back in a narrow frequency



band. The aim of this analysis is to illustrate the wavelength selectivity of the distributed Bragg reflector (DBR) by using the solution of the coupled mode equations.

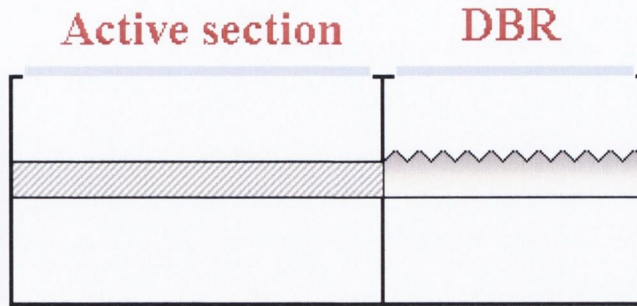


**Figure 3.2** Two-section DBR laser diode

The coupled mode equations can be solved for a periodic structure of length  $L$  and the general solution, for these form of differential equations is

$$R(L) = \left[ \cosh(\gamma L) + \frac{\alpha_0 - j\Delta\beta}{\gamma} \sinh(\gamma L) \right] R(0) - \frac{j\kappa}{\gamma} \sinh(\gamma L) S(0) \quad (3.12)$$

$$S(L) = \frac{j\kappa}{\gamma} \sinh(\gamma L) R(0) + \left[ \cosh(\gamma L) - \frac{\alpha_0 - j\Delta\beta}{\gamma} \sinh(\gamma L) \right] S(0) \quad (3.13)$$

where

$$\gamma^2 = \kappa^2 - \Delta\beta^2 \quad (3.14)$$

These equations can be written in transfer matrix form as

$$\begin{pmatrix} R(L) \\ S(L) \end{pmatrix} = F_{per}(L) \begin{pmatrix} R(0) \\ S(0) \end{pmatrix}$$

where the matrix elements of  $F_{per}$  follow directly from equations 3.12 and 3.13. If the periodic structure of length  $L$  is used as a reflector for a right-propagating wave and therefore  $S(L)=0$ , the field reflection coefficient can be written as follows using equation 3.13.

$$r_B = \frac{(F_{per})_{21}}{(F_{per})_{22}} = \frac{-j\kappa \sinh(\gamma L)}{\gamma \cosh(\gamma L) - (\alpha_0 - j\Delta\beta) \sinh(\gamma L)} \quad (3.15)$$

The results shown in Fig 3.3, show some important features of distributed Bragg reflectors: (1) the amplitude of the reflection increases with increasing  $\kappa L$ , i.e. a higher coupling coefficient leads to a stronger reflection; (2) the amplitude of the

reflection decreases with increasing  $\Delta\beta L$ , i.e. the reflection becomes smaller when the wavelength deviates from the Bragg wavelength.

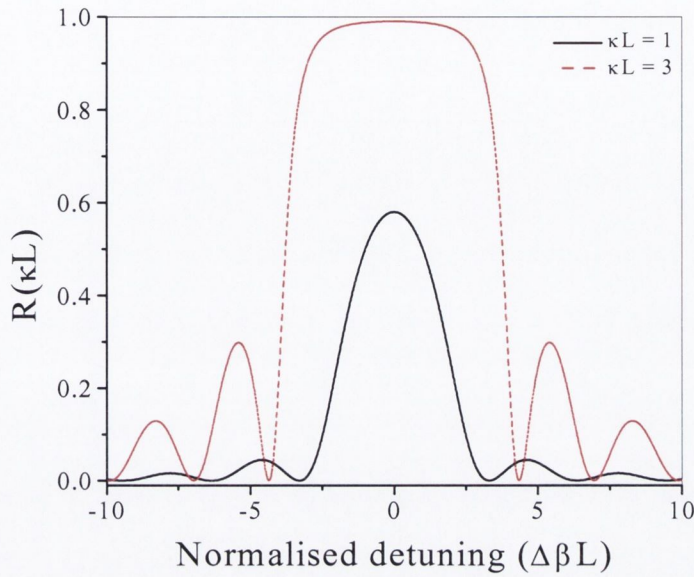


**Figure 3.3** Calculated Power reflectivity of a DBR reflector as a function of  $\Delta\beta L$ .

### 3.3.2 Distributed feedback lasers

In a DBR laser, the active region, which is providing gain, and the grating, which is providing wavelength selectivity, are separated longitudinally. In a distributed feedback laser (DFB), the feedback is not localised but, as the name suggests, is distributed along the length of the cavity (above the active medium in an index coupled structure) as shown in Fig. 3.4.

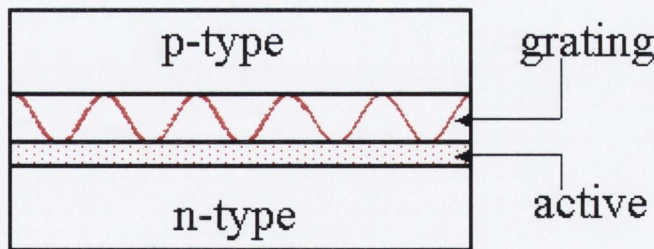


**Figure 3.4** DFB laser structure.

The analysis of a DFB laser is not as simple as for DBR lasers because the gain and phase conditions do not separate. By allowing for the presence of gain the detuning  $\Delta\beta$  now becomes



$$\Delta\beta + ig_o \quad (3.16)$$

Where  $g_o$  represents the gain for the field. The oscillation condition is

$$\cosh(\gamma L) + \frac{i(\Delta\beta + ig_o)}{\gamma} \sinh(\gamma L) = 0 \quad (3.17)$$

where  $\gamma$  now becomes

$$\gamma^2 = \kappa^2 - (\Delta\beta + ig_o)^2 \quad (3.18)$$

the oscillation condition can be written as

$$\gamma L \coth(\gamma L) = -i(\Delta\beta L + ig_o L) \quad (3.19)$$

For a given value of the coupling coefficient  $\kappa$  and length  $L$ , there exists a discrete set of eigenvalues, which corresponds to longitudinal modes with threshold gain given by  $g_o$  and wavelength determined by  $\Delta\beta$ . The solutions of Equation 3.19 can only be solved using numerical methods and the results are shown in Fig. 3.5.

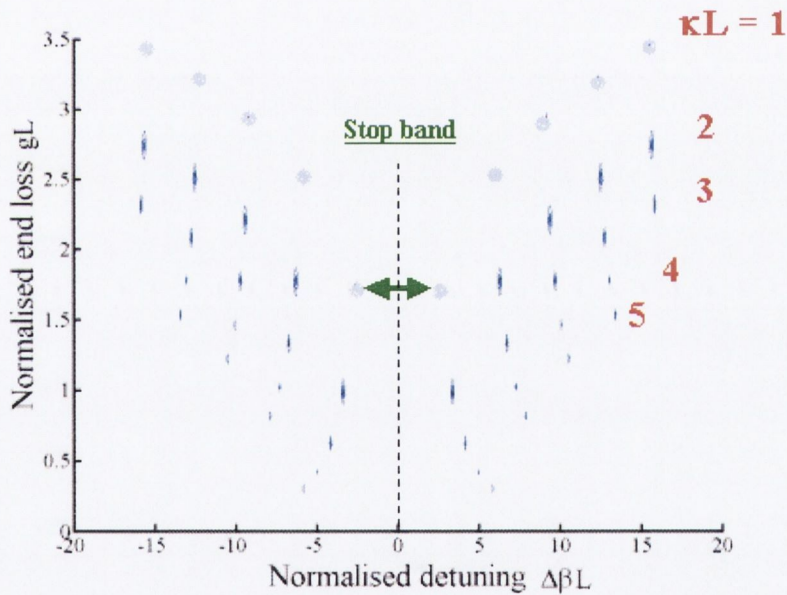


**Figure 3.5** DFB modes for different values of  $\kappa L$

Fig. 3.5 shows that there is no solution at  $\Delta\beta=0$  for the index coupled DFB laser. Note that there is a spacing between the two modes. The spacing region is called the stop band, and it has a width of  $2\kappa L$  for large values of  $\kappa L$ . The appearance of two modes with the same lowest field gain means the existence of two degenerate modes, hence single-mode operation is not possible. In order to understand why there is no solution at  $\Delta\beta=0$ , consider a simple rectangular grating as shown in Fig. 3.6.





In practice, three physical mechanisms can be used to change the refractive index of a semiconductor: injecting free carriers, applying an electric field and changing the temperature. As applying an electric field was not used here it will not be mentioned further.

### **3.4 Carrier-induced index change**

The injected electron-hole plasma is the source of a number of effects influencing the refractive index [9, 10].

#### **3.4.1 Band-filling**

The injected electrons occupy the lowest energy states in the conduction band, just as the injected holes fill the states in the valence band closest to the band edge. Consequentially, on average higher photon energies  $h\nu$  are required to excite electrons from occupied energy states in the valence band to empty energy states in the conduction band. This causes a reduction of the absorption coefficient for photon energies  $h\nu$  slightly above the nominal band-gap energy.

#### **3.4.2 Band-gap shrinkage**

Electron-Electron interactions at the densely populated states at the bottom of the conduction band reduce the energy of the conduction band edge  $E_c$ . A similar correlation effect for holes increase the energy of the valence band edge  $E_v$ . The sum of these effects causes a band-gap shrinkage, which lowers the minimum photon energy for which significant absorption occurs.

#### **3.4.3 Free-carrier absorption**

A free carrier can absorb a photon and move to a higher energy state within a band. The excess energy is released in the form of lattice vibrations as the carrier relaxes towards its equilibrium state.

#### **3.4.4 Temperature tuning**

The refractive index of III-V semiconductors also exhibits considerable temperature dependence. A well-known rule of thumb is that the emission wavelength of a single mode InGaAsP/InP laser emitting in the 1550nm region increases with temperature at a rate of approximately 0.1nm/K. Heating the entire laser cavity has the disadvantage that the threshold current increases and the differential efficiency (change in output power per unit change in drive current) decreases. Some heat is generated when



carrier-induced tuning is used, due to the non-zero resistance of the tuning diode and the non-radiative recombination process. It should be noted that the carrier effects decrease the refractive index, whereas the thermal effects increase the refractive index. This ultimately limits the tuning range achievable using carrier injection.

The amount of tuning depends on how much the refractive index can be changed, typical values for the fractional change in the refractive index is a few percent [5]. This gives a limitation for the DFB/DBR structures on the tuning range,

$$\frac{\Delta\lambda}{\lambda} = \frac{\Delta n}{n} \approx 1-2\% \quad \Delta\lambda = 10\text{nm} \quad (3.22)$$

In the next section a number of ways for overcoming this limitation are outlined.

### 3.5 Extending the tuning range of DBR-type lasers

The tuning range of conventional DFB and DBR lasers is approximately 5-10nm which is significantly smaller than the available gain bandwidth of multiple quantum well semiconductor lasers (more than 100nm) and Erbium doped fibre amplifiers (about 40nm in the C or L band) [11]. Consequently, much research has targeted the development of integrated lasers with extended tuning ranges beyond the refractive index limit [12-23]. The basic principle behind all schemes that have been developed for wide tuning is that a refractive index difference is changed rather than the index itself. Therefore, the relative wavelength change is equal to a relative change in index difference, which can be significantly larger for similar absolute refractive index variations. In the following sections we will describe the most common scheme for achieving the broad tuning range.

#### 3.5.1 Vernier effect between two comb reflectors

The Vernier caliper is a well-known instrument for high-resolution length measurement. The same principle can be applied to a tuneable laser (Fig. 3.7) if the laser has two mirrors with a comb-shaped reflectivity spectrum. The mirrors are designed such that the peak reflectivity spacing of the front mirror ( $\delta_f$ ) and the rear mirror ( $\delta_r$ ) differ by a small amount. Lasing can then only occur in the frequency range where the two peaks coincide, since the round-trip loss is inversely proportional



to the product of both mirror reflectivities. The phase section can be used to adjust the longitudinal modes, such that a mode can be aligned with the loss minimum. The coincidence of two particular peaks is often called a “super-mode” and the large frequency changes observed when applying the Vernier tuning mechanism are consequently called super-mode jumps. Intermediate tuning, from one longitudinal mode to the next, is obtained by tuning both reflectors simultaneously. Quasi-continuous tuning over a wide tuning range involves the synchronised adjustment of both the reflectors and the phase section.

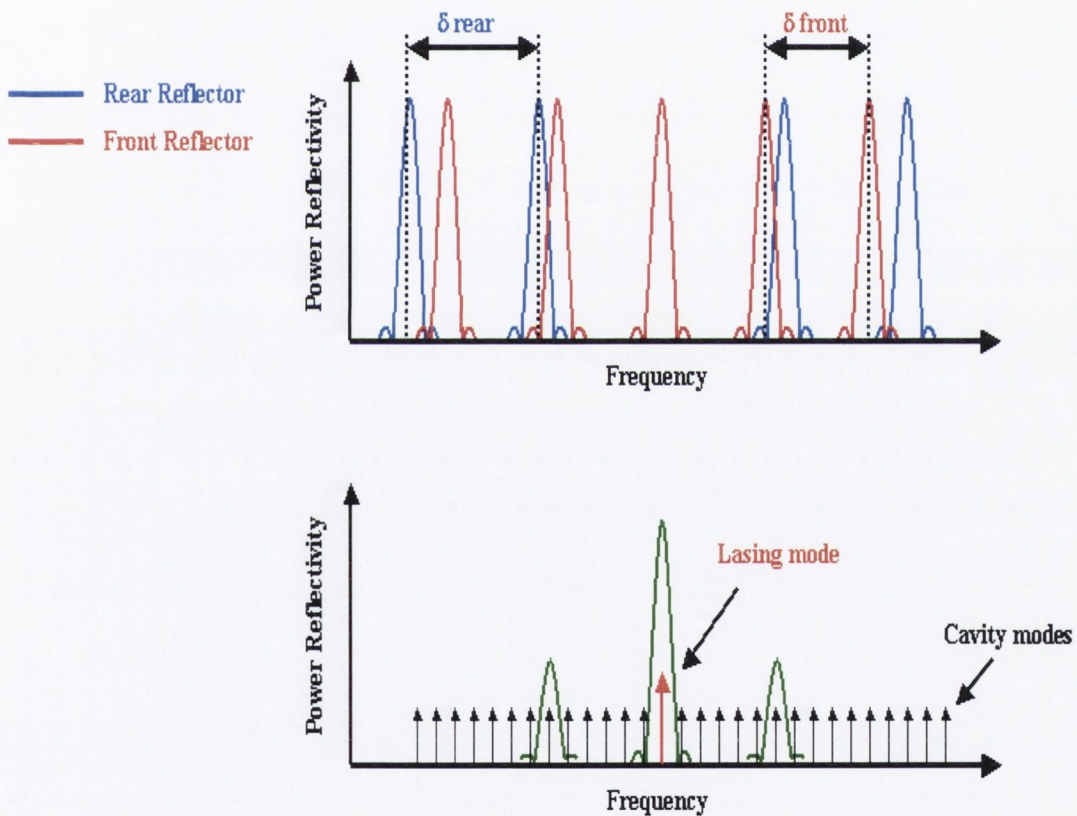


**Figure 3.7** Vernier principle applied to a tuneable laser which has two mirrors with comb-shaped reflectivity spectrums with different pitches. Lasing occurs in the frequency range where the reflection peaks coincide.

### 3.5.2 Sampled Grating DBR

The sampled grating (SG) is technologically the simplest way to produce a reflectivity spectrum that has periodic maxima [24]. The device consists of four independently biased sections; two sampled gratings, a passive phase section and a gain section as illustrated in Fig 3.8.

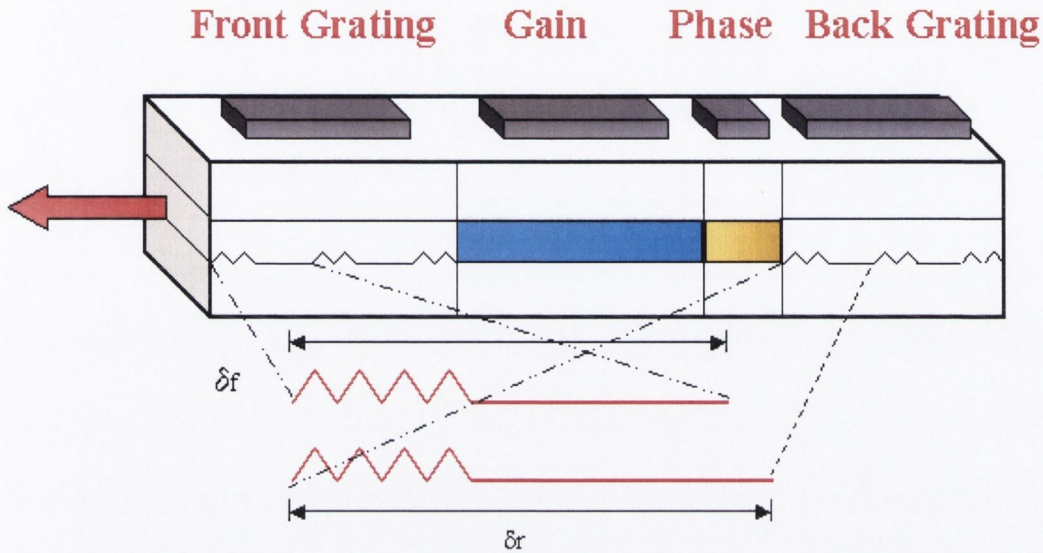


**Figure 3.8** Four section SG-DBR laser diode consisting of two sampled grating regions a phase section and a gain section. The front and back grating sections have different periods.

A “sampled grating” consists of a conventional uniform grating with grating elements periodically removed along its length. A qualitative idea of the shape of the reflectivity spectrum can easily be derived from coupled mode theory, which says that every spatial Fourier component of the refractive index modulation contributes a peak to the reflection spectrum [12]. The Fourier components of the sampled grating are obtained by convoluting the Fourier transforms of the uniform grating and the sampling function. The uniform grating has a single Fourier component with a coupling strength  $\kappa_u$  given by (3.8), at a spatial frequency  $1/\Lambda$ , which corresponds to the Bragg frequency  $\nu_B$  according to (3.5). The Fourier transform of the sampling function on the other hand consists of a comb of peaks with a spatial frequency spacing  $1/\Lambda_s$ .



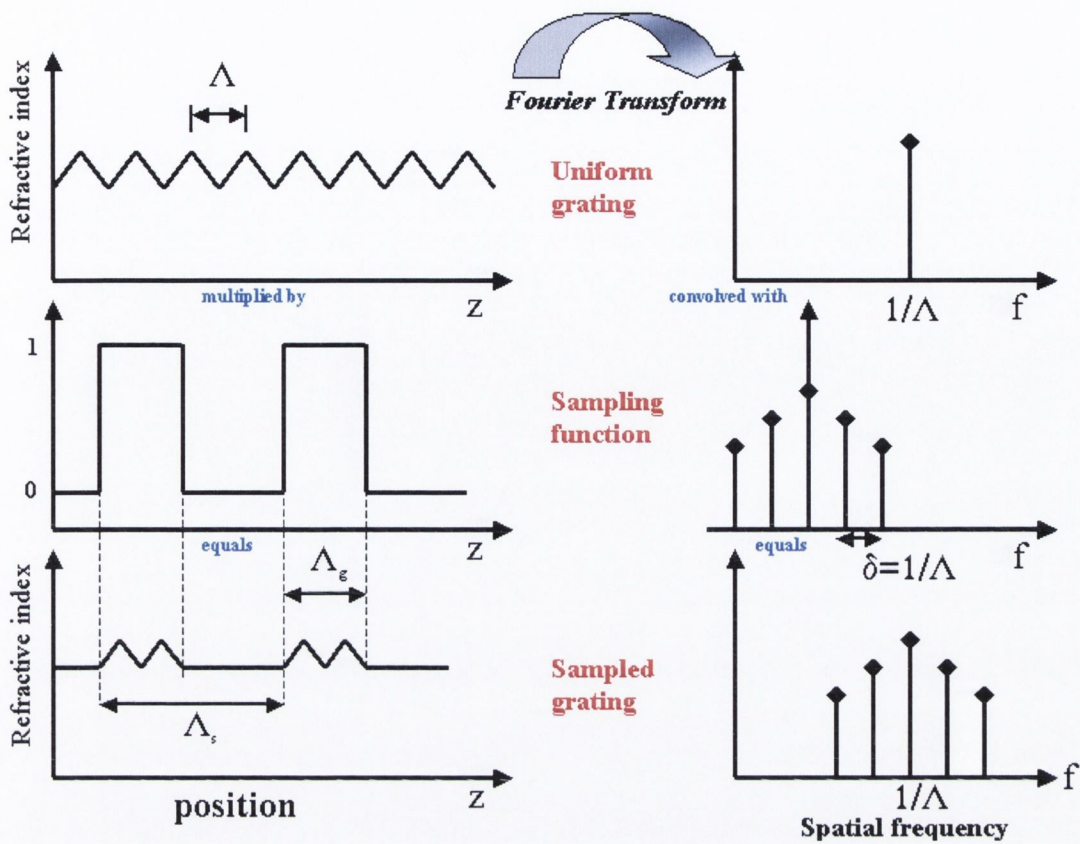


Figure 3.9 Principle of the sampled grating [12].

The modulation function is given by ( $l$  is an integer)

$$F(z) = \begin{cases} 1 & l\Lambda_s < z < l\Lambda_s + \Lambda_g \\ 0 & l\Lambda_s + \Lambda_g < z < (l+1)\Lambda_s \end{cases} \quad (3.23)$$

From which the amplitudes of the Fourier components are easily obtained as

$$F_k = \frac{1}{\Lambda_s} \int_0^{\Lambda_g} F(z) e^{-i2\pi k z / \Lambda_s} dz = \frac{\Lambda_g}{\Lambda_s} \frac{\sin(\pi k \Lambda_g / \Lambda_s)}{\pi k \Lambda_g / \Lambda_s} e^{-i\pi k \Lambda_g / \Lambda_s} \quad (3.24)$$

The convolution of both Fourier transforms exhibits peaks centred at  $1/\Lambda$ , with spacing  $1/\Lambda_s$ , this leads to strong reflections at frequencies  $\nu_k$

$$\nu_k = \frac{c}{2n(\nu_k)} \left( \frac{1}{\Lambda} + \frac{k}{\Lambda_s} \right) \quad (3.25)$$

The reflection peak spacing is determined by the sampling period  $\Lambda_s$ ,

$$\delta = \nu_{k+1} - \nu_k = \frac{c}{2n_g \Lambda_s} \quad (3.26)$$

where  $n_g$  is the group refractive index,

$$n_g(\nu) = n(\nu) + \nu \frac{dn}{d\nu} \quad (3.27)$$

The coupling coefficients at the same frequencies  $\nu_k$  are equal to the product of the coupling coefficient of the unsampled grating  $\kappa_a$  and the Fourier components  $F_k$  of the sampling function

$$\kappa_k = \kappa_a F_k \quad (3.28)$$

The overall reflectivity is the sum of the reflectivities of individual gratings with Bragg frequencies  $\nu_k$  and coupling coefficients  $\kappa_k$

$$r(\nu) = \sum_k \frac{-j\kappa_k \sinh(\gamma_k L)}{\gamma_k \cosh(\gamma_k L) - (\alpha_0 - j\Delta\beta_k) \sinh(\gamma_k L)} \quad (3.29)$$

$$\gamma^2 = \kappa^2 + [\alpha_0 - i\Delta\beta]^2 \quad (3.30)$$

with

$$\Delta\beta_k = \frac{2\pi\nu}{c} n(\nu) - \pi \left( \frac{1}{\Lambda} + \frac{k}{\Lambda_s} \right) \quad (3.31)$$

here  $L$  is the length of the sampled grating. Fig 3.10 shows a calculated reflection spectrum from a sampled grating DBR mirror.

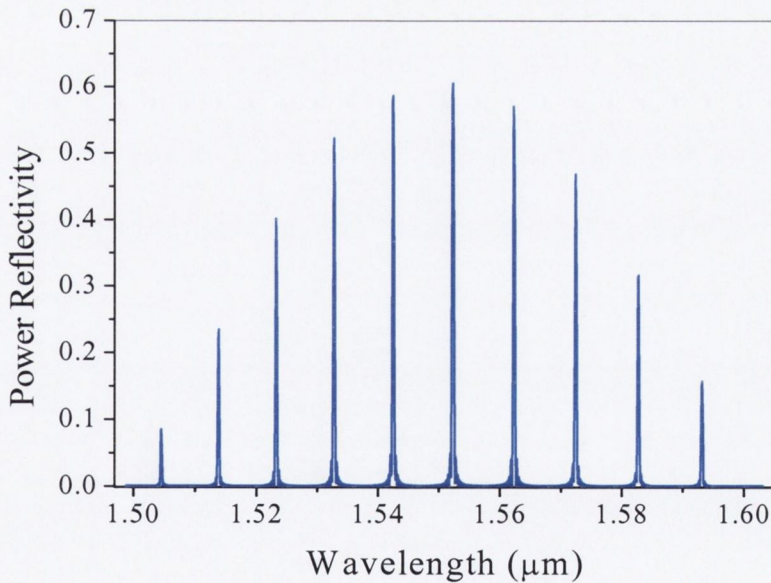


**Figure 3.10** Calculated power reflectivity spectrum of a sampled grating.



### 3.5.3 Modulated Grating Y-Laser.

Although it is technologically the simplest way to obtain a comb reflector, the sampled grating does not exhibit the optimum reflection spectrum. The shape of the sampled grating reflection spectrum as shown in Fig 3.10, above is a sinc(x) function. This is a direct consequence of the square wave nature of the sampling function applied to the grating. The above approach of periodically sampling a uniform Bragg grating in order to obtain multiple reflections peaks around the Bragg frequency can naturally be extended to other types of periodic modulation. Any modulation function that has a comb-shaped Fourier spectrum can be applied. These more general periodically modulated grating (MG) are commonly called super-structure gratings (SSG). Diagrams and analysis in this section is summarised from Buus's chapter 7 [1]. Further details can be found in [13, 25]. In the SSG mirrors the gratings are periodically chirped instead of sampled where the period of the chirp determines the peak spacing.

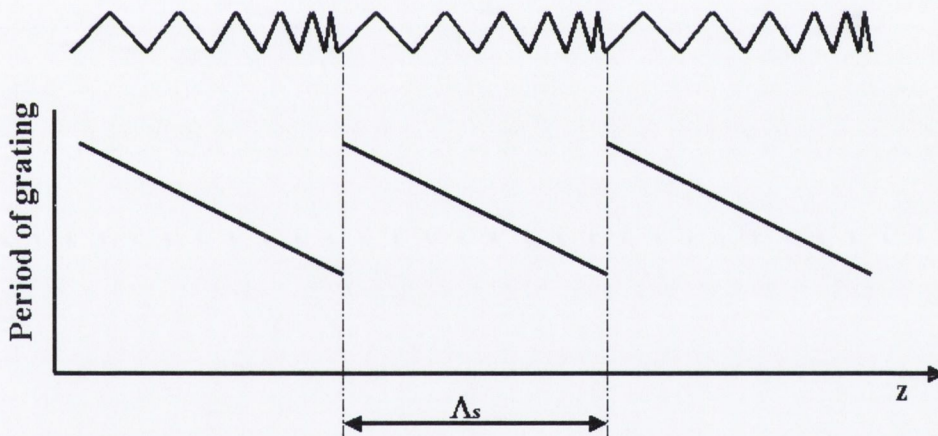


*Figure 3.11 Modulated grating with linearly varying grating period within each super period*

The advantage of this approach is that the grating occupies the entire length of the mirrors so that a much higher reflectivity can be achieved with a lower  $\kappa$  in the grating. The other main advantage is that the reflectivity of the individual peaks can be tailored such that all of the reflection peaks have the same magnitude as shown in Fig 3.12.

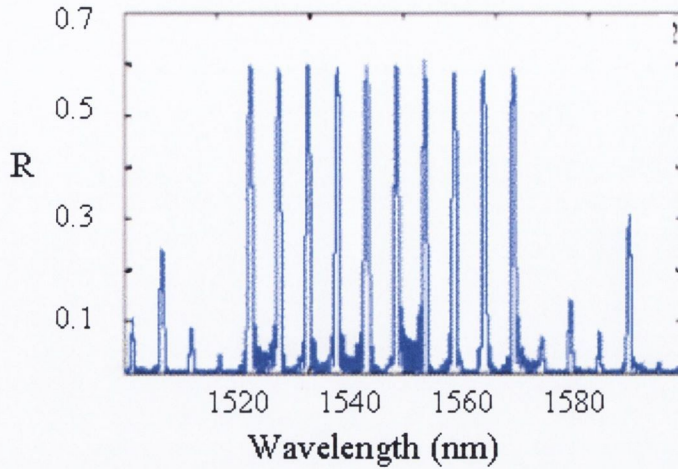


**Figure 3.12** Power reflectivity spectrum from a MG-Y Laser [26].

One of the main disadvantages with the SG-DBR is that light has to propagate through the front reflector to exit the laser. The output power will vary a lot more with tuning in these devices due to free carrier absorption in the front reflector. In the MG-Y laser this is overcome by placing the two comb reflectors on the same side of the cavity when put in the Y-branch configuration, as illustrated in Fig. 3.13, this is the concept of the MG-Y laser [26].

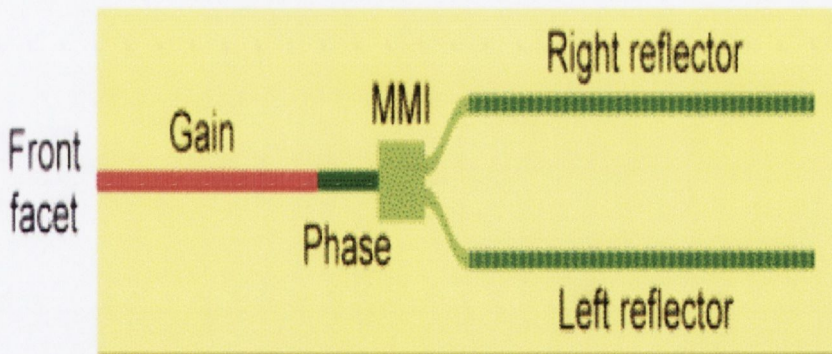


**Figure 3.13** Top view schematic of the MG-Y Laser [26].

In the MG-Y laser the different functions are separated into different sections (Fig 3.13). The gain section amplifies the light, multi-mode interferometer (MMI) splits the light into 2 equal beams, bends increase the separation between the waveguides and the reflectors filter out certain frequencies. The additive Vernier effect is used to select one lasing wavelength. Both reflectors have slightly different peak spacing so



the frequency where both peaks overlap will reach the laser threshold first. A higher side mode suppression ratio can be achieved compared with the multiplicative Vernier effect (used with the SG-DBR), because the neighbouring peaks add partly out of phase.

### **3.6 Characteristics of tuneable lasers for gas sensing.**

There are a number of standard characterisation techniques that may be applied to semiconductor lasers. These include measurements of the output power and wavelength as functions of input current and temperature and indicate the quality of the devices and hence the suitability of these lasers in gas sensing applications.

#### **3.6.1 Tuning Range**

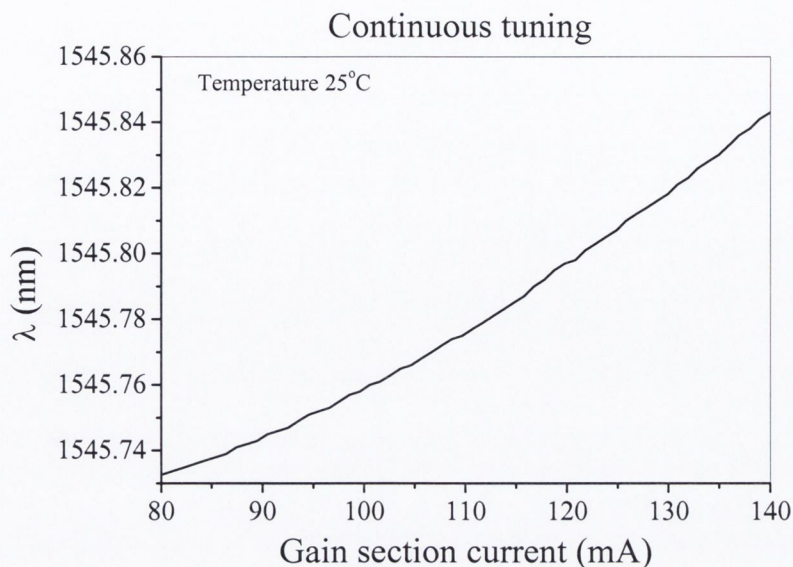
The wavelength tuning range is naturally the first characteristic by which a tuneable laser is evaluated. When tuning ranges of different lasers are compared, care has to be taken that comparisons are made on the same basis. Three different types of tuning have been identified [1]: continuous, discontinuous and quasi-continuous tuning as illustrated in Fig 3.14.

##### **Continuous tuning.**

The ideal tuning scheme for gas sensing applications is continuous tuning. In this tuning scheme the laser wavelength is tuned smoothly in arbitrarily small steps without mode change. Thereby a stable single-mode operation may be achieved throughout the entire tuning range. Owing to the stringent requirements that the same cavity mode has to remain the lasing mode across the entire tuning range, this tuning range is the smallest and is normally around 5nm.

##### **Discontinuous tuning**

Larger tuning ranges may be achieved by allowing for longitudinal mode hops during tuning. In this discontinuous tuning range, tuning ranges up to about 100nm have been obtained [27]. Unfortunately it is impossible with this tuning scheme to access



(a)

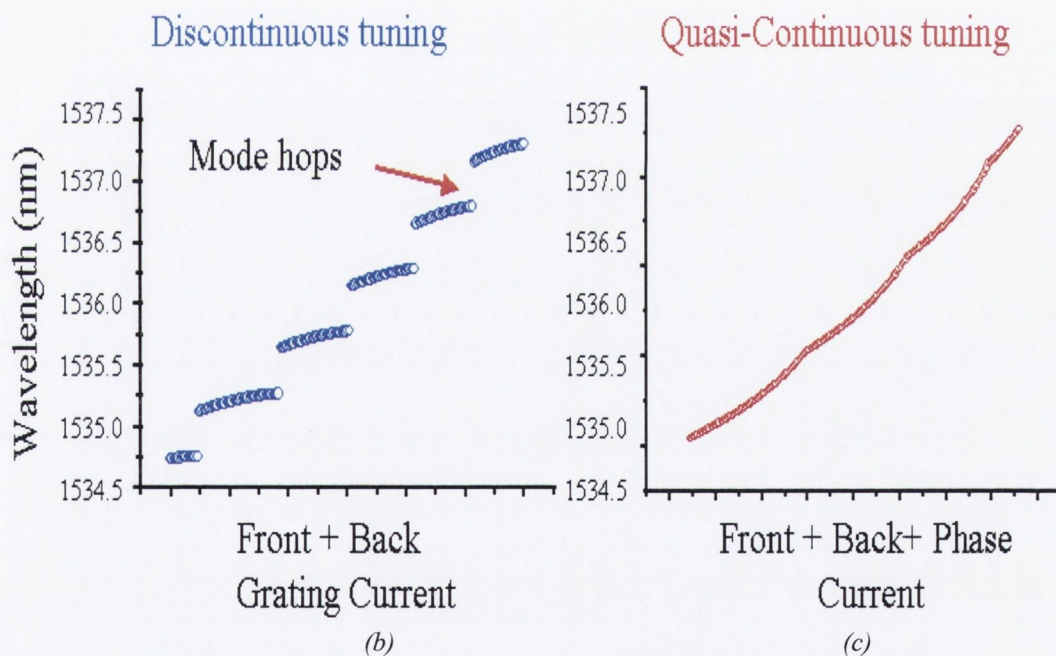


**Figure 3.14** (a) Continuous wavelength tuning as a function of gain section current of a sampled grating DBR currents. (b) Discontinuous wavelength tuning as a function of front and back sampled grating currents, gaps indicate longitudinal mode hops. (c) Emission wavelength as a function of front, back and phase currents resulting in quasi-continuous tuning.



all wavelengths within the tuning range therefore if a gas absorption line lies in the region where a mode hop occurs it cannot be detected.

### **Quasi-Continuous tuning**

Quasi-continuous tuning is achieved by joining overlapping continuous regions in order to get full wavelength coverage over a wider range. This is achieved by tuning a cavity mode and the loss minimum synchronous over a range equal to the longitudinal mode spacing, then resetting the cavity modes to their original settings and subsequently tuning the next cavity mode simultaneously with the loss minimum. In this quasi-continuous tuning range, ranges up to about 40nm have been obtained [28]. In the case of quasi-continuous tuning, the control of the tuneable laser diode can be quite complicated, because three parameters have to be adjusted at the same time to tune the wavelength. The principle is demonstrated in Fig. 3.14(c) for the SG-DBR by adjusting the front, back and phase section currents.

### **3.6.2 Spectrum and Side Mode suppression ratio.**

The side mode suppression ratio (SMSR) is a term used to describe the spectral purity of the single mode output of the lasers. It is the ratio of power in the main mode to the power in the side-mode. The SMSR is usually expressed in decibels, for gas sensing applications a SMSR of at least 30dB, preferably, 40dB is required to minimise mode partition noise [29], and to prevent absorption signals from other modes interfering with the desired signal from the spectral feature of interest. The SMSR value for the SG-DBR and MG-Y laser is dependent on the operating point of the laser. The bias conditions determine whether the device output is single or multimode.

### **SMSR Measurements**

The laser spectrum was measured using an optical spectrum analyser (OSA) and the measurement data transferred to a PC via a GPIB interface bus. The spectrum gives an immediate indication of the modal behaviour of the device. The SMSR is extracted by a peak search algorithm [30]. The SMSR is then the ratio in dB between the highest and second highest peak.

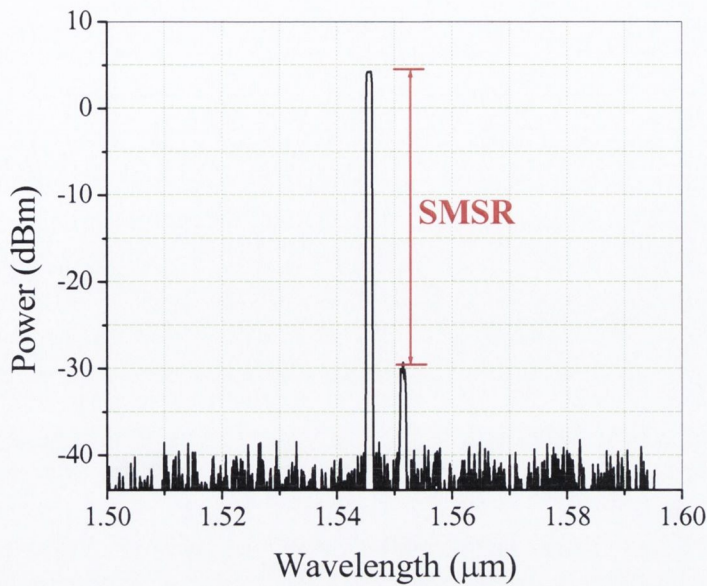
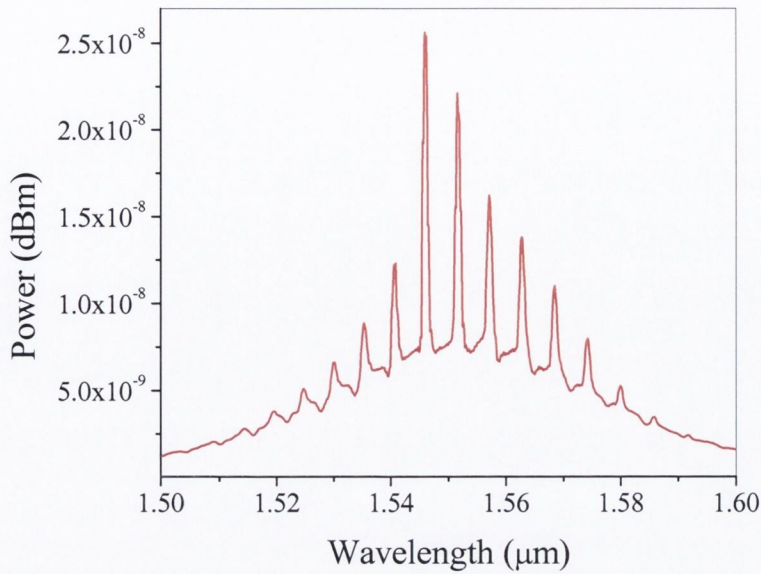


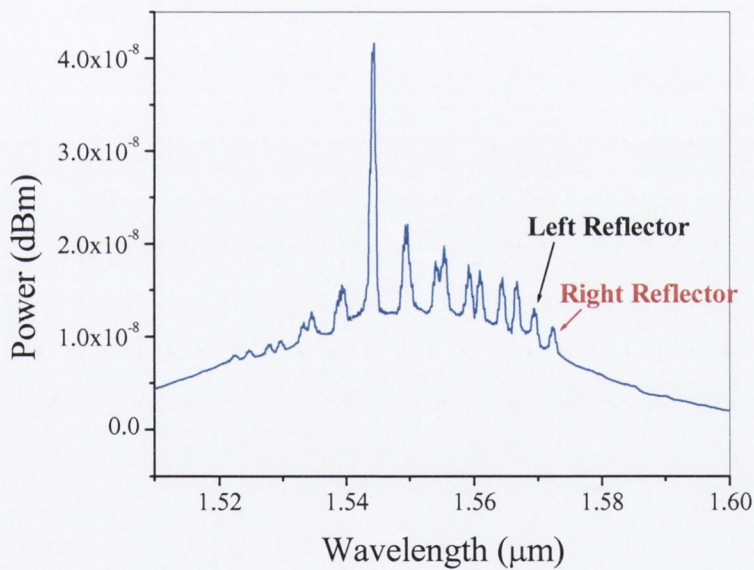
*Figure 3.15 SMSR spectrum of a SG-DBR Laser indicating how SMSR is measured.*

When measured below threshold, the amplified spontaneous emission spectrum (ASE) is useful in confirming the grating design used in tuneable devices. The ASE spectrum of the SG-DBR is shown in Fig. 3.16(a), the reflection comb of the back grating has a prominent effect on the ASE spectrum leaving the peaks of the back reflection comb as features. The opposite is true for the front reflection comb as the light is coupled out of this facet. At the reflection peaks, light is coupled back into the device rather than into the fibre. Therefore the front reflection peaks are seen as sharp dips in the spectrum. For comparison the ASE spectrum of the MG-Y laser is shown in Fig. 3.16(b), as the gratings are on the same side the left and right reflector have prominent effects on the ASE spectrum.





(a)



(b)

**Figure 3.16** (a) ASE spectrum for a SG-DBR Laser just below threshold (b) ASE spectrum for MG-Y Laser.

### 3.6.3 High FM/AM ratio

Modulating the laser drive current not only modulates the laser frequency but also the intensity and this effect is known as R.A.M. This RAM appears as a large offset in the  $I/f$  harmonic absorption spectrum. Due to the decoupling of the power and wavelength control in widely tuneable laser, the objective is to minimise the intensity modulation by modulating the grating sections. Therefore a high FM/AM ratio can be achieved.



### 3.6.4 Spectral Linewidth

In any spectroscopic based gas detection application a knowledge of the system resolution is important. For tuneable laser diode absorption spectroscopy, in particular, it is desirable that the laser emission linewidth remains a factor of ten less than the gas absorption linewidth for all operating conditions of the laser. Typical gases of interest for laser absorption spectroscopy in the  $1.5\mu\text{m}$  wavelength region have Doppler broadened linewidths of around 400MHz at room temperature. Since the laser output has a non-zero linewidth, a broadening of the measured absorption line will inevitably be present, especially in the low-pressure regime. The spectral width of the laser line arises due to fluctuations in the phase of the optical field [31, 32]. Fluctuations arise from two basic sources, a) spontaneous emission which alters the phase and intensity of the lasing field and b) carrier density fluctuations (unique to semiconductors).

In the active section the carrier density is clamped at threshold therefore carrier density fluctuations are suppressed but have more prominent effects on passive sections [22]. In multiple passive section lasers that use the quasi-continuous tuning schemes, the linewidth can vary strongly. The linewidth is relatively low as long as the lasing mode and the loss minimum are more or less aligned, but singularities in the linewidth arise at the mode boundaries, where frequency jumps occur. However when carrier-induced tuning is used, considerable linewidth broadening is observed [22, 33]. This excess broadening is attributed to injection-recombination shot noise in the tuning sections. The shot noise of the carrier injection and recombination processes causes carrier density fluctuations, which lead to refractive index and loss variations. These in turn produce fluctuations of the instantaneous laser frequency that finally lead to a broadened spectral linewidth.

#### Linewidth Measurements

In this section two methods for linewidth characterisation are discussed and some results presented. Linewidth is often defined in terms of the full-width half-maximum (FWHM) of the optical field power spectrum. Grating-based optical spectrum analysers (OSAs) do not offer the measurement resolution required for laser linewidth measurement, so alternative characterisation methods must be used. The alternative methods used in the course of this work include the delayed self-homodyne method and the optical heterodyne. Theory of the heterodyne / delayed self-homodyne



techniques have been reported elsewhere [30, 34] and will be briefly described here. The principle relies on the interference between two optical fields. In both cases the interference between waves causes intensity variations that are detectable using a photodiode.

### Delayed Self-Homodyne

Theoretically it can be proven that the linewidth has a Lorentzian distribution when written as a function of the optical frequency. The delayed self-homodyne technique shown in Fig 3.17, offers a very simple means to measure the linewidth of the laser.

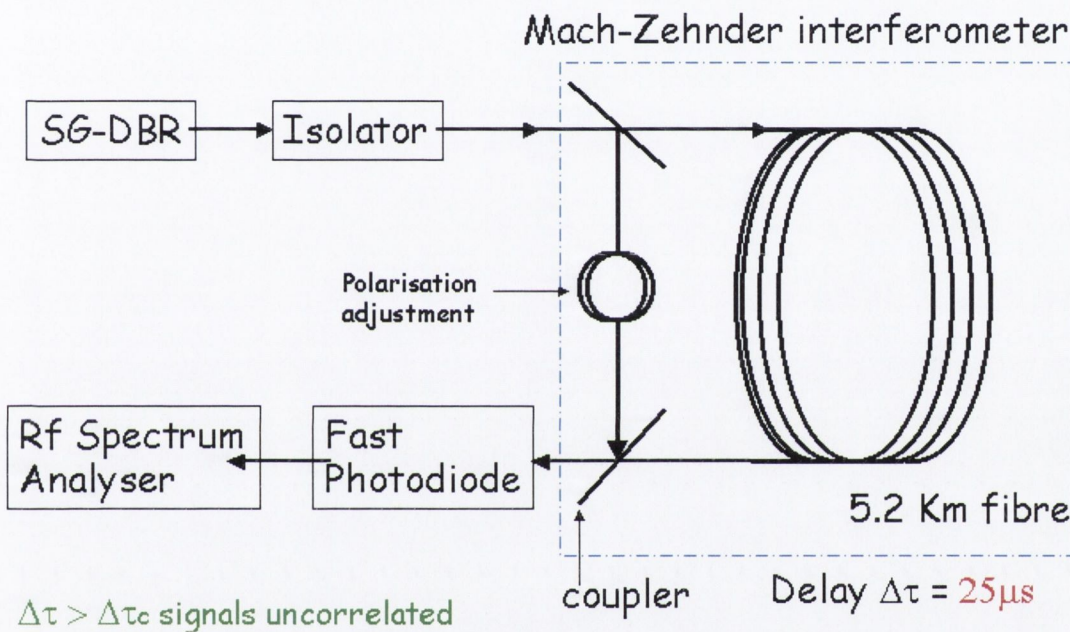


**Figure 3.17** Delayed long-arm self-homodyne experimental set-up.

Incident light is split into two paths by the interferometer, one part goes through a delay line, the other part is sent through a polarisation state controller to maximise the interference between the two mixing signals by ensuring that their polarisation states are closely matched. If the delay  $\tau_0$  of one path exceeds the coherence time  $\tau_c$  of the source, the two combining beams interfere as if they originated from two independent lasers. This process is equivalent to mixing two separate laser signals both having the same linewidth and centre frequency. The mixing of these two signals is accomplished as a result of the square-law nature of the photodiode with respect to the electric field. The displayed spectrum is the autocorrelation function of the laser



lineshape; its spectral linewidth is twice that of the laser linewidth. Some examples from the initial set of measurements are shown in Fig 3.18.

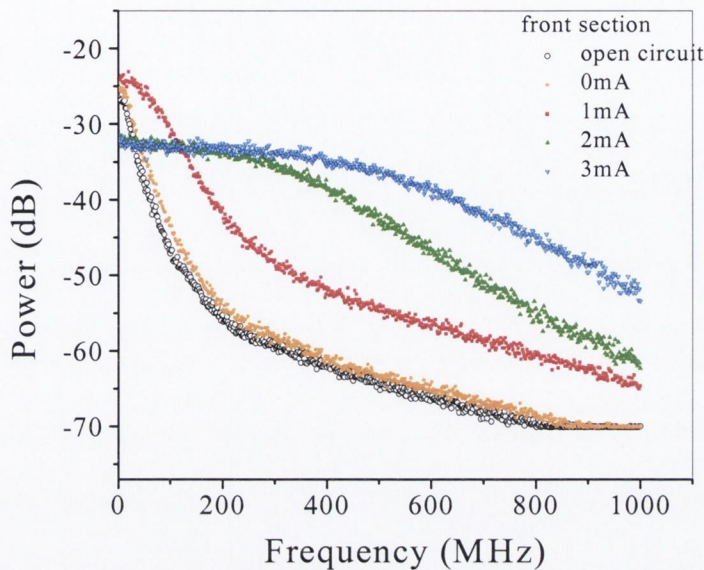


**Figure 3.18** Long-arm self-homodyne lineshapes for a SG-DBR Laser as a function of front reflector current, Gain section current 150mA, phase section, right section current=0mA at 25°C.

The results shown in Fig. 3.18 clearly show the lineshape broadening that occurs with the addition of any amount of front section current into the SG-DBR laser. Since the delayed self-homodyne method centres the mixing spectrum at 0Hz, only half of the symmetrical spectrum is viewed, thus the laser FWHM linewidth corresponds to the measured  $-3\text{dB}$  point. None of the measurements extend down to the 0Hz point, this was due to the type of RF analyser used. While the spectrum close to 0Hz contains useful information for a curve fitting procedure, it is not absolutely necessary. In fact, in such long arm systems, the lineshape tends to become Gaussian at lower frequencies due to the presence of  $1/f$  frequency noise [35]. The resulting lineshape is a mixture of Gaussian and Lorentzian waveforms. To curve-fit to this type of lineshape, a portion of the data must be selected which is purely Lorentzian. As shown in Fig. 3.18, it proved difficult to select an operating point for the laser once current was injected into the passive sections, that yielded a Lorentzian lineshape and therefore produce a confident value of the linewidth. At first it was assumed that the  $1/f$  noise cloaked the true lineshape and therefore it was a problem with the measurement system.



A short-arm homodyne technique was next implemented to counteract the inconsistency in the measurements and reduce the  $1/f$  noise [36]. The 5.2 km fibre was replaced with 39.8 m length of fibre. This technique works on the principle that a short fibre delay introduces a mixture interface and homodyne effects. By curve fitting the resulting spectrum the linewidth may be extracted. As this fitting no longer depends on a pure Lorentzian lineshape, it should be possible to overcome the broadening effects of  $1/f$  noise on the system. The spectrum was fitted to the following expression [37],

$$P(f) = \frac{c\Delta f}{f^2 + \Delta f^2} \left\{ 1 - e^{-4\Delta f} - 2e^{-2\Delta f} \left( \frac{\Delta f}{f} \sin(2\pi f\tau) \right) \right\} \quad (3.32)$$

where  $\tau$  is the delay time calculated using an optical time domain reflectometer at 199.5ns. Fig. 3.19 shows an example of the lineshape obtained using this short-arm method.

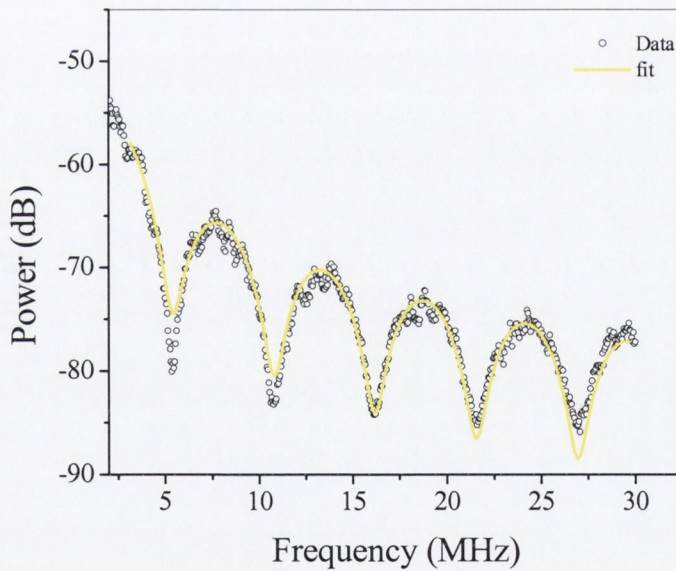


**Figure 3.19** Fitted and measured short-arm self-homodyne curves for a SG-DBR with a gain current of 120mA.

The profiles shown have a Lorentzian shape with the interface pattern superimposed. The sharp troughs where interference was a maximum caused a lot of difficulty during the fitting procedure.

The lack of consistent results prompted further investigations into the linewidth broadening. The conclusions reached by large number of researchers working

together on this problem were taken as a starting point [38]. The current source noise was identified as the main cause of this excess broadening [39]. The ILX-3220B current sources with a noise level of  $8\mu\text{A}$  were subsequently replaced with low noise current sources ILX-3220 ( $<2\mu\text{A}$ ) with significant effect. The cables connecting the current sources to the laser were fitted with ferrite beads to minimise antenna effects in the cables. Fig 3.20 shows examples of the lineshapes obtained using the long-arm homodyne method. This method was preferred to the short-arm technique, due to the ease of fitting the lineshapes. The expected Lorentzian profile is now very obvious and there is minimum broadening caused by current source noise.

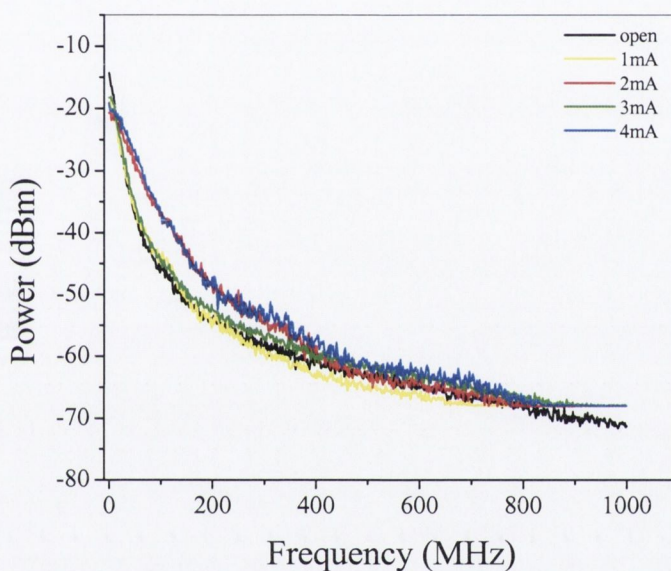


**Figure 3.20** Long-arm self-homodyne lineshapes using low noise current sources on the left reflector section, Gain section current  $150\text{mA}$ , phase section, right section current  $=0\text{mA}$  at  $25^\circ\text{C}$ .

The lineshape, which is measured in dBm, was then curve-fitted to a log-scale Lorentzian function given by

$$P(f) = 10 \log_{10} \left( \frac{\Delta f}{f^2 + \Delta f^2} \right) \quad (3.33)$$

where  $\Delta f$  is the 3dB FWHM linewidth. As mentioned earlier,  $1/f$  noise in the long-arm measurement set-up and the type of radio frequency analyser used meant part of the spectrum suitable for curve fitting was generally from 200MHz onwards.



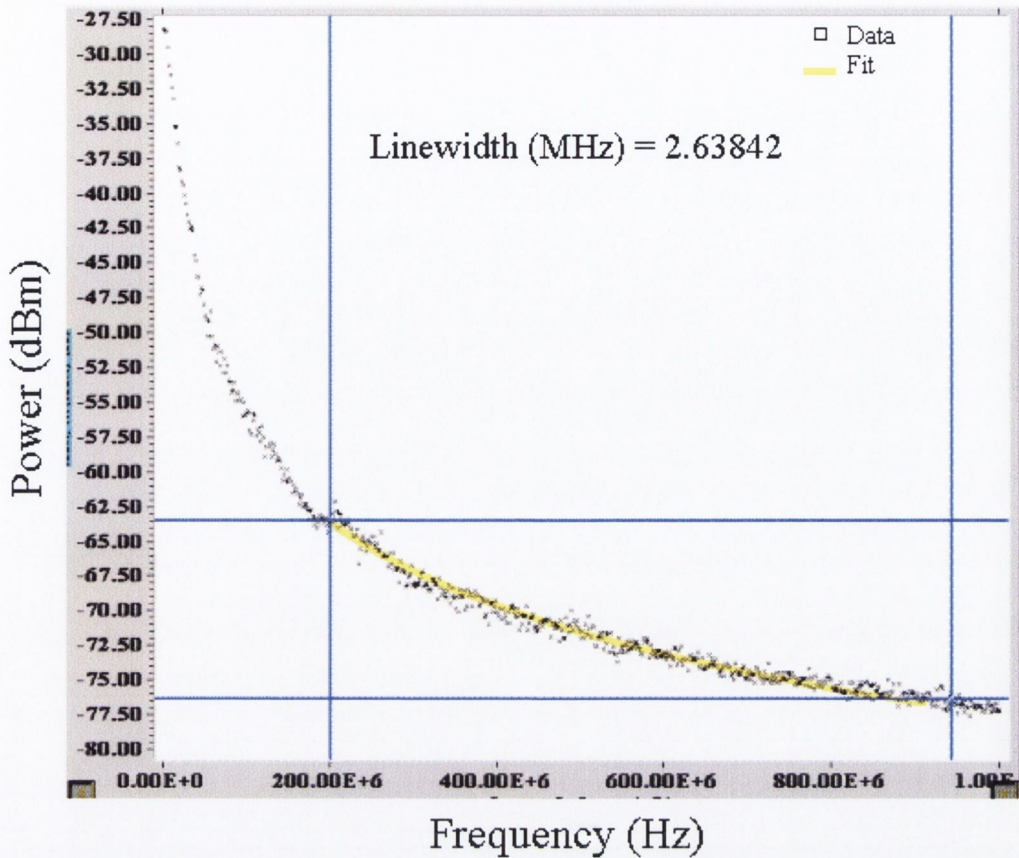


*Figure 3.21 Example of a curve fit to a Lorentzian lineshape for a SG-DBR  $I_{GAIN}=150Ma$ . All other sections are unbiased.*

An example of the measured and fitted curve is shown in Fig 3.21 with the extracted value for the linewidth at 2.638MHz.

### **Optical heterodyne**

To verify the results obtained with the long-arm homodyne technique a second independent approach for linewidth measurements, using the optical heterodyne technique was employed and a comparison with some of the results made. A Heterodyne technique configuration is shown in Fig 3.22, the key requirement for these measurements is a stable, narrow linewidth reference laser (100kHz). In this set-up, both lasers are mixed into a fibered coupler, its first output is connected to an optical spectrum analyser, which allows us to match approximately the two wavelengths. The reference laser (LO) is tuned to a frequency just lower than the average frequency of the laser under study. This creates a heterodyne beat tone between the LO and each of the frequency components in the signal spectrum as

illustrated in Fig. 3.23. The LO laser frequency had to be tuned to within 1GHz of the signal laser frequency to allow the mixing product to fall within the bandwidth of the detector.

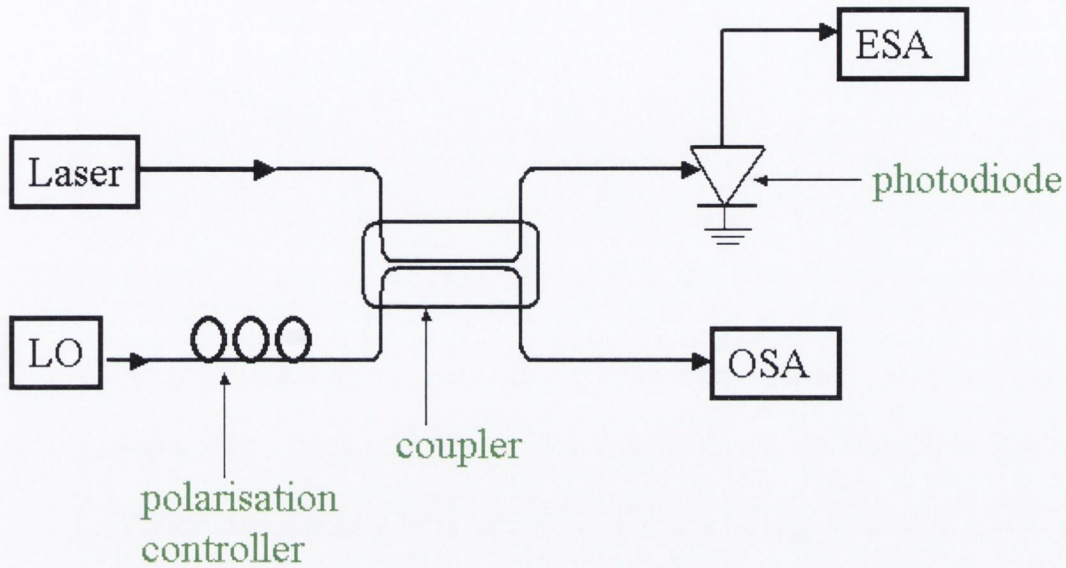


**Figure 3.22** Schematic of the high resolution heterodyne experimental set-up for measuring laser linewidth using an external cavity laser for a local oscillator.

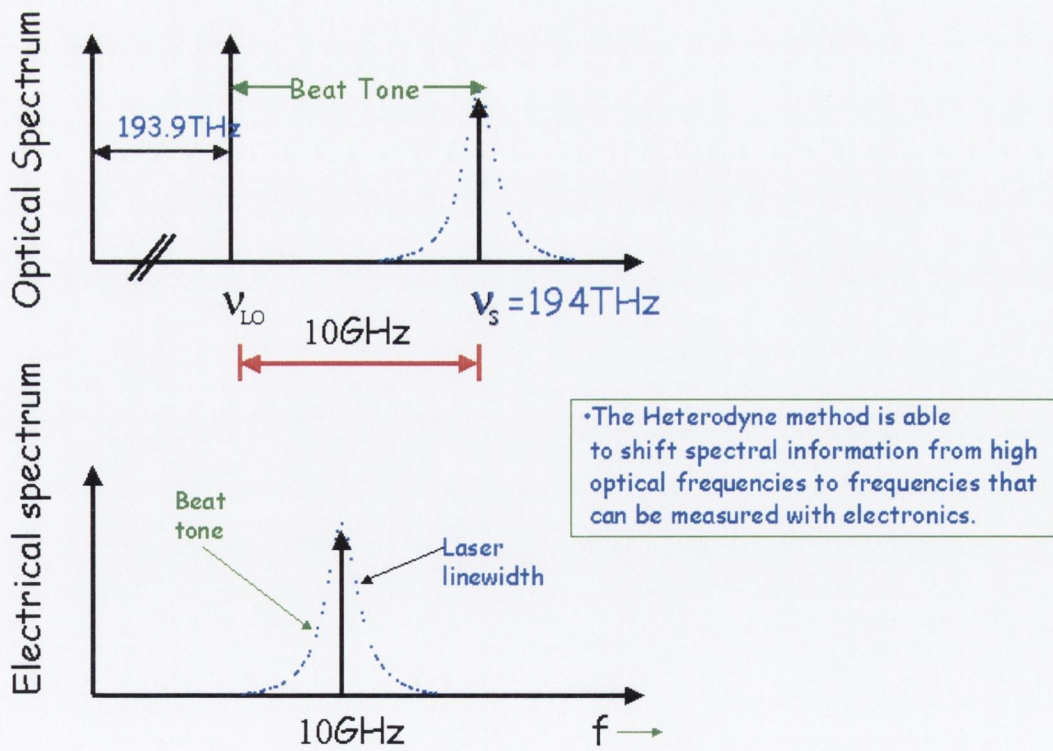


**Figure 3.23** Schematic of the heterodyne mixing of the laser field with a narrow linewidth external cavity laser diode [30].



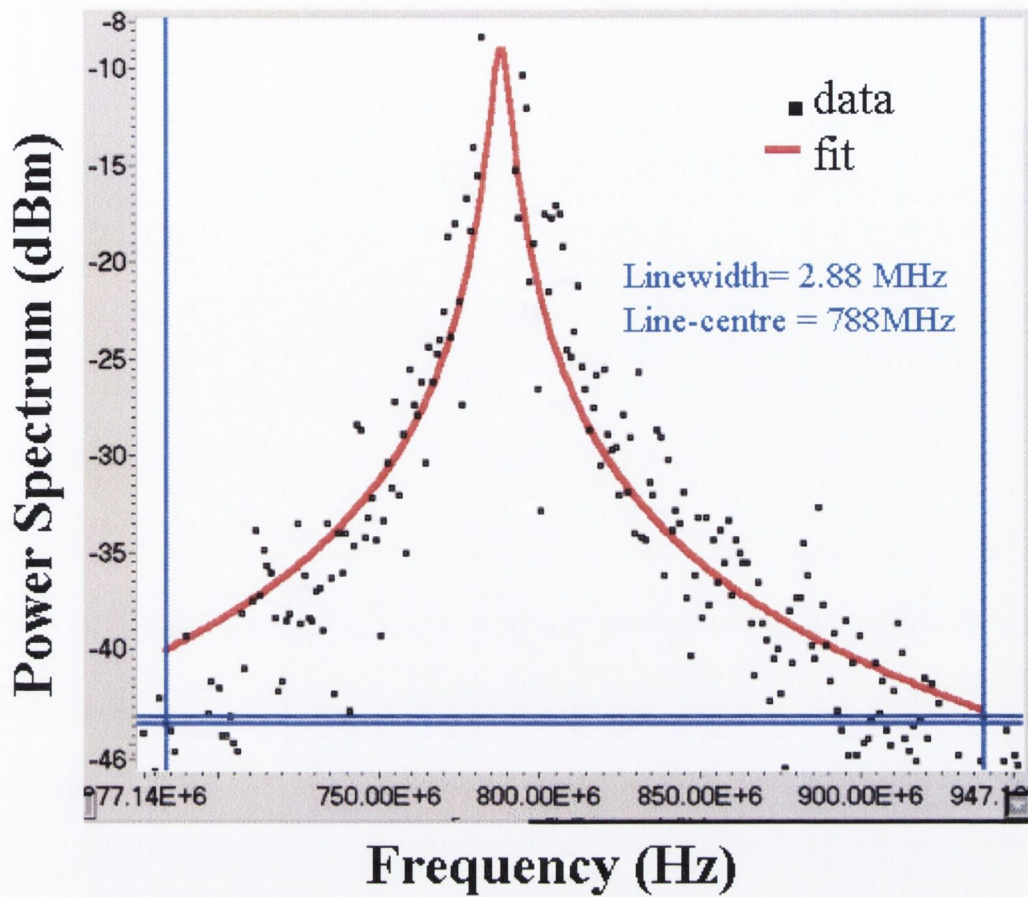


**Figure 3.24** Optical heterodyne power spectrums of a SG-DBR  $I_{GAIN}=150mA$  all other sections are unbiased. Also shown is the fitted Lorentzian lineshape used to extract the linewidth.

The resulting optical heterodyne power spectrum is illustrated in Fig 3.24. The lineshape was fitted with a Lorentzian profile and a linewidth of 2.88MHz was measured. This linewidth compares favourably with the linewidth of 2.63MHz measured with the long-arm self-homodyne technique.

### 3.7 Conclusions

This chapter outlined the current state-of-the-art of monolithically integrated tuneable laser for gas sensing applications. The basic concepts of tuneable lasers were described and the methods used to achieve single frequency output outlined. The distributed feedback and distributed Bragg reflector lasers were then introduced followed by more advanced laser structures for achieving a wide tuning range. Two such lasers were discussed, the sampled grating distributed Bragg reflector and the modulated grating Y-branch laser. A summary of the important standard

characterisation techniques that may be applied to semiconductor lasers was next outlined and some initial results presented. These measurements range from measurements of the output power and wavelength as functions of input current and temperature, which indicate the quality of the devices and hence the suitability of these devices in gas sensing applications.



### 3.8 References

- [1] M. C. Amann. and. J. Buus, *Tunable Laser Diodes*. Norwood: Artech house, 1998.
- [2] G. Sarlet, G. Morthier, and R. Baets, "Control of widely tunable SSG-DBR lasers for dense wavelength division multiplexing," *Lightwave Technology, Journal of*, vol. 18, pp. 1128-1138, 2000.
- [3] A. P. Larson, L. Sandstrom, S. Hojer, H. Ahlberg, and B. Broberg, "Evaluation of distributed Bragg reflector lasers for high-sensitivity near-infrared gas analysis," *Optical Engineering*, vol. 36, pp. 117-123, 1997.
- [4] H. Kogelnik and C. V. Shank, "Coupled-Wave Theory of Distributed Feedback Lasers," *Journal of Applied Physics*, vol. 43, pp. 2327-2335, 1972.
- [5] J. Buus, *Single-Frequency Semiconductor Lasers*: SPIE, 1990.
- [6] E. Kapon, A. Hardy, and A. Katzir, "The effect of complex coupling coefficients on distributed feedback lasers," *Quantum Electronics, IEEE Journal of*, vol. 18, pp. 66-71, 1982.
- [7] A. J. Lowery and D. Novak, "Performance comparison of gain-coupled and index-coupled DFB semiconductor lasers," *Quantum Electronics, IEEE Journal of*, vol. 30, pp. 2051-2063, 1994.
- [8] K. Utaka, S. Akiba, K. Sakai, and Y. Matsushima,  $\lambda/4$ -shifted InGaAsP/InP DFB lasers," *Quantum Electronics, IEEE Journal of*, vol. 22, pp. 1042-1051, 1986.

- [9] B. R. Bennett, R. A. Soref, and J. A. Del Alamo, "Carrier-induced change in refractive index of InP, GaAs and InGaAsP," *Quantum Electronics, IEEE Journal of*, vol. 26, pp. 113-122, 1990.
- [10] J.-P. Weber, "Optimization of the carrier-induced effective index change in InGaAsP waveguides-application to tunable Bragg filters," *Quantum Electronics, IEEE Journal of*, vol. 30, pp. 1801-1816, 1994.
- [11] L. A. Coldren, "Monolithic tunable diode lasers," *Selected Topics in Quantum Electronics, IEEE Journal of*, vol. 6, pp. 988-999, 2000.
- [12] V. Jayaraman, Z.-M. Chuang, and L. A. Coldren, "Theory, design, and performance of extended tuning range semiconductor lasers with sampled gratings," *Quantum Electronics, IEEE Journal of*, vol. 29, pp. 1824-1834, 1993.
- [13] Y. Tohmori, Y. Yoshikuni, H. Ishii, F. Kano, T. Tamamura, Y. Kondo, and M. Yamamoto, "Broad-range wavelength-tunable superstructure grating (SSG) DBR lasers," *Quantum Electronics, IEEE Journal of*, vol. 29, pp. 1817-1823, 1993.
- [14] J.-O. Wesstrom, J. Bergerengen, G. Sarlet, Y. Gustafsson, P. Szabo, and B. Broberg, "GCSRs and other widely tunable lasers," presented at Advanced Semiconductor Lasers and Applications/Ultraviolet and Blue Lasers and Their Applications/Ultralong Haul DWDM Transmission and Networking/WDM Components, 2001 Digest of the LEOS Summer Topical Meetings, 2001.
- [15] J.-O. Wesstrom, S. Hammerfeldt, J. Buus, R. Siljan, R. Laroy, and H. de Vries, "Design of a widely tunable modulated grating Y-branch laser using the additive Vernier effect for improved super-mode selection," presented at Semiconductor Laser Conference, 2002. IEEE 18<sup>th</sup> International, 2002.



- [16] P.-J. Rigole, S. Nilsson, L. Backbom, T. Klinga, J. Wallin, B. Stalnacke, E. Berglind, and B. Stoltz, "114-nm wavelength tuning range of a vertical grating assisted codirectional coupler laser with a super structure grating distributed Bragg reflector," *Photonics Technology Letters, IEEE*, vol. 7, pp. 697-699, 1995.
- [17] A. J. Ward, D. J. Robbins, G. Busico, N. D. Whitbread, P. J. Williams, D. C. J. Reid, and J. R. Rawsthorne, "Modelling of phase-grating based wideband tuneable lasers with simplified quasi-digital wavelength selection," *Optoelectronics, IEE Proceedings-*, vol. 150, pp. 199-204, 2003.
- [18] G. Morthier, B. Moeyersoon, and R. Baets, "A sampled or superstructure grating tunable twin-guide laser for wide tunability with 2 tuning currents," presented at Optical Fiber Communication Conference and Exhibit, 2001. OFC 2001, 2001.
- [19] C. J. Chang-Hasnain, "Tunable VCSEL," *Selected Topics in Quantum Electronics, IEEE Journal of*, vol. 6, pp. 978-987, 2000.
- [20] C. J. Chang-Hasnain, "Widely tunable VCSEL using MEMS technology," presented at Lasers and Electro-Optics Society 2000 Annual Meeting. LEOS 2000. 13th Annual Meeting. IEEE, 2000.
- [21] F. Riemenschneider, M. Maute, H. Halbritter, G. Boehm, M.-C. Amann, and P. Meissner, "Continuously Tunable Long-Wavelength MEMS-VCSEL With Over 40-nm Tuning Range," *Photonics Technology Letters, IEEE*, vol. 16, pp. 2212-2214, 2004.
- [22] P. Signoret, M. Myara, J.-P. Turrenc, B. Orsal, M.-H. Monier, J. Jacquet, P. Leboudec, and F. Marin, "Bragg section effects on linewidth and lineshape in

- 1.55 $\mu\text{m}$  DBR tunable laser diodes," *Photonics Technology Letters, IEEE*, vol. 16, pp. 1429-1431, 2004.
- [23] A. Syrbu, V. Iakovlev, G. Suruceanu, A. Caliman, A. Rudra, A. Mircea, A. Mereuta, S. Tadeoni, C.-A. Berseth, M. Achtenhagen, J. Boucart, and E. Kapon, "1.55  $\mu\text{m}$  optically pumped wafer-fused tunable VCSELs with 32-nm tuning range," *Photonics Technology Letters, IEEE*, vol. 16, pp. 1991-1993, 2004.
- [24] B. Mason, J. Barton, G. A. Fish, L. A. Coldren, and S. P. DenBaars, "Design of sampled grating DBR lasers with integrated semiconductor optical amplifiers," *Photonics Technology Letters, IEEE*, vol. 12, pp. 762-764, 2000.
- [25] Y. Tohmori, Y. Yoshikuni, T. Tamamura, H. Ishii, Y. Kondo, and M. Yamamoto, "Broad-range wavelength tuning in DBR lasers with superstructure grating (SSG)," *Photonics Technology Letters, IEEE*, vol. 5, pp. 126-129, 1993.
- [26] G. S. J.-O. Wesström, S. Hammerfeldt, L. Lundqvist, P. Szabo, P.-J. Rigole, "State-of-the-art performance of widely tunable modulated grating Y-branch lasers," *Proc. OFC 2004, paper TuE2*, 2004.
- [27] Y. Tohmori, Y. Yoshikuni, H. Ishii, F. Kano, T. Tamamura, and Y. Kondo, "Over 100 nm wavelength tuning in superstructure grating (SSG) DBR lasers," *Electronics Letters*, vol. 29, pp. 352-354, 1993.
- [28] P.-J. Rigole, S. Nilsson, L. Backbom, B. Stalnacke, E. Berglind, J.-P. Weber, and B. Stoltz, "Quasi-continuous tuning range from 1560 to 1520 nm in a GCSR laser, with high power and low tuning currents," *Electronics Letters*, vol. 32, pp. 2352-2354, 1996.



- [29] P. Werle, "A review of recent advances in semiconductor laser based gas monitors," *Spectrochimica Acta Part a-Molecular and Biomolecular Spectroscopy*, vol. 54, pp. 197-236, 1998.
- [30] D. Derickson, *Fiber Optic Test and Measurement*: Prentice Hall PTR, 1998.
- [31] C. Henry, "Theory of the linewidth of semiconductor lasers," *Quantum Electronics, IEEE Journal of*, vol. 18, pp. 259-264, 1982.
- [32] C. Henry, "Theory of the phase noise and power spectrum of a single mode injection laser," *Quantum Electronics, IEEE Journal of*, vol. 19, pp. 1391-1397, 1983.
- [33] M.-C. Amann and R. Schimpe, "Excess linewidth broadening in wavelength-tunable laser diodes," *Electronics Letters*, vol. 26, pp. 279-280, 1990.
- [34] D. M. Baney and P. B. Gallion, "Power spectrum measurement of a modulated semiconductor laser using an interferometric self-homodyne technique: influence of quantum phase noise and field correlation," *Quantum Electronics, IEEE Journal of*, vol. 25, pp. 2106-2112, 1989.
- [35] L. B. Mercer,  $1/f$  frequency noise effects on self-heterodyne linewidth measurements," *Lightwave Technology, Journal of*, vol. 9, pp. 485-493, 1991.
- [36] L. Richter, H. Mandelberg, M. Kruger, and P. McGrath, "Linewidth determination from self-heterodyne measurements with subcoherence delay times," *Quantum Electronics, IEEE Journal of*, vol. 22, pp. 2070-2074, 1986.
- [37] G. Genty, M. Kaivola, and H. Ludvigsen, "Measurements of linewidth variations within external-cavity modes of a grating-cavity laser," *Optics Communications*, vol. 203, pp. 295-300, 2002.

- [38] M. O. van Deventer, P. Spano, and S. K. Nielsen, "Comparison of DFB laser linewidth measurement techniques results from COST 215 round robin," *Electronics Letters*, vol. 26, pp. 2018-2020, 1990.
- [39] G. H. Duan and P. Gallion, "Drive current noise induced linewidth in tunable multielectrode lasers," *Photonics Technology Letters, IEEE*, vol. 3, pp. 302-304, 1991.



# Chapter 4

## Absorption Line Shift with Temperature and Pressure. Impact on Laser-Diode-Based H<sub>2</sub>O Sensing at 1.393 $\mu$ m

### 4.1. Introduction

Gas sensing using laser diode based optical spectroscopy is becoming the standard for real time non-invasive measurements of industrial gas emissions and the monitoring of gases used in manufacturing processes. In typical atmospheric open path trace gas measurements, there is little deviation in pressure and temperature from standard values ( $\approx 1000\text{mbar}$ ,  $293\text{K}$ ) and so accurate concentration measurements are relatively easily achieved by correcting for minor effects such as collisional line broadening. However, in various industrial contexts (e.g. gas emanating from a stack) large variations in operating conditions may result in, for example, a gas temperature in the range  $300\text{K}$ – $1100\text{K}$ , its value dependent on the industrial process. Hence, the use of a reference cell to lock the emission wavelength of the laser diode to a target absorption line may be impaired by a modification of spectral characteristics of the sample gas as a function of temperature and pressure. Therefore, a knowledge of absorption line characteristics as a function of temperature and pressure is necessary for the application of a spectroscopic based sensor in such industrial environments.

The effects of temperature and pressure on the spectral position of the water vapour rotational absorption line at  $1.3928\mu\text{m}$ , which has a linestrength of  $2.52 \times 10^{-22}$   $\text{cm.molecule}^{-1}$  is investigated. Absorption line spectral shifts as a function of pressure and temperature in the range  $0\text{mbar}$  -  $1000\text{mbar}$  and  $293\text{K}$  -  $1100\text{K}$  respectively were investigated and are reported in this chapter. The linestrength dependence as a function of temperature was also measured. These are critical characteristics for laser diode based gas sensing where the temperature and pressure of the sample gas may differ significantly from that of the gas in a reference cell which is used to implement line locking.



## 4.2 Experimental

### 4.2.1 Gas Cell

The high temperature absorption gas cell, shown in Fig. 4.1, was designed and fabricated for the purpose of absorption line shift measurements at elevated temperature. The cell consists of a 1m long, 25.4mm diameter stainless steel cylinder. Short sections of thin walled (0.5mm) stainless steel tubing were welded to each end of the main cylinder. Quartz windows cut at Brewster's angle were set into the thin walled tubing with adhesive. The thin-walled tubing was used to reduce heat transfer from the main cell to the windows. Water-cooled copper jackets in thermal contact with the thin-walled tubing, were also used to minimise this heat transfer. The main cylinder was surrounded by ceramic heaters and enclosed by efficient high temperature insulation. A K-type thermocouple placed in contact with the cell wall provided feedback to a temperature controller. Starting from room temperature the entire cell could be stabilized at 1100K in approximately two hours. The sample cell was connected to the gas handling system via quarter inch stainless steel tubing welded to the main cylinder. A liquid reservoir containing de-ionised water facilitated the introduction of water vapour into the gas cell. The cell and gas handling system are also shown in Fig. 4.1.

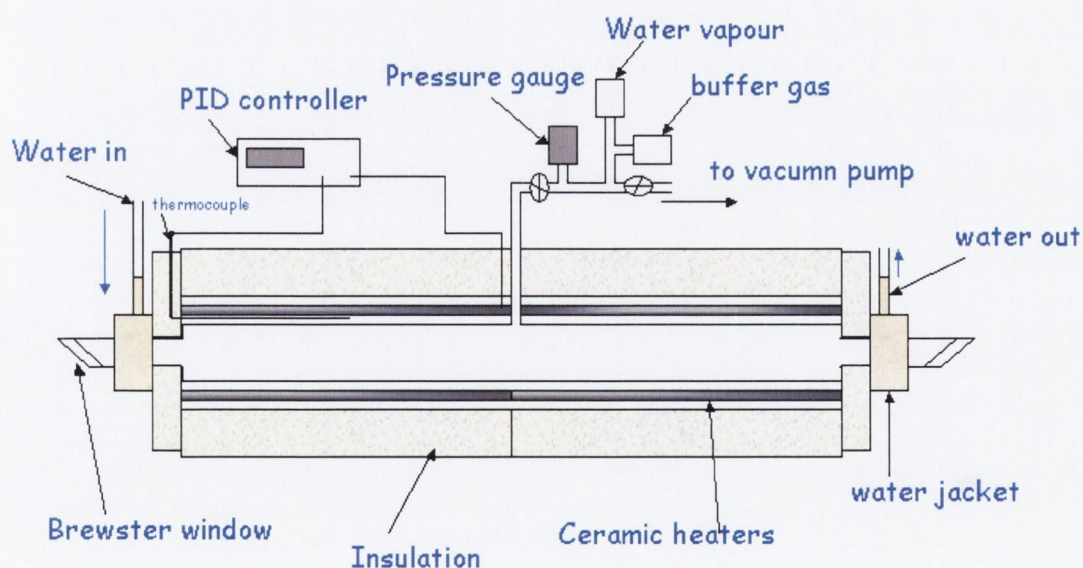


*Figure 4.1. Schematic of high temperature gas absorption cell.*



### 4.2.2 Laser diode

The diode laser used in the experiment is a distributed feedback (DFB) InGaAsP device supplied by Aero-laser, with a room temperature emission wavelength of 1.393 $\mu\text{m}$ . The DFB operated in a single mode in the temperature range  $5^\circ\text{C} < T < 35^\circ\text{C}$  shown in Fig. 4.2. The device had a SMSR  $> 35\text{dB}$  across the temperature tuning range of the device. Calibration of the wavelength tuning with current was achieved by measuring the current dependence of the single mode emission characteristics of the device using a wave meter (0.01nm resolution) and is also shown in Fig. 4.2. The emission wavelength tunes linearly with current at a rate  $\Delta\lambda/\Delta I = 1.35 \times 10^{-2} \text{ nm/mA}$  over the small current range (70 to 74mA) required to tune across the absorption line with a constant laser heat sink temperature of  $22^\circ\text{C}$ . The constant tuning rate with current, all be it over a small range, provides the relative wavelength tuning calibration required to accurately measure the small absorption line shifts. Fig. 4.3 shows the laser diode L-I curve measured at  $22^\circ\text{C}$  with a 20cm path length between the device and the photo-detector. An absorption profile is clearly visible on the L-I curve resulting from spectral absorption by water vapour present in room air. The laser has a threshold current of approximately 25mA at  $22^\circ\text{C}$ . Also shown in Fig 4.3 is the voltage-current plot, which shows an operating voltage of the laser in the range 0.7-1.8V, which is typical and yields a differential resistance of  $6.6\Omega$  which indicates no parasitic resistances in the laser.

In this work, spectral resolution is an important issue since it effectively determines the smallest absorption line shift measurable. Resolution is essentially determined by the minimum laser drive current step of the high precision ILX 3220 current source ( $4 \times 10^{-3} \text{ mA}$  equivalent to  $5.40 \times 10^{-5} \text{ nm}$ ) in convolution with the laser diode emission linewidth. Since a measurement instrument to determine laser linewidth was unavailable at the time, it was decided to estimate it using a spectral absorption technique. High-resolution absorption spectra of the Doppler broadened water vapour line at 1.3928 $\mu\text{m}$  were taken by detecting the transmitted light attenuation through the gas as the laser diode emission wavelength was swept across the absorption feature of interest by varying the current of the laser diode. The absorption linewidth (FWHM) was plotted as a function of pressure in the range 1- 40mbar and is shown in Fig. 4.4. The measured Doppler linewidth at 1mbar is  $3.7 \times 10^{-3} \text{ nm}$ .

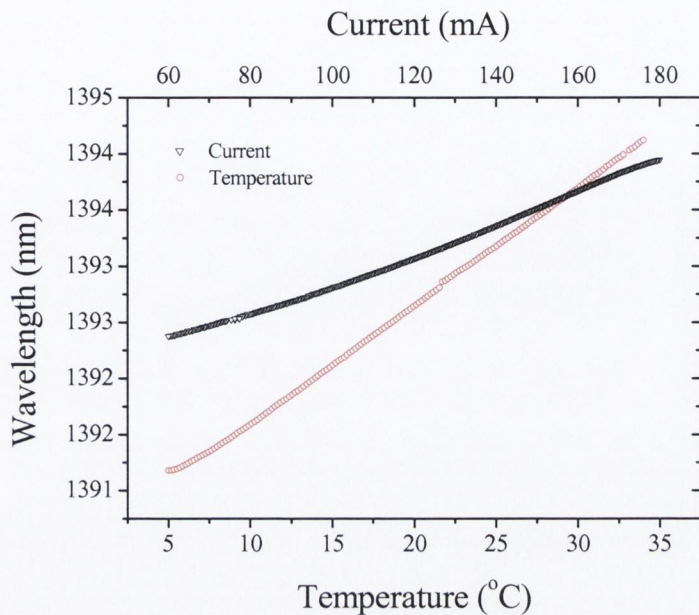


**Figure 4.2.** Measured spectral tuning of 1.39 $\mu\text{m}$  DFB laser diode as a function of temperature at a constant injection current of 120mA and as a function of injection current at a laser heat sink temperature of 22°C.

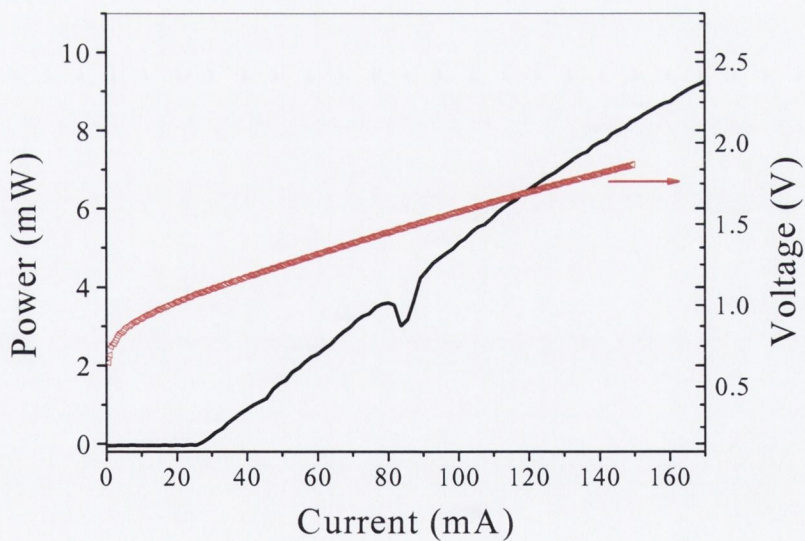


**Figure 4.3.** Laser diode L-I curve at 22°C with H<sub>2</sub>O absorption profile visible. Also shown is the voltage-current plot and shows an operating voltage in the range 0.8-1.7V. The differential resistance is obtained from the first derivative of this of curve.



Calculations show that a laser diode emission profile (assuming a Lorentzian distribution) of width in the range 10MHz-30MHz (FWHM) may be convolved with the Doppler absorption profile of width  $3.7 \times 10^{-3}$  nm without observing significant broadening of the absorption line. Hence, we can infer that the laser linewidth is less than 30MHz, which is significantly smaller than the measured Doppler linewidth. This estimated upper limit of the laser linewidth is consistent with the typical value (10MHz) specified by Aero-laser. As a consequence of these measurements, collisional narrowing was observed as the pressure was increased from 1 to 5mbar (see Fig. 4.4). The linewidth of the water vapour line decreases, as a result of collisional narrowing (Dicke narrowing), [1, 2] whereby with increasing pressure, the Doppler width is reduced by the effect of velocity averaging of elastic collisions. The minimum collisional narrowed absorption linewidth ( $3.12 \times 10^{-3}$  nm) occurred at a pressure of 5mbar. Hence, in subsequent lineshift spectral measurements when water vapour in a reference cell was used as a spectral marker the pressure in the cell was set to 5mbar.

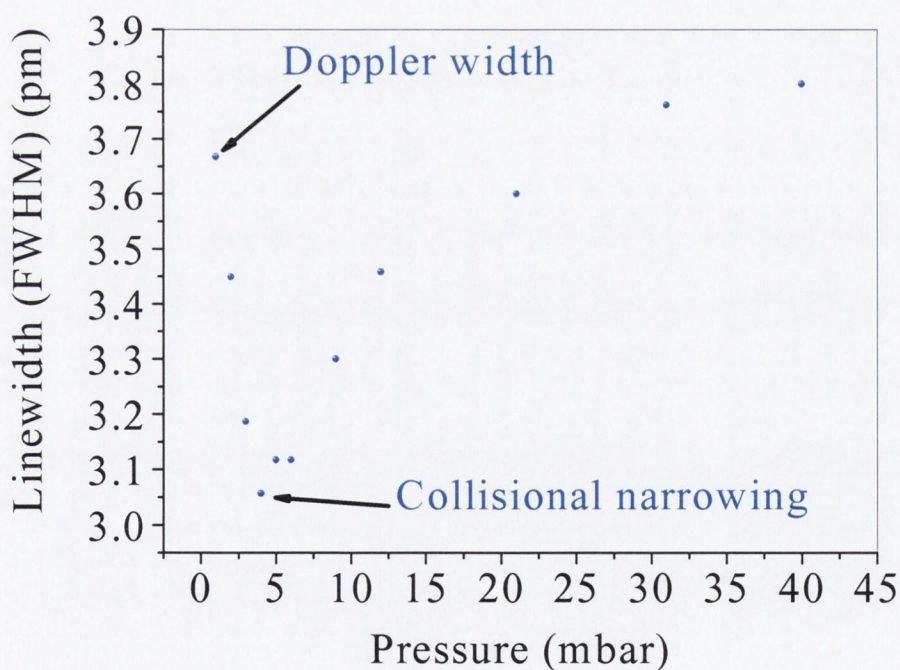


**Figure 4.4.** Collisional narrowing of the absorption feature in the pressure range 1-40mbar.

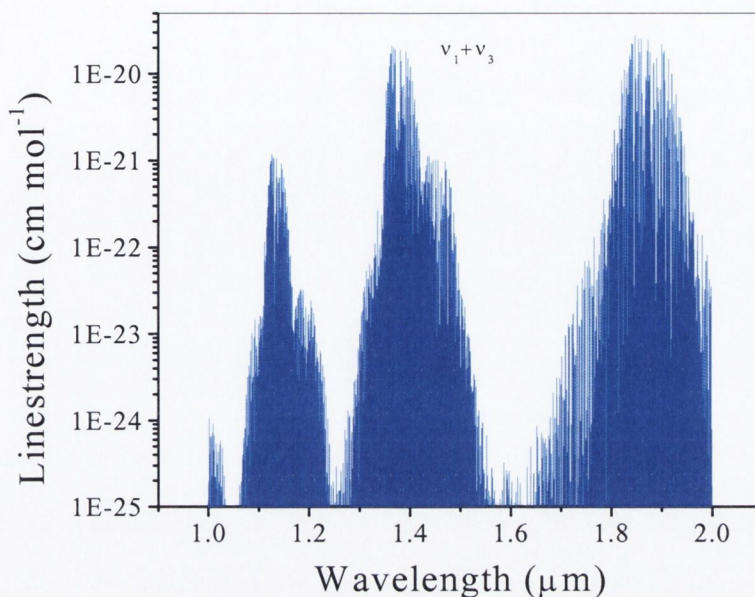


**Figure 4.5.** Near-Infrared water vapour linestrengths [3].

### 4.3 Near-Infrared Spectra of H<sub>2</sub>O

Water is the most important molecule for without it life on earth would not be possible. Water vapour, for example makes the earth habitable through the greenhouse effect. Although highly variable in concentration, the infrared-active water molecule is the third most abundant atmospheric species. In view of the general interest in the spectroscopy of water vapour and the important applications in atmospheric science and astronomy, the measurement of water vapour is also important in many industrial applications, for example, continuous emission monitoring in combustion processes where the vapour concentration can be related to performance parameters such as efficiency of combustion and heat release [4-7]. As illustrated in Fig 4.5, H<sub>2</sub>O has three main absorption bands in the NIR. In this chapter, we investigated the effects of temperature and pressure on the spectral position of the water vapour rotational absorption line at 1.3928μm, which has a linestrength of  $2.52 \times 10^{-22}$  cm.molecule<sup>-1</sup> [3, 8]. This line is in the water vapour vibrational combination band  $\nu_1+\nu_3$  centred at 1.38μm, where  $\nu_1$  denotes the symmetric OH stretch and  $\nu_3$  the asymmetric OH stretch.



## 4.4 Direct-Detection Measurements

The absorption lines in the vibrational combination band ( $\nu_1 + \nu_3$ ) of  $\text{H}_2\text{O}$  are relatively strong ( $\approx 10^{-20}$  cm.molecule $^{-1}$ ). Hence, a direct detection technique was adopted here for line shift measurements. A schematic view of the experimental arrangement is shown in Fig. 4.6. The output from the DFB laser diode is passed through a beam splitter and on through the high temperature gas cell and focused down onto a InGaAs photodiode. The beam splitter placed in front of the high temperature gas cell directs approximately 10% of the laser light, through a reference cell containing approximately 5mbar of water vapour maintained at room temperature. The monitored absorption line in the reference cell was used as a spectral marker against which the spectral characteristics of the gas in the sample cell as a function of temperature and pressure, simultaneously obtained, were compared. A 16-bit A/D card collected the direct absorption signals from the measurement and reference paths photodiodes. Spectral line shift and line broadening measurements were taken using 20mbar of pure water vapour in the gas sample cell, buffered from 20mbar to 1000mbar with  $\text{N}_2$ , at temperatures in the range from 300K to 1100K. Line strength measurements of the targeted water vapour line at a pressure of 20mbar were also taken in the range 300K to 1100K.

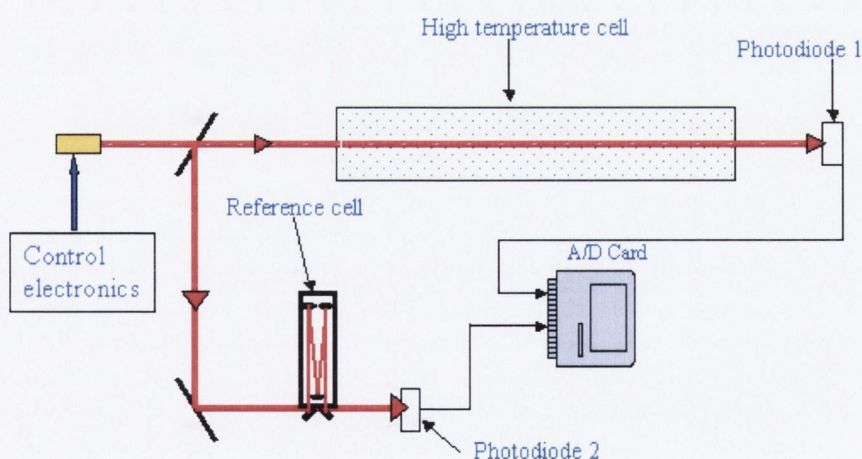


**Figure 4.6.** Schematic of the experimental set-up for measurement of absorption lineshift.

## 4.5 Direct-Detection Results

Absorption measurements of the isolated water vapour line at  $1.3928\mu\text{m}$  were made by detecting the transmitted light attenuation through the gas as the laser diode emission wavelength was swept across the line by varying the laser bias current. A typical direct absorption spectrum of the isolated collisional broadened water vapour line at 1000mbar and a temperature of 300K is shown in Fig. 4.7. A linear sloping baseline resulting from the linear dependence of the output power on laser diode current can be seen. The absorption profile was normalised with respect to laser power and the sloping background removed, by fitting a linear response to the regions of the transmitted laser signal away from the absorption line. The need for an additional reference beam to achieve normalisation can be avoided with this approach.

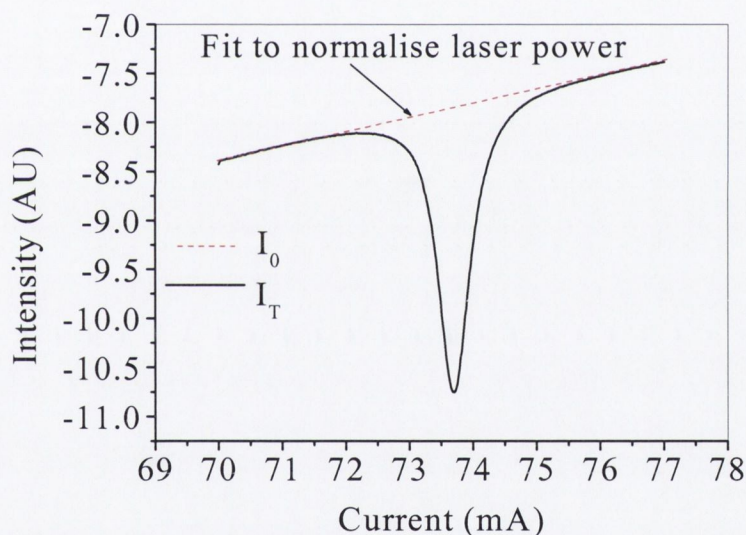


**Figure 4.7.** Measured absorption profile with linear fit of the laser power used for normalisation.

Fig. 4.8 (a) shows a typical water vapour absorption line-shape at a pressure of 5mbar, when the sloping background is removed, overlaid with the best-fit Galatry profile [9]. Fig 4.8(b) shows the same absorption line overlaid with a best-fit Voigt profile [10]. Similarly, a high-pressure (1000mbar) line-shape overlaid with a best-fit Lorentzian profile is shown in Fig. 4.8(c). The residuals (difference between data and fit) are also shown in Fig. 4.8.



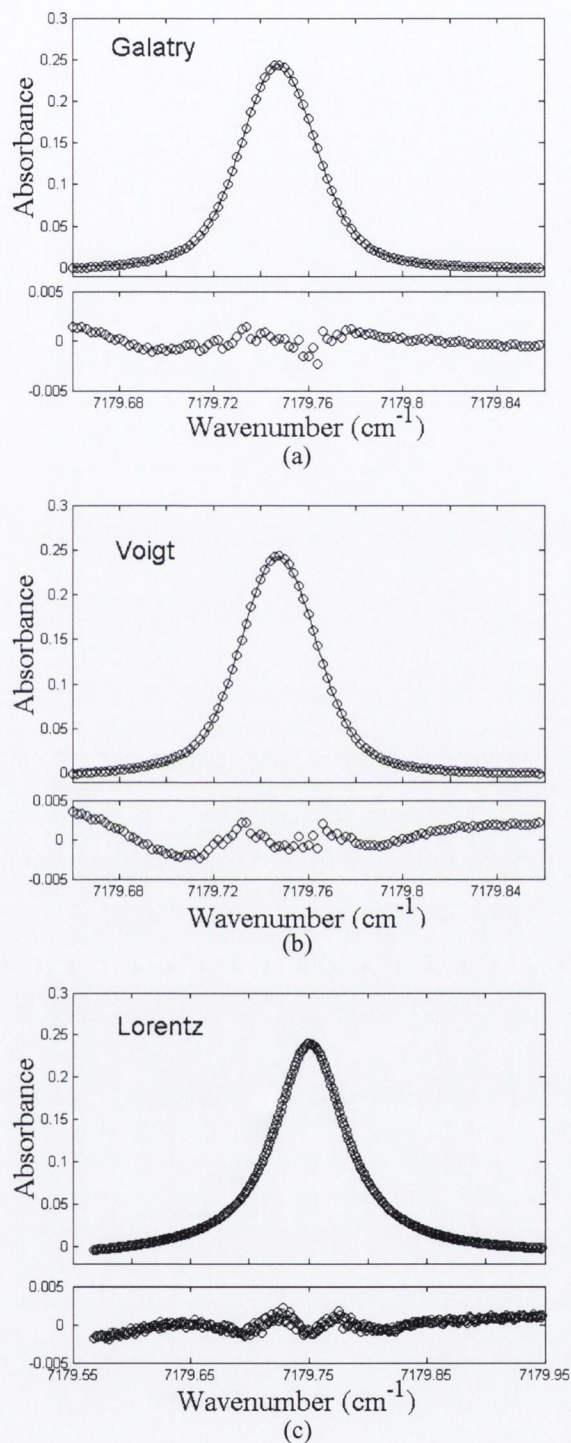


**Figure 4.8.** Absorbance profile at a pressure of (a) 5mbar overlaid with best-fit Galatry profile (b) 5mbar overlaid with best-fit Voigt profile and (c) 1000mbar overlaid with best-fit Lorentzian profile. Residual plots show the differences between data and the fitted spectral profiles.

The residual of the Galatry fit is similar to that of the Voigt. However, it is clear that the error associated with the Galatry fit is notably less, since it takes account of velocity changing collisions, which produce a linewidth narrowing effect observable at low pressures. The measured spectra in the pressure range 20-1000mbar were modelled with Voigt and Lorentzian profiles in the appropriate pressure regime to extract line centre positions and the broadening coefficients. The shift is measured as the difference between the wavelength  $\lambda_P$  of the absorption line centre of the sample gas at a given pressure  $P$  and the wavelength  $\lambda_R$  of the corresponding reference peak. Shift ( $\lambda_P - \lambda_R$ ), is positive for all values of  $P > R$ . The shift coefficient  $\delta$ , was determined from the slope of the linear fit to the measured shifts at various pressures, as shown in Fig. 4.9. The shift coefficient was measured as a function of temperature in the range 300K-1100K and is shown in Fig. 4.10. The maximum measured spectral shift coefficient with pressure is  $2.29 \times 10^{-6}$  nm/mbar (0.35MHz/mbar) and occurs at room temperature. A pressure increase of 100mbar, leads to a shift of 35MHz or approximately 1% of a pressure broadened linewidth. At a constant pressure of 1000mbar, the spectral line shift for an 800K change in temperature is approximately  $1.13 \times 10^{-3}$  nm (173MHz) or approximately 5.8% of a typical collision broadened linewidth. In the case of monitoring the H<sub>2</sub>O concentration, using a direct detection system and a reference cell at constant temperature (296K) for line-locking, the above wavelength shift would result in an inaccuracy of approximately 2%.

It is important to monitor how the transition lineshape varies with pressure. In the collisional broadening region, neighbouring absorption lines in close proximity can overlap. The absorption linewidth was measured as a function of pressure and the results shown in Fig. 4.11. The broadening coefficient  $2\gamma$  was determined from the slope of Fig. 4.11, which is a plot of measured Lorentzian widths in the pressure range  $20 \leq P \leq 1000$ mbar. The measured N<sub>2</sub> broadening coefficient at 296K is  $1.54 \times 10^{-5}$  nm/mbar (2.38MHz/mbar) compared with 2.68MHz/mbar at 300K reported by Delaye et al [11]. N<sub>2</sub> broadening was determined for temperatures up to 1100K. The temperature exponent ( $N$ ) was determined from equation 2.15, using a suitable log plot as shown in Fig. 4.12. The slope of the line gives a value for the temperature exponent,  $N=0.348$ , which is in good agreement with the theoretical predictions,  $N=0.35$  of Delaye et al. [11]



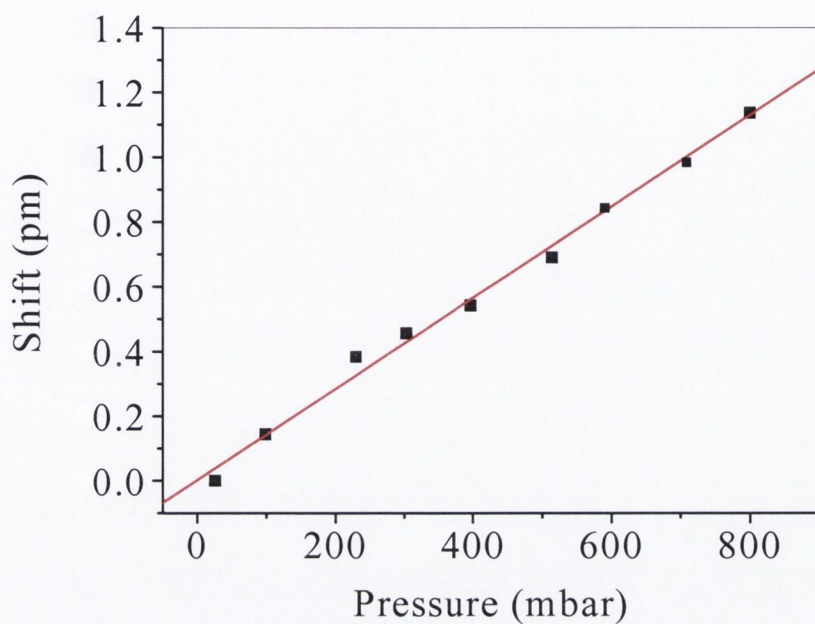


**Figure 4.9.** Measured spectral line shift versus pressure at 296K. The linear best-fit is shown where the shift coefficient is calculated from slope.

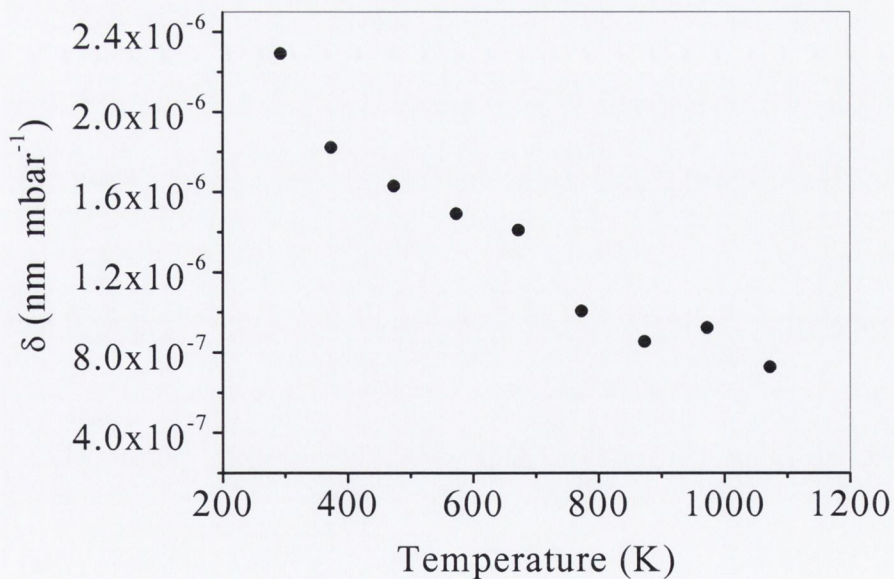


**Figure 4.10.** Plot of measured shift coefficient as a function of temperature

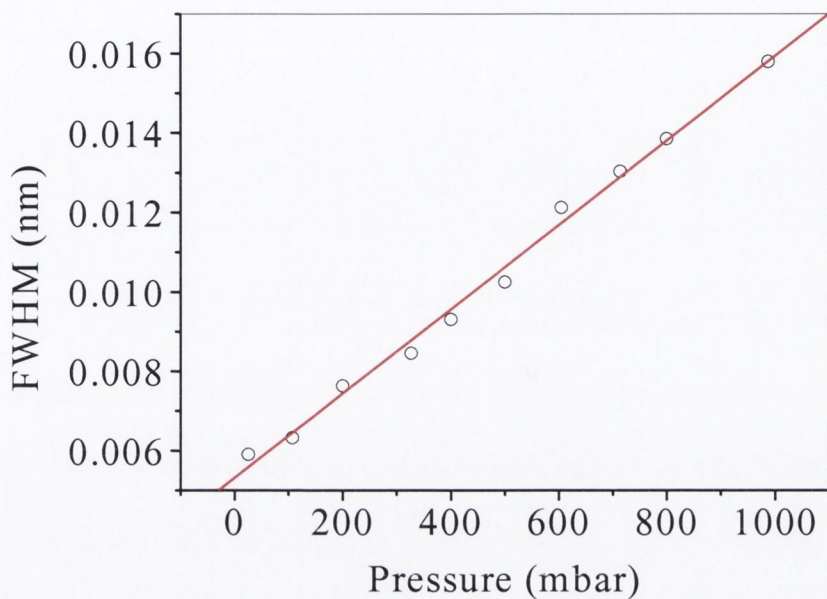


**Figure 4.11.** Collisional broadened linewidth versus pressure at 296K.

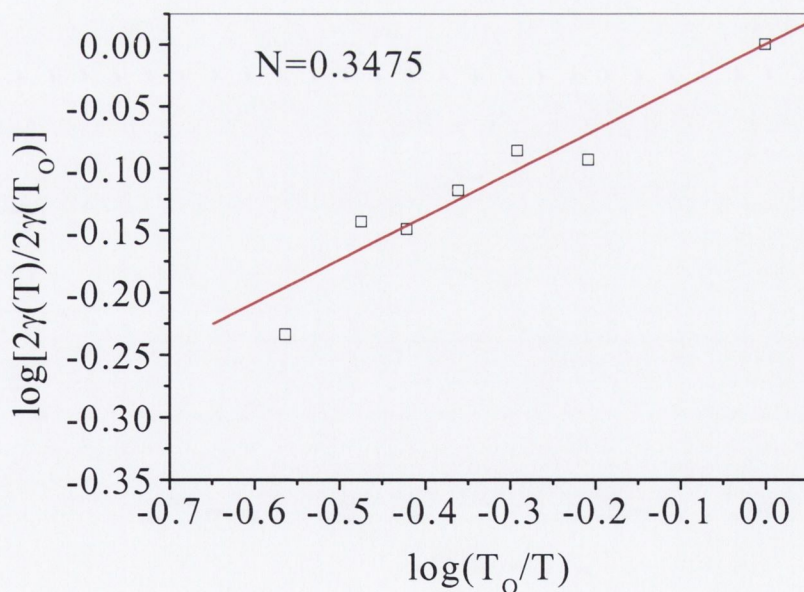


**Figure 4.12.** Logarithmic plot of Nitrogen broadening coefficient as a function of temperature.  $N$  is the calculated temperature exponent.



Any variation in line strength with temperature is another important issue with respect to absorption spectroscopy based gas sensing. Hence this parameter was also measured over a range of temperatures 296-1100K. Absorption profiles similar to that shown in Fig. 4.8(a), were determined for gas pressures in the range 0-20mbar. The area (A) under each absorbance profile was calculated and shown to increase linearly with pressure as depicted in Fig. 4.13. The line strength was determined by applying a linear fit to Fig 4.13, and using the slope to calculate the linestrength from the relationship,

$$S = \frac{A}{PL} \quad (4.1)$$

The line strength was determined for a range of temperatures and is shown in Fig. 4.14, together with values obtained from Hitran2000 database.[3] The line strength of the absorption profile at 1.3928um at 296K is summarised in table 4.1, and agrees well with values determined elsewhere [3, 12-14].

It can be seen from the graph (Fig. 4.14) that the maximum line strength value ( $0.019\text{cm}^{-2}\text{atm}^{-1}$ ) occurs at 673K and is four times that at 296K. This has obvious implications for accurate measurements of sample gas concentrations at elevated temperatures. The effect of spectral line strength variations with temperature can be quantified and depending on concentration accuracy required, a predetermined temperature dependent correction factor can be applied.

Hitran [3]	Toth [12]	S [ $\text{cm}^{-2} \text{atm}^{-1}$ ]		
		Partridge [13]	Parvitte [14]	measured
0.00590	0.00562	0.005454	0.00580	0.00550

**Table 4.1.** Summary of Line strength values for the absorption profile at 1.3928um (296K).

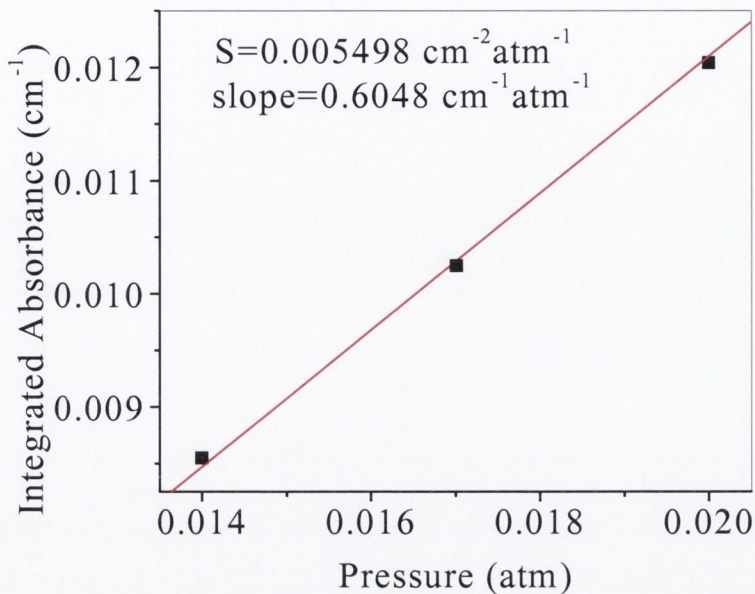


**Figure 4.13.** Integrated absorbance of the best-fit Voigt function at a range of pressures. The temperature was 296K and the path length 110cm. Note that the line strength is calculated from the slope.

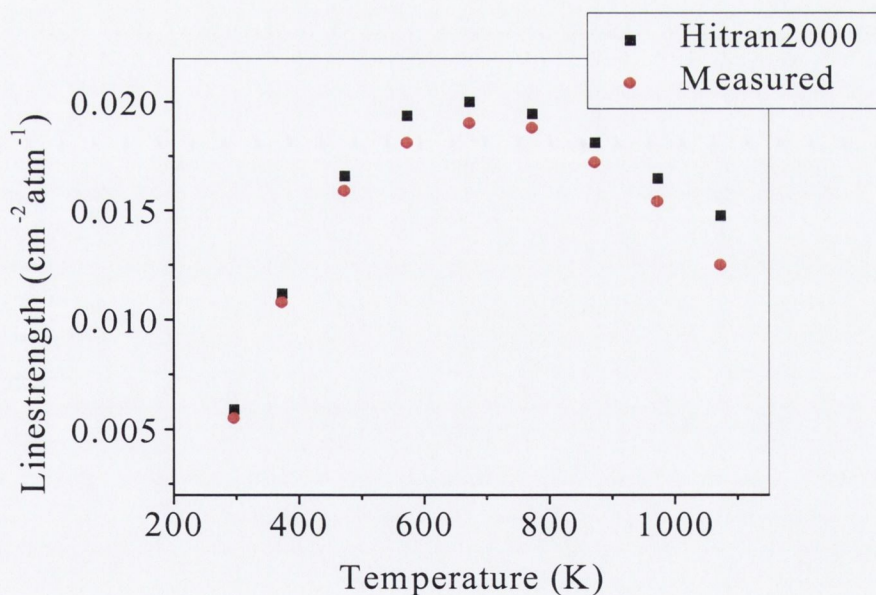


**Figure 4.14.** Measured values of the linstrength as a function of temperature in the range 300K – 1100K. Also shown are the values obtained from Hitran2000.



## 4.6 WMS $2f$ measurements

While direct absorption measurements are ideal for displaying strong absorption line profiles, the use of direct detection was found to be a poor method of measuring very small absorptions. Accordingly, we have investigated the capability of high sensitivity wavelength modulation spectroscopy techniques for quantitative shift measurements by analysing the accuracy with which line parameters can be retrieved by least squares fitting procedures. In this way the high sensitivity of WMS may also be useful for line parameters measurements in situations for which sufficient sensitivity is not achievable for direct detection.

WMS is a well-known technique for high sensitivity optical absorption measurements by use of diode lasers. Its advantage over direct detection is that it shifts the detection to higher frequencies where the  $1/f$  laser excess noise is reduced [15, 16]. It also removes much of the base line slope seen in the direct detection measurements. The  $2f$  components were used in the detection measurement of  $\text{H}_2\text{O}$  since the  $2f$  profile has a maximum amplitude, at the gas absorption line centre. The experimental arrangement is shown in Fig 4.15, and is similar to the direct detection set-up, but with the inclusion of a signal generator and two lock-in amplifiers. A 20kHz sine wave generated by the signal generator was added to the injection current to provide the wavelength modulation. The two lock-in amplifiers collected the  $2f$  signals and sent them to a PC. A LabVIEW™ program for generating WMS absorption profiles has been developed specifically for the purpose, to extract the typical line-shape and position parameters for the  $\text{H}_2\text{O}$  absorption line. The  $2f$  spectra were fitted using a non-linear Levenberg-Marquardt sub-routine (LabVIEW™) [17], which minimises the chi-squared parameter by adjusting the fitting parameters. The absorption line used in the direct detection measurements was also selected for the WMS measurements.



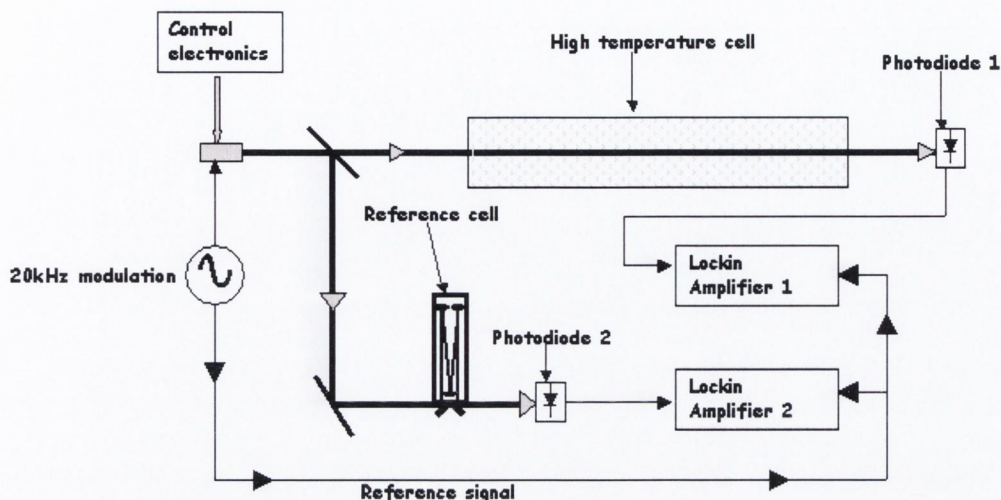


**Figure 4.15.** Schematic of the WMS experimental set-up for measurement of absorption lineshift.

## 4.7 WMS 2f Results

Voigt, Galatry and Rautian profiles were used to model the measured 2f spectra in the Dicke narrowing pressure region as shown in Fig 4.16. Fig. 4.16, also shows the residuals of the three profile fits to the measured H<sub>2</sub>O lineshape recorded with 5mBar of H<sub>2</sub>O in the cell. It is clear from the residuals in Fig 4.16 that Galatry and Rautian profiles more accurately fit the measured data compared with a Voigt profile, which does not account for the narrowing effect [18].

Typically a laser diode based open path sensing system will have a reference cell, filled with the target gas, in the transmitter to provide the means for locking the emission wavelength of the laser to the peak of the sample gas absorption line. Fig 4.17 shows the 2f absorption signal from the low pressure reference cell and the 2f absorption signal for varying temperature and pressure, from the high temperature cell. The shift is clearly apparent, which will compromise the accuracy of concentration measurement. For a pressure difference of 995mBar at 22<sup>o</sup>C as shown in Fig 4.17 (b) the inaccuracy in a concentration measurement is approximately 20% compared to an inaccuracy of 2% at 800<sup>o</sup>C shown in Fig 4.17 (d). In a gas sensing system using WMS, where the emission wavelength of the laser is locked using a reference cell the effect of



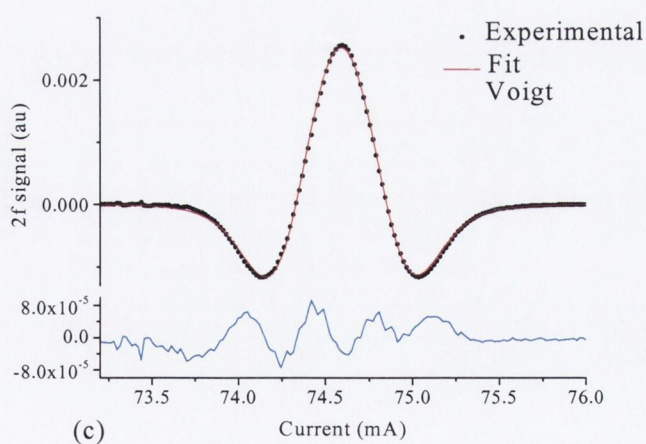
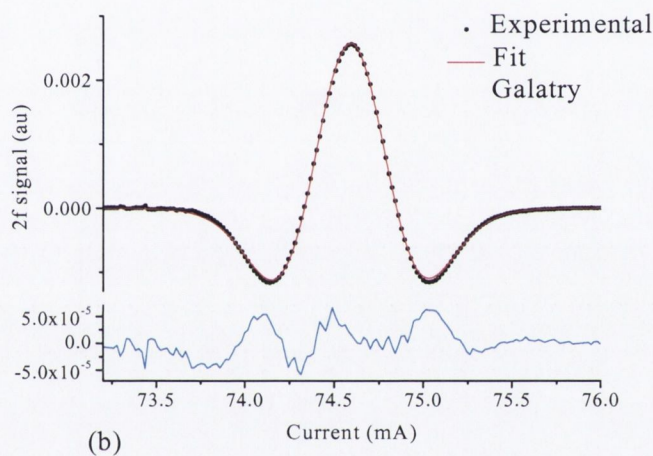
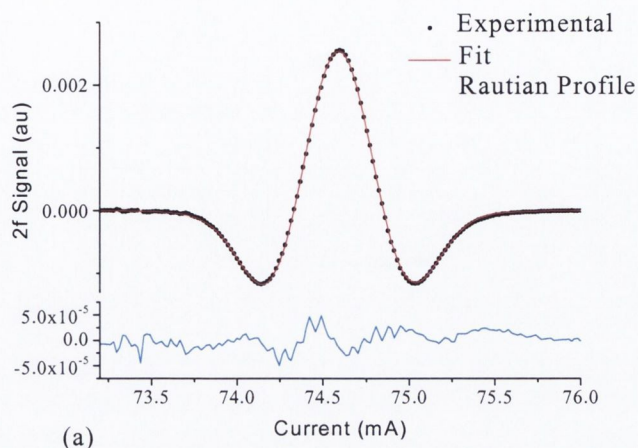


**Figure 4.16.** *2f* profile at a pressure of 5mbar (a) overlaid with best-fit Rautian profile (b) overlaid with best-fit Galatry profile and (c) overlaid with best-fit Voigt profile. Residual plots show the differences between data and the fitted spectral profiles.

the pressure induced spectral line shift on the targeted feature in the sample gas has a larger effect on concentration accuracy (compared with a direct detection system). The effect of this offset may be somewhat reduced by suitable choice of the reference cell pressure. For example with the measurement described above the optimum reference cell gas pressure to reduce the effects of spectral shift is 400mbar.

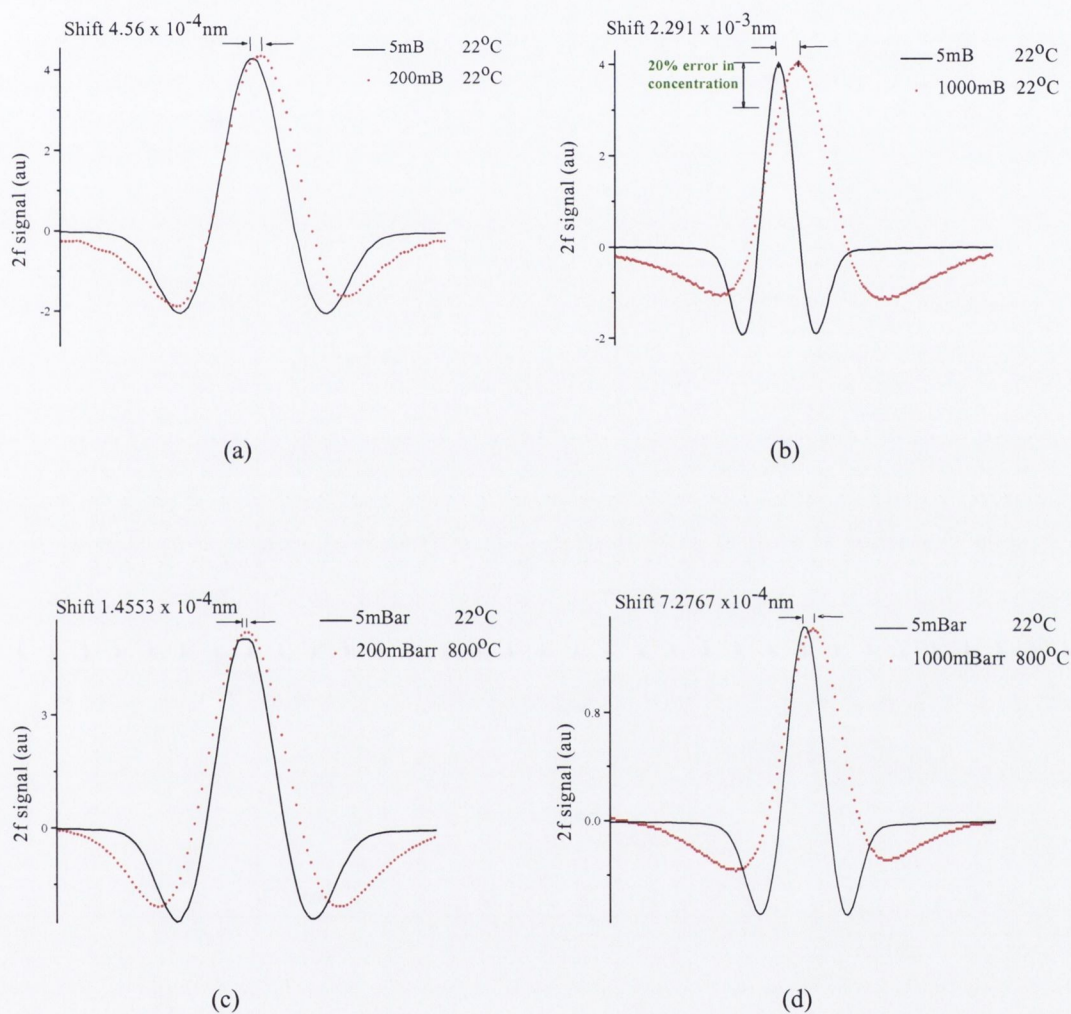


**Figure 4.17** Measured 2f  $N_2$ -pressure induced shifts of the  $H_2O$  rotational absorption line at (a) 200mBar, 22°C (b) 1000mBar, 22°C (c) 200mBar, 800°C (d) 1000mBar, 800°C



## 4.8 Conclusion

The effects of spectral line shift, line strength and  $N_2$  broadening on the water vapour line at  $1.3928\mu\text{m}$  for temperatures between 300K-1100K, and their impact on the accuracy of optical absorption based gas sensing has been investigated. Significant spectral parameters ( $S$ ,  $2\gamma$ ,  $N$ ,  $\delta$ ) for this absorption line were measured and were in good agreement with values obtained in literature. The high temperature gas cell performed well and is a simple and inexpensive apparatus enabling spectral characteristic measurements at elevated temperatures.

The dual-path direct absorption spectroscopy technique demonstrated above has enabled sensitive investigations into spectral changes with temperature and pressure. It has been also shown that in a gas sensing system using WMS, where the emission wavelength of the laser is locked using a reference cell the effect of the pressure induced spectral line shift on the targeted feature in the sample gas has a larger effect on concentration accuracy (compared with a direct detection system)

The effects of these spectral changes were quantified with respect to their impact on the accuracy of a laser diode based spectroscopic sensing system employing a line locking technique. The resultant strategic knowledge gained can be used to facilitate  $H_2O$  sensing in a non-standard temperature and pressure environment.

## 4.9 References

- [1] R. H. Dicke, "The effects of Collisions upon the Doppler Width of Spectral Lines," *Physical Review*, vol. 89, pp. 472-305, 1953.
- [2] R. S. Eng, A. Javan, T. C. Harman, A. R. Calawa, and P. L. Kelley, "Collisional Narrowing of Infrared Water-Vapor Transitions," *Applied Physics Letters*, vol. 21, pp. 303-306, 1972.
- [3] L. S. Rothman, A. Barbe, D. C. Benner, L. R. Brown, C. Camy-Peyret, M. R. Carleer, K. Chance, C. Clerbaux, V. Dana, V. M. Devi, A. Fayt, J. M. Flaud, R. R. Gamache, A. Goldman, D. Jacquemart, K. W. Jucks, W. J. Lafferty, J. Y. Mandin, S. T. Massie, V. Nemtchinov, D. A. Newnham, A. Perrin, C. P. Rinsland, J. Schroeder, K. M. Smith, M. A. H. Smith, K. Tang, R. A. Toth, J. Vander Auwera, P. Varanasi, and K. Yoshino, "The HITRAN molecular spectroscopic database: edition of 2000 including updates through 2001," *Journal of Quantitative Spectroscopy & Radiative Transfer*, vol. 82, pp. 5-44, 2003.
- [4] V. Nagali, S. I. Chou, D. S. Baer, and R. K. Hanson, "Diode-laser measurements of temperature-dependent half-widths of H<sub>2</sub>O transitions in the 1.4  $\mu$ m region," *Journal of Quantitative Spectroscopy and Radiative Transfer*, vol. 57, pp. 795-809, 1997.
- [5] M. P. Arroyo and R. K. Hanson, "Absorption-Measurements of Water-Vapor Concentration, Temperature, and Line-Shape Parameters Using a Tunable InGaAsP Diode-Laser," *Applied Optics*, vol. 32, pp. 6104-6116, 1993.
- [6] M. P. Arroyo, S. Langlois, and R. K. Hanson, "Diode-Laser Absorption Technique for Simultaneous Measurements of Multiple Gasdynamic Parameters



- in High-Speed Flows Containing Water-Vapor," *Applied Optics*, vol. 33, pp. 3296-3307, 1994.
- [7] V. Nagali, D. F. Davidson, and R. K. Hanson, "Measurements of temperature-dependent argon-broadened half-widths of H<sub>2</sub>O transitions in the 7117 cm<sup>-1</sup> region," *Journal of Quantitative Spectroscopy and Radiative Transfer*, vol. 64, pp. 651-655, 1999.
- [8] L. S. Rothman, K. Chance, and A. Goldman, "Special issue - Hitran - Preface," *Journal of Quantitative Spectroscopy & Radiative Transfer*, vol. 82, pp. 1-2, 2003.
- [9] P. L. Varghese and R. K. Hanson, "Collisional narrowing effects on spectral line shapes measured at high resolution," *Appl Opt*, vol. 23, pp. 2376-2385, 1983.
- [10] J. Humlicek, "An efficient method for evaluation of the complex probability function: the Voigt function and its derivative," *J Quant Spectrosc Radiat Transfer*, vol. 21, pp. 309-313, 1979.
- [11] C. Delaye, J. M. Hartmann, and J. Taine, "Calculated Tabulations of H<sub>2</sub>O Line Broadening by H<sub>2</sub>O, N<sub>2</sub>, O<sub>2</sub>, and CO<sub>2</sub> at High-Temperature," *Applied Optics*, vol. 28, pp. 5080-5087, 1989.
- [12] R. A. Toth, "Extensive Measurements of (H<sub>2</sub>O)-O-16 Line Frequencies and Strengths - 5750 to 7965 cm<sup>-1</sup>," *Applied Optics*, vol. 33, pp. 4851-&, 1994.
- [13] H. Partridge and D. W. Schwenke, "The determination of an accurate isotope dependent potential energy surface for water from extensive ab-initio calculations and experimental data," *Journal of Chemical Physics*, vol. 106, pp. 4618-4639, 1997.

- [14] B. Parvitte, V. Zeninari, I. Pouchet, and G. Durry, "Diode laser spectroscopy of H<sub>2</sub>O in the 7165-7185 cm<sup>-1</sup> range for atmospheric applications," *Journal of Quantitative Spectroscopy & Radiative Transfer*, vol. 75, pp. 493-505, 2002.
- [15] J. A. Silver and A. C. Stanton, "Optical Interference Fringe Reduction in Laser-Absorption Experiments," *Applied Optics*, vol. 27, pp. 1914-1916, 1988.
- [16] P. Kluczynski, J. Gustafsson, A. M. Lindberg, and O. Axner, "Wavelength modulation absorption spectrometry - an extensive scrutiny of the generation of signals," *Spectrochimica Acta Part B-Atomic Spectroscopy*, vol. 56, pp. 1277-1354, 2001.
- [17] B. F. W.H. Press, S. Teukolsky, W. Vetterling, *Numerical Recipes in C: The Art of Scientific Computing*: Cambridge University Press, 2002.
- [18] M. Lepere, "Line profile study with tunable diode laser spectrometers," *Spectrochimica Acta Part A: Molecular and Biomolecular Spectroscopy*, In Press, Corrected Proof.



# Chapter 5

## Simultaneous Multi-Gas Sensing using a Strongly Gain Coupled DFB laser diode

### 5.1 Introduction

Recent progress in the development and deployment of wavelength division multiplexing technologies for communications systems has led to a high demand for widely tuneable single wavelength lasers, that exhibit a single mode performance comparable with stand alone DFB lasers. Widely tuneable laser diodes are also very attractive for molecular spectroscopy because their tuning ability allows scanning of a large spectral interval, which makes it possible to detect several species of a gas mixture simultaneously. Recently, a new scheme was proposed by Hong and co-workers, in which a multi-wavelength laser is realised by placing a number of DFB laser diodes with different wavelengths in series (referred to as a laser cascade) [1-3]. This gives an expanded range of accessible wavelengths and a similar performance specification to a typical DFB laser diode.

In this chapter the use of a single strongly gain coupled (SGC) three-sectioned DFB laser cascade, configured for stable simultaneous operation at two wavelengths, for the detection of two gases Hydrogen Sulphide ( $H_2S$ ) and Carbon Dioxide ( $CO_2$ ) using wavelength modulation spectroscopy (WMS) [4, 5] was investigated. Also observed and investigated was thermal cross-talk between the lasing sections (section one and section two) when the laser is operated in a dual wavelength emission mode, a configuration in which the laser would not be operated for telecommunication applications. Stabilisation techniques to minimise the effect of this cross-talk have been investigated.



## 5.2 SGC-DFB Device

The laser is a multi-section InGaAsP/InP DFB structure. The unique feature of this device is that the laser cavity is divided into three cascaded sections ( $S_1$ ,  $S_2$  and  $S_3$ ) as shown in Fig. 5.1.

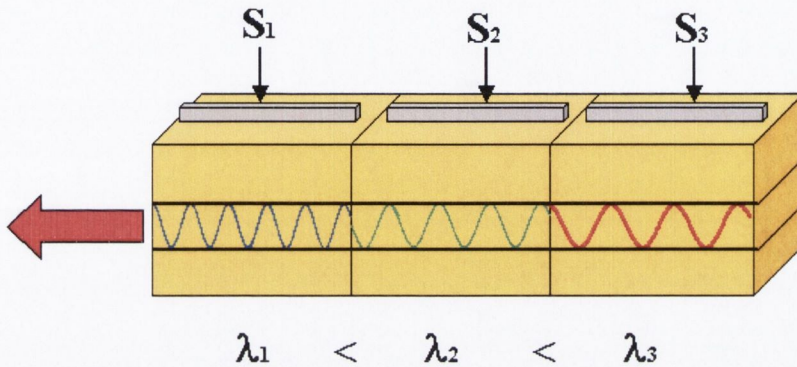


*Figure 5.1. Schematic diagram of three-section SGC cascaded DFB laser.*

Each section has a uniform grating with a different grating pitch. The Bragg wavelength of the front section is the shortest with the Bragg wavelength of each section shifted by approximately 5 nm relative to the adjacent section [6]. This allows light to pass transparently through the next section in the cascade without being reflected by the corresponding grating reflection band. The sections are separated by isolation trenches, which are several micrometers wide, so that each section can be biased independently. The laser cascade is mounted on a heat sink allowing operation in the range  $-5\text{ }^{\circ}\text{C} \leq T \leq 50\text{ }^{\circ}\text{C}$ . The SGC is hermetically sealed in a 26-pin butterfly package that contains a thermoelectric cooler, thermistor and an optical amplifier. Laser light exits the package through a single mode optical fibre.

In normal operation, the SGC laser device is continuously tuned to different wavelengths by varying the temperature between  $-5\text{ }^{\circ}\text{C} \leq T \leq 50\text{ }^{\circ}\text{C}$  and biasing one laser section at a time with the other two sections biased just below threshold to induce transparency. A wide tuning range of 15 nm has been demonstrated [1]. In the experiment described here  $S_1$  and  $S_2$  were biased simultaneously, in contrast to normal operation, providing a dual



wavelength emission, with  $S_3$  left unbiased. Dual wavelength operation is obtained by biasing  $S_1$  and  $S_2$  above threshold, which is approximately 12 mA for each section.

The temperature dependence of the single mode emission characteristics of the device was measured using an optical spectrum analyser. The 5 nm tuning range for each section is shown in Fig. 5.2.

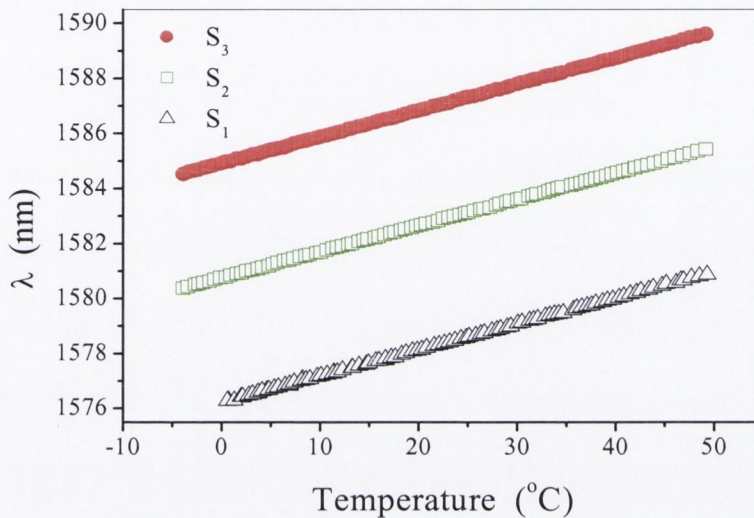


**Figure 5.2.** Measured SGC DFB emission wavelength dependence on temperature for the three sections at a constant current of 80 mA for each section, in the temperature range  $-5\text{ }^{\circ}\text{C} \leq T \leq 50\text{ }^{\circ}\text{C}$ .

The wavelength emission tunes approximately linearly with temperature at a rate  $\Delta\lambda/\Delta T = 9.50 \times 10^{-2}\text{ nm}/^{\circ}\text{C}$  for each section with bias currents of approximately 80 mA. In Fig. 5.3 the triple emission spectrum is shown when all three sections are biased simultaneously at approximately 50 mA at a laser heatsink temperature of  $3.6\text{ }^{\circ}\text{C}$ .

Each section lases in a single mode with an average SMSR of 30 dB, the SMSR varied between 50-20dB across the temperature tuning range of the device as shown in Fig 5.4. Fine control of the laser emission wavelength was achieved by adjustment of the injection current to the relevant section. Each section tuned approximately linearly with current at a rate  $\Delta\lambda/\Delta I = 1.43 \times 10^{-2}\text{ nm}/\text{mA}$ . A knowledge of the spectral performance over the temperature and current operational range is another important characteristic in assessing the suitability of these novel devices for sensing applications, as the linewidth

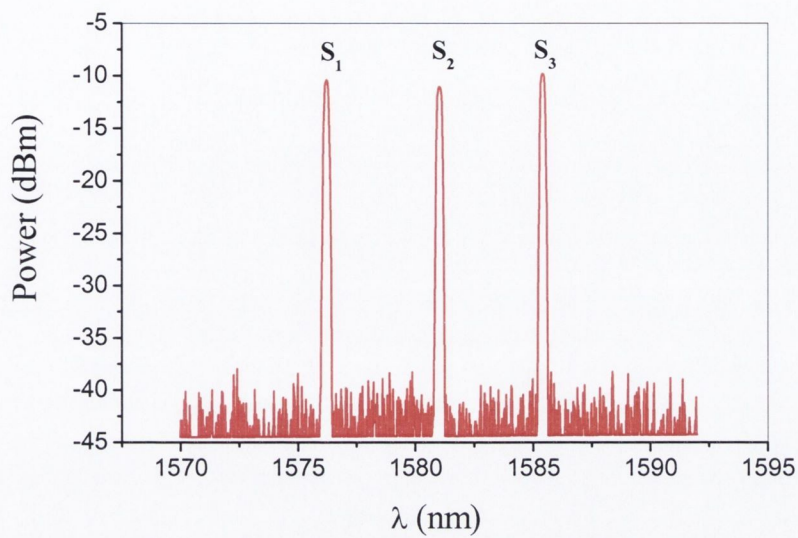


**Figure. 5.3.** Triple emission spectrum when all three laser sections are biased simultaneously at approximately 50 mA at a temperature of 3.6 °C.

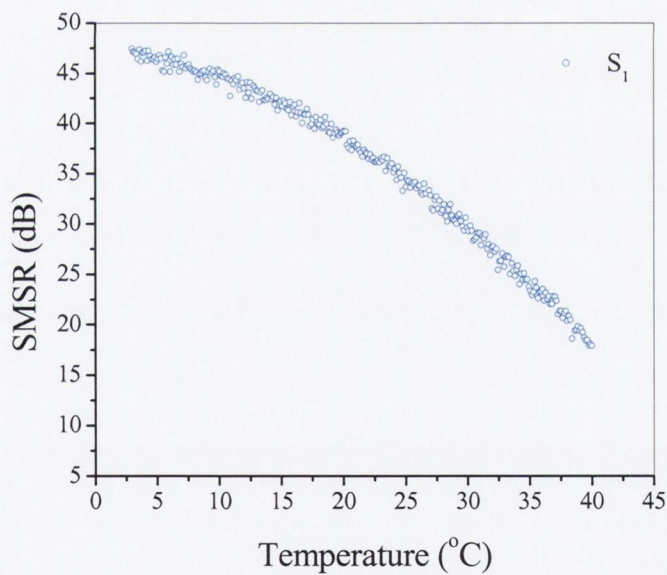


**Figure 5.4** SMSR variation with temperature tuning for  $S_1$  at a bias of 80mA.



is a measure of the system resolution. This was determined by the delayed self-Homodyne method as described in chapter 3. The emission linewidth ( $S_1$ ) of the SGC-DFB laser diode was measured to be consistently  $< 10\text{MHz}$  with a constant injection current of  $80\text{mA}$  in the temperature range  $0^\circ\text{C} \leq T \leq 40^\circ\text{C}$ .

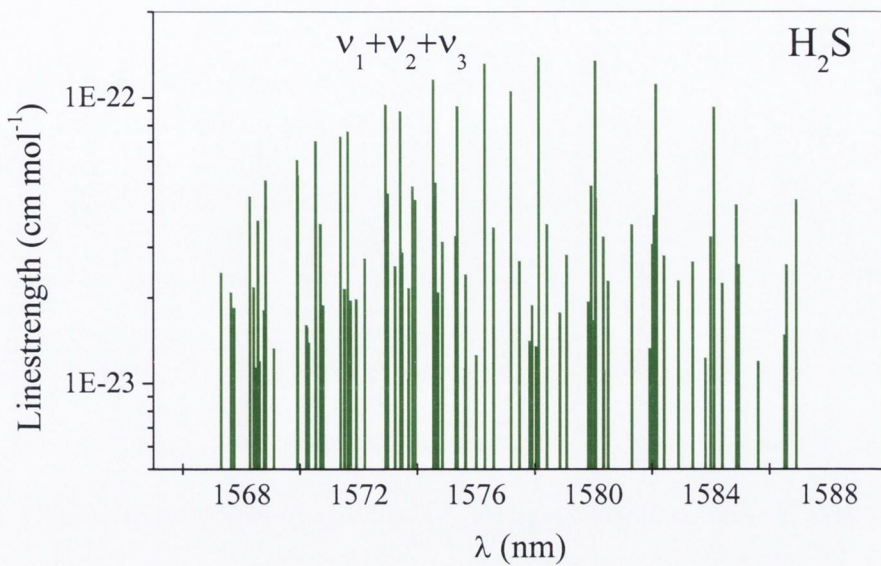
## 5.3 Near-Infrared Spectra of Target gases.

### 5.3.1 Hydrogen Sulphide ( $\text{H}_2\text{S}$ )

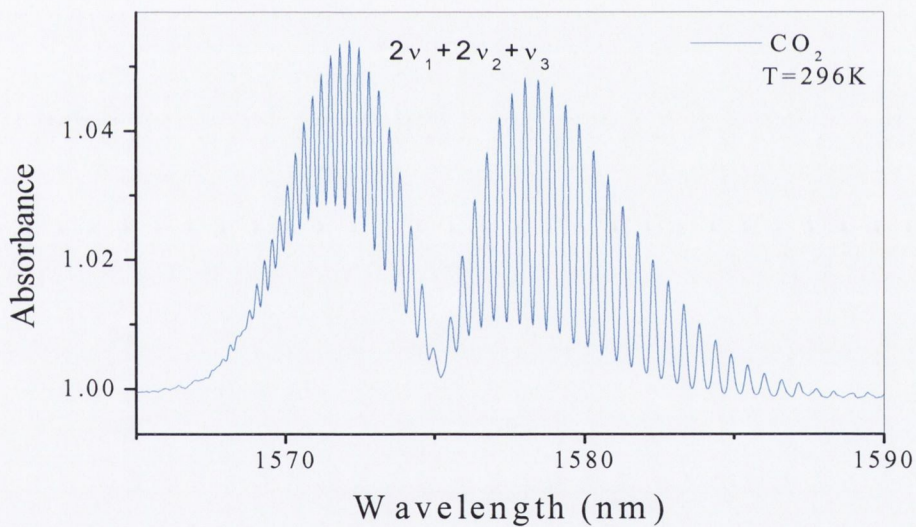
$\text{H}_2\text{S}$  is a highly toxic and flammable gas and is present in many processes in the oil and waste treatment industries, where concentrations levels above  $10\text{ppm}$  are considered hazardous [7], and thus is a valuable target species to monitor. The near-infrared spectrum of  $\text{H}_2\text{S}$  has been the subject of many high-resolution studies [8-10]. This band is actually composed of three overlapping combination and overtone bands namely the  $\nu_1+\nu_2+\nu_3$ ,  $2\nu_1+\nu_2$  and  $\nu_2+2\nu_3$  bands centred at  $1.58\ \mu\text{m}$ , the first one being the most intense which is shown in Fig. 5.5 (a). In this work we targeted the  $\text{H}_2\text{S}$  combination band  $\nu_1+\nu_2+\nu_3$  in the  $1.58\ \mu\text{m}$  spectral region with the single frequency emission from  $S_1$ .

### 5.3.2 Carbon dioxide ( $\text{CO}_2$ )

$\text{CO}_2$  is an important atmospheric constituent that exists at an average concentration of approximately  $356\text{ppm}$  [11] and is an important greenhouse gas. As a major product of hydrocarbon combustion,  $\text{CO}_2$  emissions are an indicator of combustion efficiency and have contributed to a global increase in atmospheric  $\text{CO}_2$  concentrations to their current levels. These high levels play an important role in the global energy balance, and as a result anthropogenic  $\text{CO}_2$  emissions might be regulated in the future in the form of carbon taxes. A FTIR plot of  $\text{CO}_2$  near infrared spectra is shown in Fig 5.5 (b). As the band labels on the plot reveal, the NIR is populated by weak overtone and combination bands. In this thesis we targeted the overtone-combination band  $2\nu_1+2\nu_2+\nu_3$  in the  $1.58\ \mu\text{m}$  spectral region [12] with the single frequency emission from  $S_2$ .



(a)



(b)

**Figure 5.5** (a) Absorption features from  $H_2S$  database [8] in the spectral region of the SGC-DFB (b)  $CO_2$ 's FTIR spectra with absorption bands labelled.



## 5.4 Experimental Details

The vibrational overtone/combination absorption line-strengths of gases in the near-infrared region of the spectrum are significantly less than the fundamental line-strengths in the mid-infrared. Hence high sensitivity WMS techniques were used for the simultaneous detection of  $\text{H}_2\text{S}$  and  $\text{CO}_2$  described here. WMS is a well known technique for high sensitivity optical absorption measurements by use of diode lasers. Its advantage over direct detection is that it shifts the detection to higher frequencies where the  $1/f$  laser excess noise is reduced. It also removes much of the base-line slope seen in direct detection. The  $2f$  components were used in the detection measurement of  $\text{H}_2\text{S}$  and  $\text{CO}_2$  since the  $2f$  profile has a maximum amplitude at the gas absorption line centre. The SGC laser was used in the WMS experimental set-up shown in Fig. 5.6.

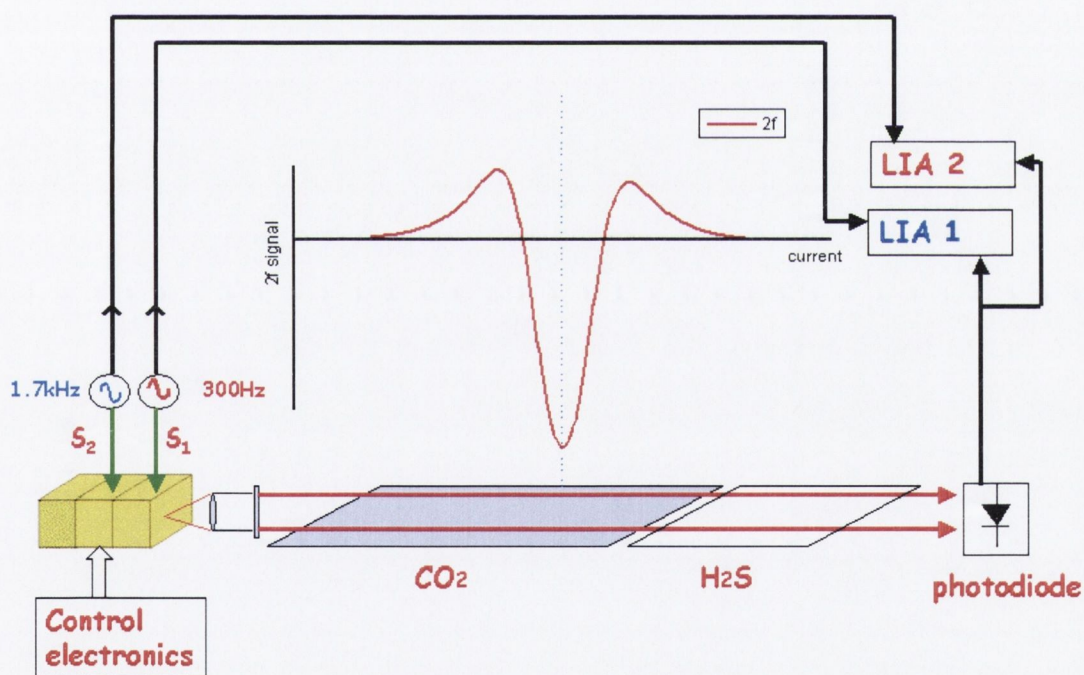


**Figure 5.6.** Schematic diagram of dual modulation WMS experimental set-up.

Simultaneous detection of  $\text{H}_2\text{S}$  and  $\text{CO}_2$  using WMS is achieved by independently modulating the front and middle sections at different frequencies ( $S_1$  at 300 Hz and  $S_2$  at



1.7 kHz) with a current modulation of 3.5 mA ( $S_1$ ), and 2.5mA ( $S_2$ ) (equivalent to a modulation depth 2.2 times the halfwidth of the absorption line). A pair of lock-in amplifiers operating at  $2f$  was used to process the WMS signals. These frequencies were deliberately chosen so that multiple relationships are avoided, reducing the potential cross-talk between the WMS detection systems. Little information regarding the optical amplifier was available from the manufacturer of the laser cascade and its full characterisation was not undertaken as part of the work described here. However, its noise characteristics as a function of bias current, in respect of its effect on laser emission was investigated. A bias current at 20 mA was found to give optimum noise performance and this value was used throughout the experiment. Under these conditions the typical optical output power of the laser with a section bias current of 60mA was 0.2mW for each section.

The experimental set-up involved directing the output of the device through two stainless steel sample cells with antireflection coated quartz windows placed in series containing 500 mbar of  $H_2S$  and  $CO_2$  and on to an InGaAs detector. For ease of measurement the magnitude of the signal levels from the  $H_2S$  and  $CO_2$  were arranged to be comparable by using a path length of 1 m for  $CO_2$  and a path length of 0.17 m for  $H_2S$ .

## 5.5 Simultaneous detection of $H_2S$ and $CO_2$

The dual independently modulated laser emission lines from  $S_1$  and  $S_2$  were simultaneously scanned (non-repetitively) across the  $H_2S$  and  $CO_2$  rotational absorption lines. The bias current of  $S_1$  and  $S_2$  were individually adjusted such that the wavelength of the two laser emission lines correspond with two rotational  $H_2S$  and  $CO_2$  absorption lines respectively, when the laser temperature was at  $3.6^\circ C$ . The measured second harmonic absorption signals are shown in Fig. 5.7. The wavelength of the  $H_2S$  and  $CO_2$  absorption lines detected by the emission from  $S_1$  and  $S_2$  were 1576.1 nm and 1581.0 nm respectively, as shown in Fig. 5.8. The identification of the target gas lines was confirmed by correlating its spectral position with  $H_2S$  and  $CO_2$  absorption lines from the HITRAN database [12]. Targeting these lines the detection limits of the gases were measured by buffering the cells with Nitrogen ( $N_2$ ) to a total pressure of 1000 mbar.  $N_2$  is transparent



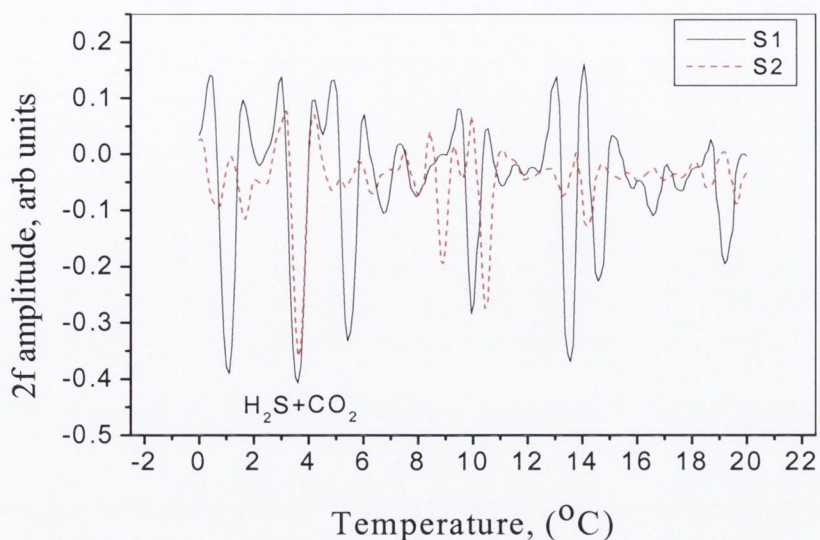


**Figure 5.7** Measured simultaneous  $2f$  absorption spectra of  $H_2S$  with the emission from  $S_1$  and  $CO_2$  with the emission from  $S_2$ , obtained by temperature tuning in the range  $0^\circ C \leq T \leq 20^\circ C$  while the drive currents of  $S_1$  and  $S_2$  were held constant at  $80mA$  and  $54mA$  respectively.

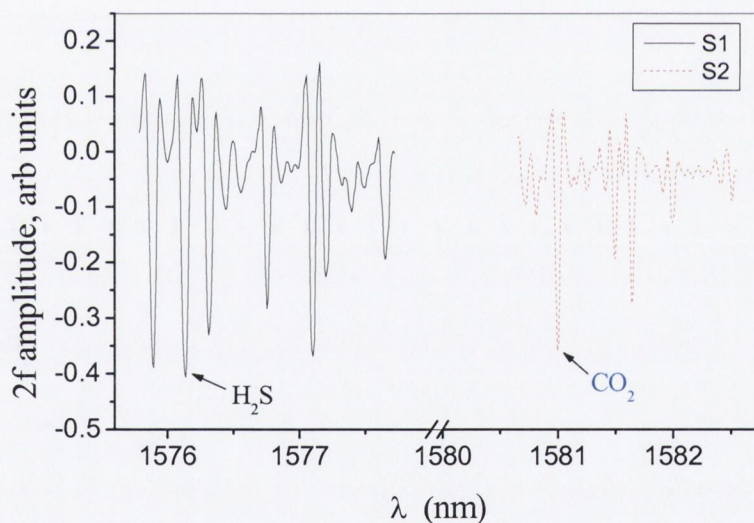


**Figure 5.8** Measured WMS absorption spectrum of  $H_2S$  and  $CO_2$  in the  $1576\text{ nm} \leq \lambda \leq 1581\text{ nm}$  region.

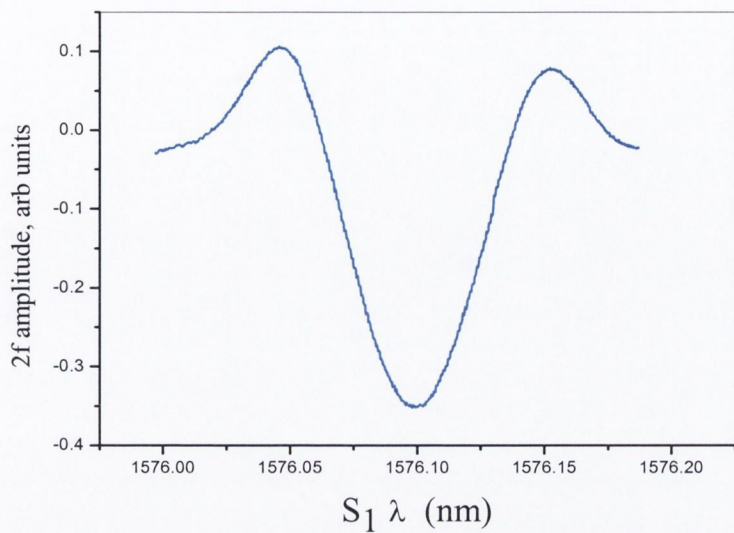
at this wavelength so its only contribution is to simulate atmospheric pressure measurement conditions. High-resolution spectra of these absorption lines were taken by current-tuning the emission wavelength from  $S_1$  and  $S_2$ , while holding the laser temperature constant at  $3.6\text{ }^{\circ}\text{C}$ , and are shown in Fig. 5.9. An integration time constant of 30 ms was set on the lock-in amplifier with a roll-off factor of 6dB/octave. This corresponds to an equivalent-noise detection bandwidth of 8.33Hz. The low detection limits were not directly measured but extrapolated from the signal to noise ratio (SNR) of the absorption signals. The SNR of the  $\text{H}_2\text{S}$  and  $\text{CO}_2$  absorption lines in Fig. 5.9 were calculated by measuring both the magnitude of the absorption and the high frequency noise over an integration time 30ms set by the lock-in amplifier. The SNR was calculated using equation (5.1).

$$\frac{S}{N} = \frac{(S_g - S_n)5}{\Delta S_n} \quad (5.1)$$

$$\frac{\Delta S_n}{5} = \sigma_n \quad (5.2)$$

where  $S_g$  is the signal level at the gas absorption line centre.  $S_n$  is the signal level with no gas present. The measured value  $\Delta S_n$  is the peak-to-peak spot noise. This value is obtained by assuming that the data is within a confidence interval  $\pm 2.5$  times the standard deviation,  $\sigma_n$ . SNR's of 1750 and 4498 were estimated, corresponding to minimum detection limits of  $7\text{ ppm.m.Hz}^{-1/2}$  and  $66\text{ ppm.m.Hz}^{-1/2}$  for  $\text{H}_2\text{S}$  and  $\text{CO}_2$  respectively. This is equivalent to an absorption detectivity for the system of  $1.51 \times 10^{-5}\text{ Hz}^{-1/2}$ . These detection levels are somewhat better than those achieved using widely tuneable multi-section DBR devices recently reported [13]. Of course, to achieve these detection limits in real-world applications, low frequency noise contributions from, for example, laser distortion and optical interference fringes which are not included here would need to be minimised. Also, the determination of sensitivity limits is best achieved using low-concentration samples. However, for simplicity, relatively large gas concentrations were used, since in the case of  $\text{H}_2\text{S}$  accurate calibration of low concentration levels is difficult





(a)

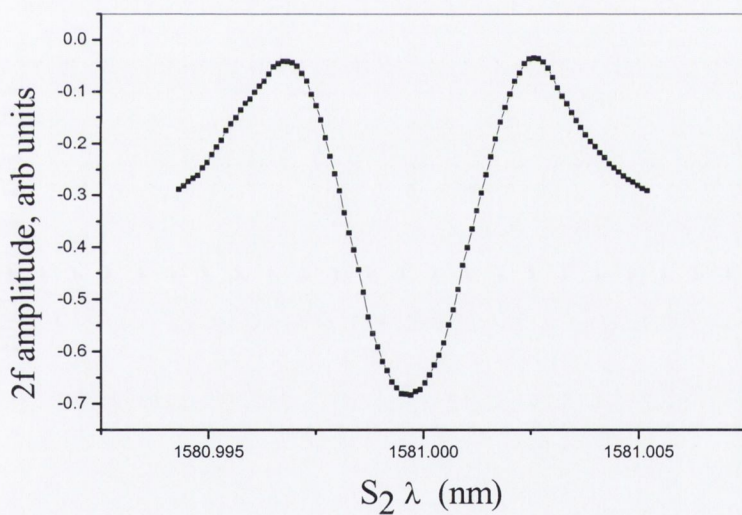


**Figure 5.9** Second harmonic WMS profile of the  $H_2S$  absorption line (a) observed while tuning the emission wavelength of  $S_1$  by current at a laser temperature of  $3.6\text{ }^\circ\text{C}$ , mod-depth of  $3.5\text{ mA}$  and (b) Second harmonic WMS profile of the  $CO_2$  absorption line detected with the emission wavelength of  $S_2$  at a laser temperature of  $3.6\text{ }^\circ\text{C}$ , mod-depth of  $2.5\text{ mA}$ .

given its great affinity for water vapour and its propensity for adsorption onto the walls of the sample cell [14].

## 5.6 Feedback control and stabilisation

One characteristic of the SGC laser when operating in a dual wavelength emission mode is thermal cross-talk [2] between the lasing sections which complicates somewhat the setting of emission wavelength of  $S_1$  and  $S_2$ . Fig. 5.10 shows the effect of tuning the emission wavelength of  $S_1$  by current across the  $H_2S$  absorption line, as a function of the bias current in  $S_2$  at a constant laser temperature of  $3.6^\circ C$ . The current-induced thermal interaction results in the temperature and hence the emission wavelength of  $S_1$  increasing with  $S_2$  bias current. A reduction in the  $S_1$  bias current of 4.5 mA is required to maintain the emission wavelength constant when the bias current in  $S_2$  is increased from 0 to 60 mA as shown in Fig. 5.10.

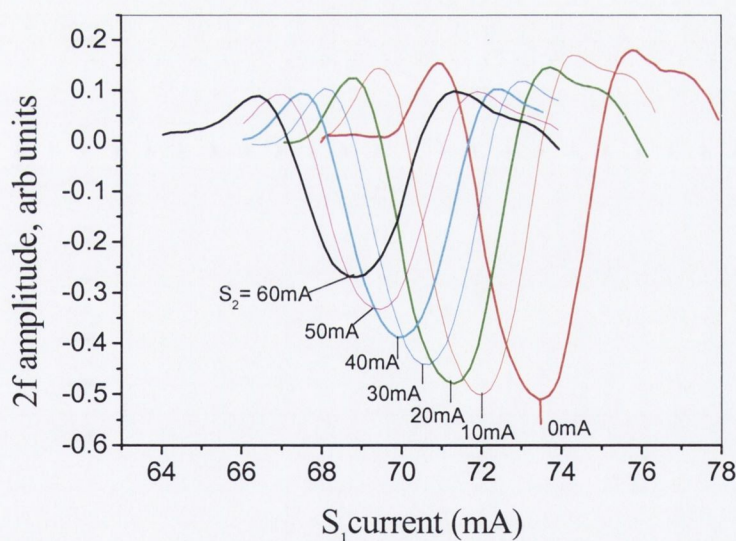


**Figure 5.10** Second harmonic WMS profile of the  $H_2S$  absorption line at  $1576.1nm$  observed while tuning the emission wavelength of  $S_1$  by current as a function of  $S_2$  bias current.



The current reduction corresponds to a temperature increase in  $S_1$  of  $1.4\text{ }^{\circ}\text{C}$ . The decrease in amplitude of the  $S_1$  WMS signal as the bias current in  $S_2$  is increased is a result of the output power of  $S_1$  decreasing due to the emission from  $S_2$  being amplified by  $S_1$ . Normalising the  $2f$  signal to the power can compensate for the power decrease. As the power at the detector associated with  $S_1$  and  $S_2$  cannot be distinguished, the  $1f$  components can be used for normalisation [15]. The current modulation on  $S_2$  also affects the emission wavelength of  $S_1$ . The influence of the thermal cross talk on the setting of the emission wavelength of  $S_1$  bias current, necessary to maintain constant emission wavelength, is depicted as a function of  $S_2$  bias current in Fig. 5.11.

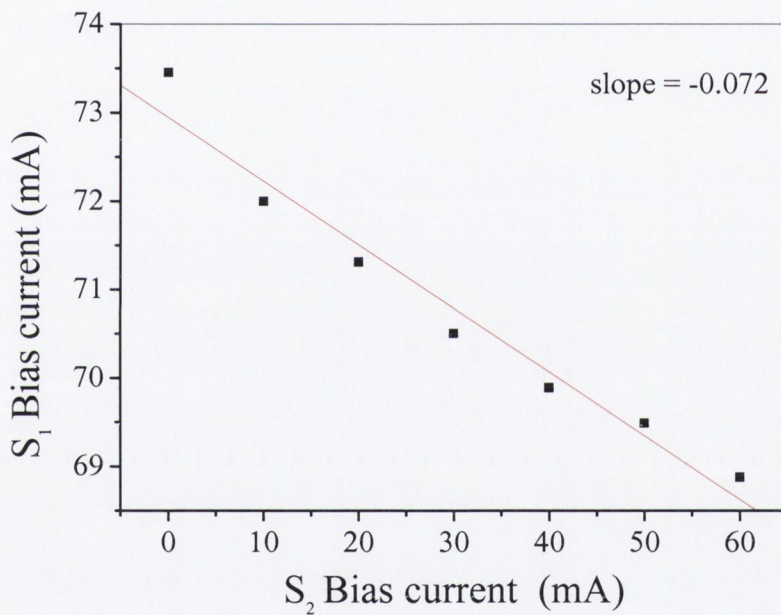


**Figure 5.11** Influence of thermal cross-talk between the lasing sections. The adjustment in  $S_1$  bias current necessary to maintain constant emission wavelength, is depicted as a function of  $S_2$  bias current.

For example when the bias current of  $S_2$  is modulated with a modulation depth of  $2.5\text{mA}$  this corresponds to a wavelength shift in the  $S_1$  equivalent to a bias current change of  $0.18\text{mA}$  ( $2.57 \times 10^{-3}\text{ nm}$ ). This may be derived from the slope of the fitted line in Fig. 5.11. This modulation results in a broadening of the measured  $2f$  line shape by approximately

8%. We have observed that the transfer function (slope Fig. 5.11) does not change appreciably from the D.C value, over the frequency range used.

For continuous long term monitoring of a gas, the laser wavelength of  $S_1$  must be fixed at the gas line centre, where the peak height of the  $2f$  signal is related to the concentration. In the absence of active control of the laser wavelength, the wavelength set by  $S_1$  will vary due to changes in the  $S_2$  bias current. The use of an optical absorbance for wavelength stabilisation is generally known as line-locking [16, 17]. To overcome the effect of thermal cross-talk a line-locking technique for active control of the  $S_1$  emission wavelength is introduced. The experimental set-up for the line-locking stabilisation technique is illustrated in Fig. 5.12.

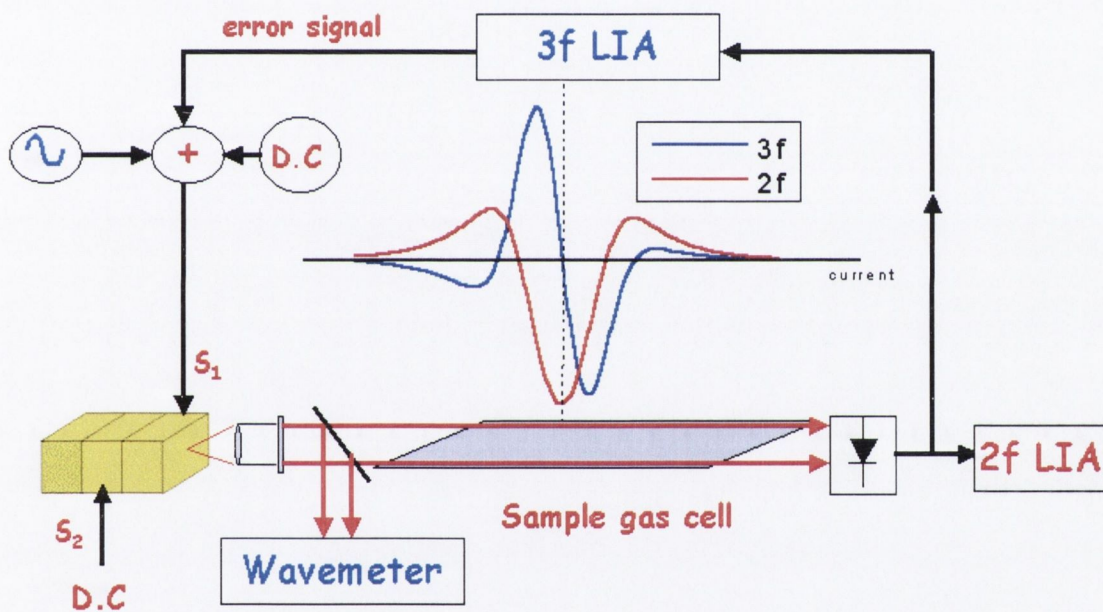


**Figure 5.12** Schematic diagram of line locking set-up.

Demodulation of the detector photocurrent at  $3f$  by a lock-in amplifier provides the wavelength stabilisation signal. The  $3f$  signal is preferred over the much stronger  $1f$  signal because  $1f$  signals are characterised by baseline offsets that occur as a result of laser power changes with current (wavelength). The  $3f$  signal of the  $H_2S$  line (as shown in Fig. 5.12) from the lock-in amplifier is zero at the line centre while deviations from the line centre cause the output to vary approximately linearly with the wavelength error.



This error signal is fed back to the current source of  $S_1$  to lock the emission wavelength of  $S_1$  to the absorption line of interest.

The result of this line-locking stabilisation technique can be seen in Fig. 5.13. With the line-locking off, the emission wavelength of  $S_1$  can be seen increasing as  $S_2$  bias current is increased from 0 to 60 mA. This is a result of the increase in temperature, which shifts the emission of  $S_1$  to longer wavelengths. With the line-locking operating, the emission wavelength from  $S_1$  is held at the gas absorption line centre as  $S_2$  bias current is increased. The bias current in  $S_1$  is being reduced by the  $3f$  wavelength error signal to compensate for this increase in temperature as shown in Fig. 5.13. The combination of line-locking and wavelength modulation spectroscopy suggests a method for continuous monitoring of a selected gas in which line-locking maintains the laser wavelength coincident with the centre of the absorption line of the target gas, while the concentration of a sample can be determined using demodulation at  $2f$ .

The line-locking technique may also be used to lock the emission wavelength of  $S_2$  to the  $\text{CO}_2$  absorption line, enabling independent operation of each section.

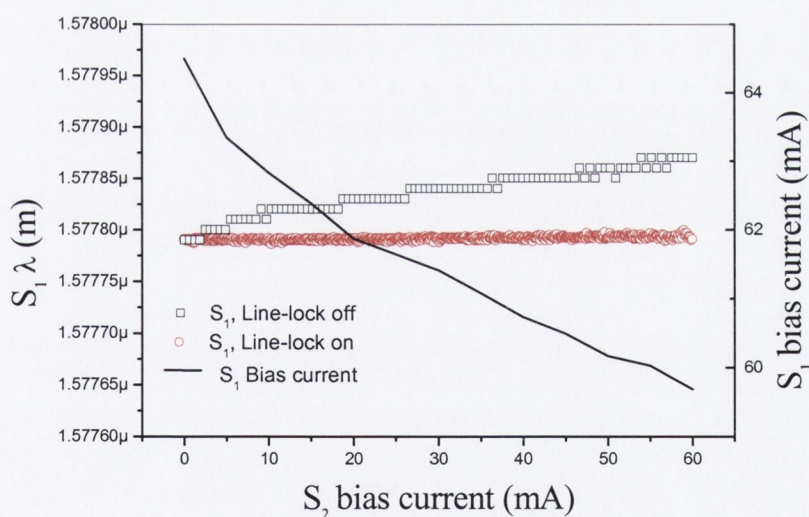


**Figure 5.13** Emission wavelength of  $S_1$  as a function of  $S_2$  bias current with line locking off and on. The  $S_1$  bias current is also depicted showing the effect of the feedback.

## 5.7 Conclusion

The first application of a SGC DFB laser cascade to simultaneous multigas sensing by operating the device in a dual wavelength emission regime is reported. Using a dual WMS technique, detection sensitivities of 7 and 66 ppm.m.Hz<sup>-1/2</sup> for H<sub>2</sub>S and CO<sub>2</sub> respectively were obtained. The operation to select the desired dual wavelength is simple and straightforward. However a characteristic of operating the SGC laser in a dual wavelength emission mode is the introduction of thermal cross talk between the lasing sections, which complicates somewhat the setting of the emission wavelength of S<sub>1</sub> and S<sub>2</sub>. The effect of the thermal cross talk, in particular its influence on lineshape profiles, is an area of ongoing study.

A line-locking technique to stabilise the emission wavelength of S<sub>1</sub> has been demonstrated. The line-locking technique can also be configured so as to simultaneously lock the wavelength of S<sub>2</sub> to the CO<sub>2</sub> absorption line. The combination of the two suggests a method for simultaneous monitoring of two selected gases.

Initial measurements described here confirm that SGC lasers developed for telecommunications industry are feasible light sources for sensitive absorption based simultaneous gas detection.



## 5.8 References

- [1] J. Hong, M. Cyr, H. Kim, S. Jatar, C. Rogers, D. Goodchild, and S. Clements, "Cascaded strongly gain-coupled (SGC) DFB lasers with 15nm continuous-wavelength tuning," *Photonics Technology Letters, IEEE*, vol. 11, pp. 1214-1216, 1999.
- [2] J. Hong, R. Finlay, R. Tong, C. Rogers, and D. Goodchild, "Simultaneous dual-wavelength operation in cascaded strongly gain-coupled DFB lasers," *Photonics Technology Letters, IEEE*, vol. 11, pp. 1354-1356, 1999.
- [3] J. Hong, H. Kim, F. Shepherd, C. Rogers, B. Baulcomb, and S. Clements, "Matrix-grating strongly gain-coupled (MC-SGC) DFB lasers with 34nm continuous wavelength tuning range," *Photonics Technology Letters, IEEE*, vol. 11, pp. 515-517, 1999.
- [4] J. Reid, D. Labrie, "Second-Harmonic Detection with Tunable Diode Lasers - Comparison of Experiment and Theory," *Applied Physics*, vol. B, pp. 203-210, 1981.
- [5] J. A. Silver, "Frequency-Modulation Spectroscopy for Trace Species Detection - Theory and Comparison among Experimental Methods," *Applied Optics*, vol. 31, pp. 707-717, 1992.
- [6] C. F. C. R. L. Baker, M. Cyr, D. R. Daniel, J. Hong, C. C. Rolland, A. G. Self, M. Svilans, and B. Villeneuve, "Tunable Sources," in *Laser Focus World*, March, 1999.

- [7] G. Modugno, C. Corsi, M. Gabrysch, and M. Inguscio, "Detection of HS at the ppm level using a telecommunication diode laser," *Optics Communications*, vol. 145, pp. 76-80, 1998.
- [8] J.-M. F. L. Lechuga-Fossat, C. Camy-Peyret, P. Arcas and M. Cuisenier, "The H<sub>2</sub>S Spectrum in the 1.6 $\mu$ m Spectral Region," *J. Mol. Phys*, vol. 61, pp. 23-32, 1987.
- [9] N. O. BYKOV AD, SMIRNOV MA, SINITSA LN, BROWN LR, CRISP J, CRISP D, "THE INFRARED-SPECTRUM OF H<sub>2</sub>S FROM 1 TO 5 $\mu$ m," *CANADIAN JOURNAL OF PHYSICS*, vol. 72, pp. 989-1000, 1994.
- [10] H. C. ALLEN, and PLYLER, E.K, "Infrared spectrum of hydrogen sulphide in the 6290 cm<sup>-1</sup> region," *J. Res. Natl. Bur. Stand*, vol. 52, pp. 169-502, 1954.
- [11] J. H. S. a. S. N. Pandis, *Atmospheric Chemistry and Physics: From Air Pollution to climate Change*: John Wiley & sons, 1998.
- [12] L. S. Rothman, C. P. Rinsland, A. Goldman, S. T. Massie, D. P. Edwards, J. M. Flaud, A. Perrin, C. Camy-Peyret, V. Dana, J. Y. Mandin, J. Schroeder, A. McCann, R. R. Gamache, R. B. Wattson, K. Yoshino, K. V. Chance, K. W. Jucks, L. R. Brown, V. Nemtchinov, and P. Varanasi, "The HITRAN molecular spectroscopic database and HAWKS (HITRAN Atmospheric Workstation): 1996 edition," *Journal of Quantitative Spectroscopy & Radiative Transfer*, vol. 60, pp. 665-710, 1998.
- [13] K. Boylan, V. Weldon, D. McDonald, J. O'Gorman, and J. Hegarty, "Sampled grating DBR laser as a spectroscopic source in multigas detection at 1.52-1.57  $\mu$ m," *IEE Proceedings-Optoelectronics*, vol. 148, pp. 19-24, 2001.



- [14] V. Weldon, "Spectroscopic Based Gas Sensing using Single Frequency Near Visible/Infrared Laser Diodes," Ph.D thesis: Trinity College Dublin, 1997.
- [15] J. 14. REID, Shewchun, B., Garside, K. and Ballik, "High sensitivity pollution detection employing tunable diode lasers," *Applied Optics*, vol. 17, pp. 300-307, 1978.
- [16] B. D.S, "Dual-modulation line-locking scheme," *Applied Optics*, vol. 30, pp. 2922-2924, 1991.
- [17] Y. Sakai, S. Sudo, and T. Ikegami, "Frequency stabilization of laser diodes using 1.51-1.55  $\mu\text{m}$  absorption lines of  $\text{C}_2\text{H}_2$  and  $^{13}\text{C}_2\text{H}_2$ " *Quantum Electronics, IEEE Journal of*, vol. 28, pp. 75-81, 1992.

# Chapter 6

## Multi-Species Gas Sensing using a SG-DBR and MG-Y laser Sensing and Absorption Line Identification

### 6.1 Introduction

Widely tuneable single frequency lasers, such as sampled grating distributed Bragg reflector and modulated grating Y-branch laser diodes recently developed for optical communications, present exciting opportunities for applications in absorption based multi-gas sensing regimes. Such wide wavelength tuning is not possible with conventional single frequency DFB and DBR lasers, and hence their use is limited to the detection of one gas. Widely tuneable laser diodes are more complex than standard DFB lasers used for single-species gas sensing and have undesirable artefacts in their operating characteristic. The tuning ranges of the widely tuneable lasers have been characterised and look-up tables, which yield high wavelength accuracy and high SMSR across the tuning range.

The use of widely tuneable laser diodes as sources in a multi-gas analysing system using wavelength modulation spectroscopy and second harmonic detection of acetylene hydrogen cyanide and ammonia have been investigated. The critical issues relevant to the application of such widely tuneable diode lasers to spectroscopic based high selectivity multi-gas sensing are outlined. The general emphasis of the work described in this chapter is not on detection limits but to selectively detect three gases with overlapping absorption bands.



Tuneable lasers are important components for next generation dense wavelength division multiplexing fibre optic networks. The wide tuning range and ability for fast wavelength switching make widely tuneable lasers especially attractive for multi-channel DWDM networks. To manage the channel wavelength of DWDM systems, wavelength-monitoring techniques are required. The use of multiple gas absorption lines for wavelength monitoring potentially offers a high degree of accuracy. The gas absorption lines have a typical FWHM of a few hundred MHz at low pressure and their wavelength dependence on temperature is such that active temperature control and stabilisation, which is necessary for other methods, is not required. The use of multiple gases to provide unique wavelength identifiers to provide monitoring of the lasing wavelength have been investigated.

## 6.2 Advanced static characterisation.

Multi-species gas sensing using widely tuneable lasers poses unique challenges compared with telecommunications applications of these devices and also compared with state-of-the-art single-species gas sensing. By now, it should be clear that the control of integrated tuneable laser diodes introduced in chapter three is rather complex. Wavelength control in a widely tuneable laser requires the alignment of reflection peaks from two grating mirrors with a cavity mode at the desired wavelength. This entails control of four separate currents to achieve complete wavelength coverage over the entire tuning range. Characterisation of these devices and selection of the optimum bias current operating points is important to demonstrate suitability for multi-gas sensing. These operating points will be selected on the basis of device linearity and distortion, output power and the ease of tuning to the relevant gas absorption lines.

The two control currents, which offer the most information with respect to characterising the laser devices, are the two coarse reflector-tuning currents. In the case of the SG-DBR these currents are the front and back grating currents ( $I_F$ ,  $I_B$ ), and for the MG-Y laser the left and right grating currents ( $I_L$ ,  $I_R$ ). The extended tuning ranges of the devices were measured using the experimental set-up illustrated in Fig 6.1.



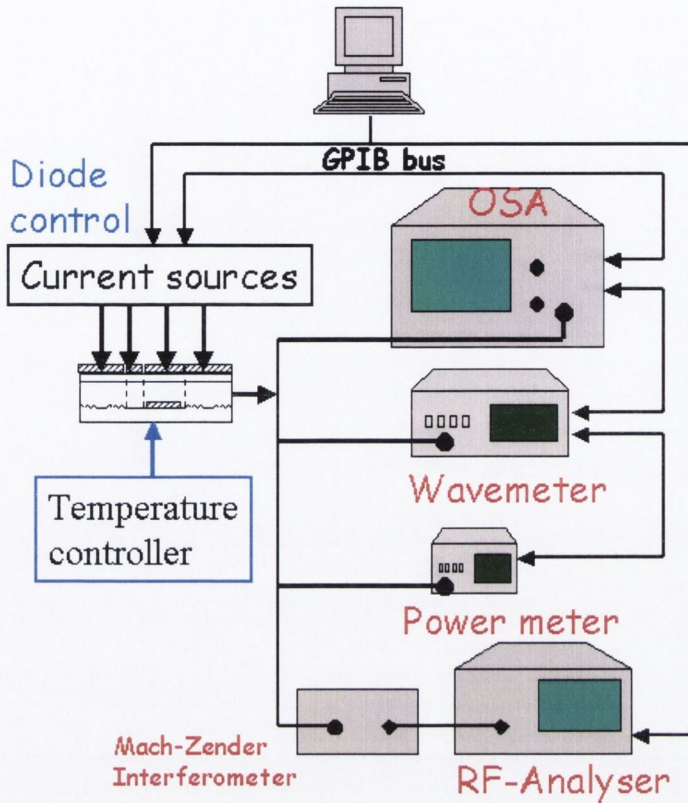


**Figure 6.1** Experimental arrangement for measuring characteristics.

The current sources biasing the laser, the optical wavelength meter, optical spectrum analyser, RF analyser and power meter are controlled by a computer using a GPIB card. With this arrangement the coarse tuning currents are set autonomously and the power and wavelength are measured at each point. Fig 6.2 (a) is an example of a wavelength-plane for the SG-DBR as a function of the coarse tuning currents. The active section was biased at 120mA ( $I_G$ ), no current was applied to the phase section and the heatsink temperature was fixed at 20°C. As illustrated in Fig 6.2 (b), on the wavelength surface, several plateaus are apparent, each corresponding to the coincidence of a pair of reflectivity peaks of the two SG-DBR mirrors and termed a super-mode. Along the super-mode, smaller wavelength hops can be observed, corresponding to cavity mode jumps. Fig 6.3 is a plot of the wavelength plane for the MG-Y laser with the active section biased at 150mA, phase section left unbiased and a heatsink temperature of 25°C. The contour plots in Fig 6.2 and 6.3 clearly identify eight super-modes per device with a wavelength



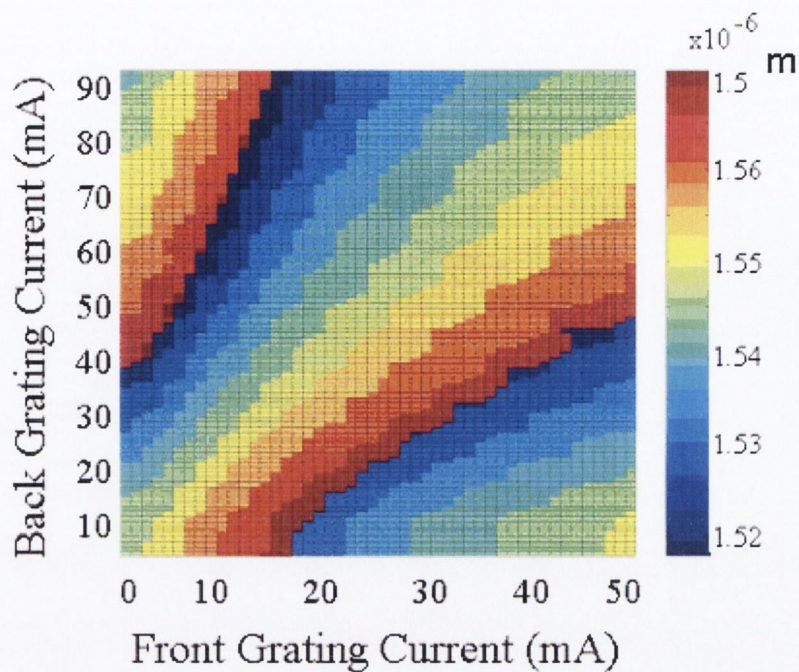
tuning range between 1520-1570nm, which is equal to the repeat mode spacing of 50nm. The repeat mode wavelength spacing occurs when the overlap of the reflection spectra of both grating reflections repeat.

The SMSR was measured as a function of the two coarse tuning currents for the SG-DBR and MG-Y laser as shown in Fig 6.4. The optical spectrum was measured for each operating point in the plane, and the SMSR value extracted as described in chapter 3. The plots clearly show a well-defined region in the SMSR value as the laser undergoes a super-mode change. In between these mode boundaries, there is a large, almost flat region, in which any chosen operating point can be guaranteed to have a SMSR of 35-40dB for the SG-DBR and 40-45dB for the MG-Y laser. The higher value for the MG-Y laser can be attributed to the additive Vernier effect. However the SMSR falls off gradually toward the super-mode boundaries in the MG-Y laser, resulting in large areas of poor SMSR compared with the SG-DBR.

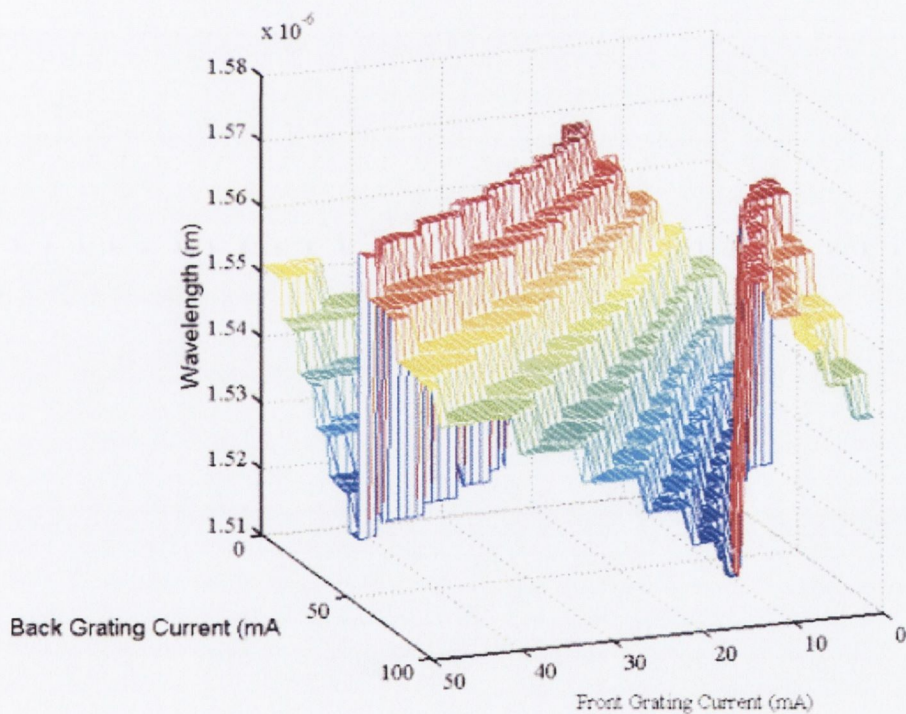
Fig 6.5 are examples of power-planes for each of the device type as a function of their coarse tuning currents. The phase and gain currents are kept constant. Effectively they represent a build-up of LI-curves. The sudden jumps in power can be attributed to mode-hops. A larger power variation with tuning is observed in the SG-DBR compared with the MG-Y laser, resulting from free carrier absorption in the front grating as light exits the laser through this mirror. In the MG-Y case light can exit the cavity without absorption enabling higher and more uniform power variation across the tuning range.

The contour plots shown in the previous figures contain all the relevant information for setting the emission from the laser to a specific wavelength, output power and SMSR. Any point on these contour plots can be selected with the correct front and back grating current combination. From a practical point of view it should be possible to set the laser wavelength to a certain wavelength using simple digital commands. A computer should then translate these into the appropriate values of the lasers control currents. For this, a look-up table of operation points is needed.





(a)



(b)

**Figure 6.2** (a) Emission wavelength of the SG-DBR laser as a function of the front and back tuning currents,  $I_F$  and  $I_B$ , at fixed phase current  $I_P = 0\text{mA}$  and active section current  $I_G = 120\text{mA}$ . (b) 3-d plot of figure 6.2(a) repeat mode spacing clearly visible.



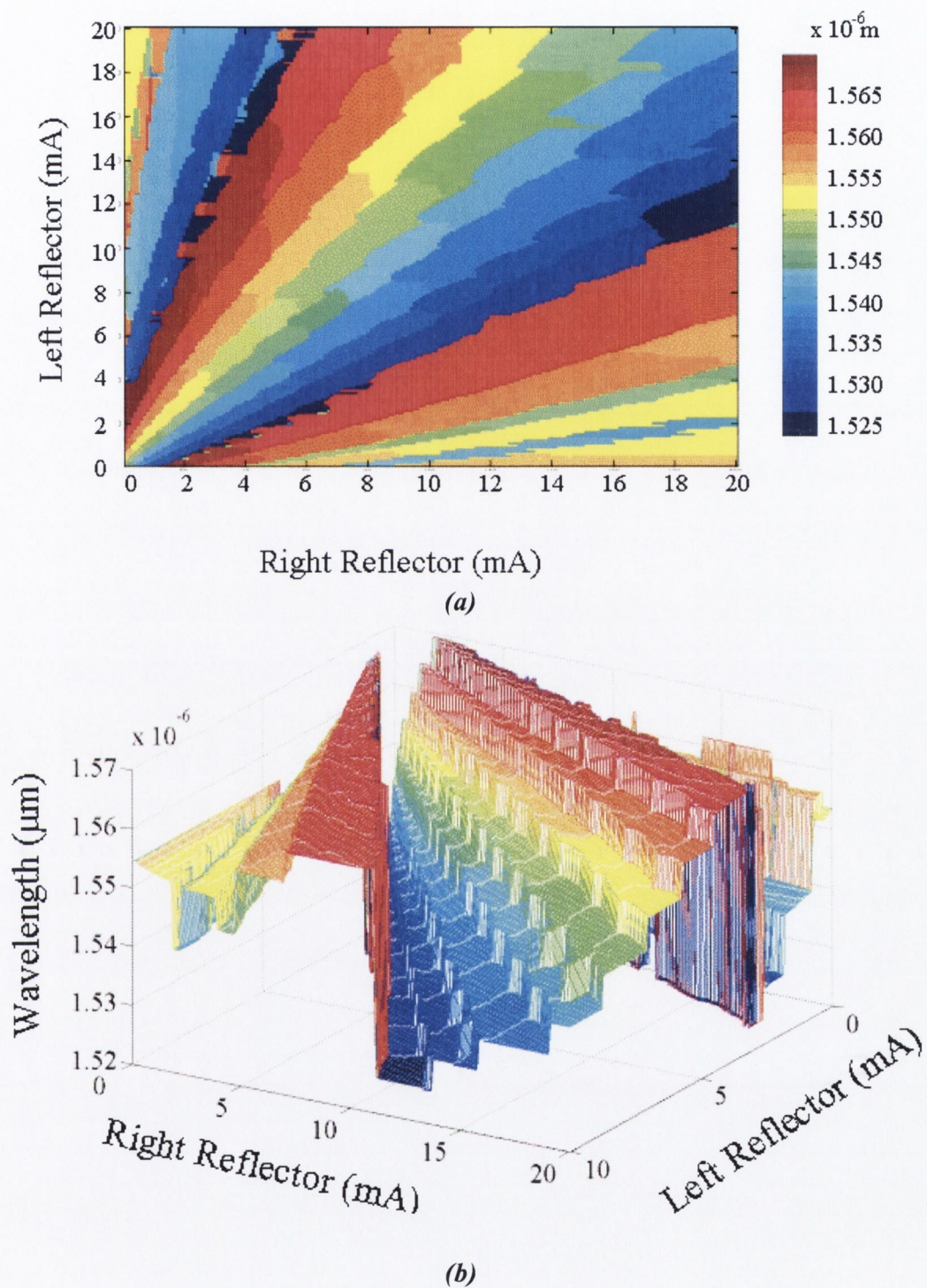
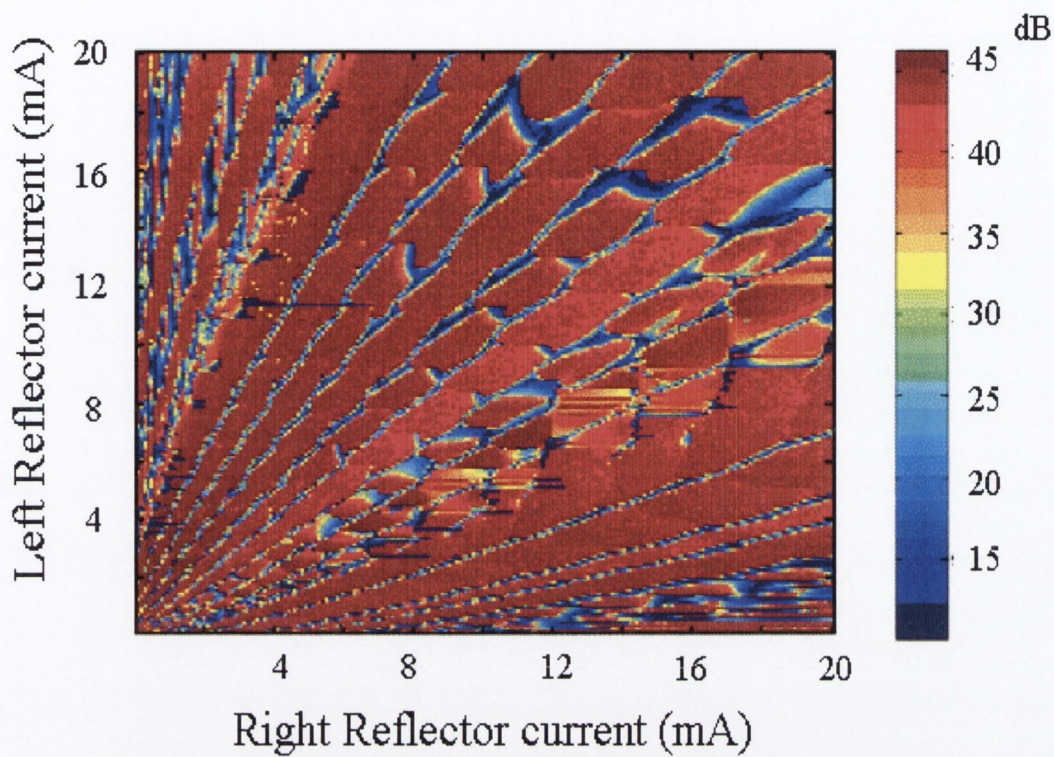
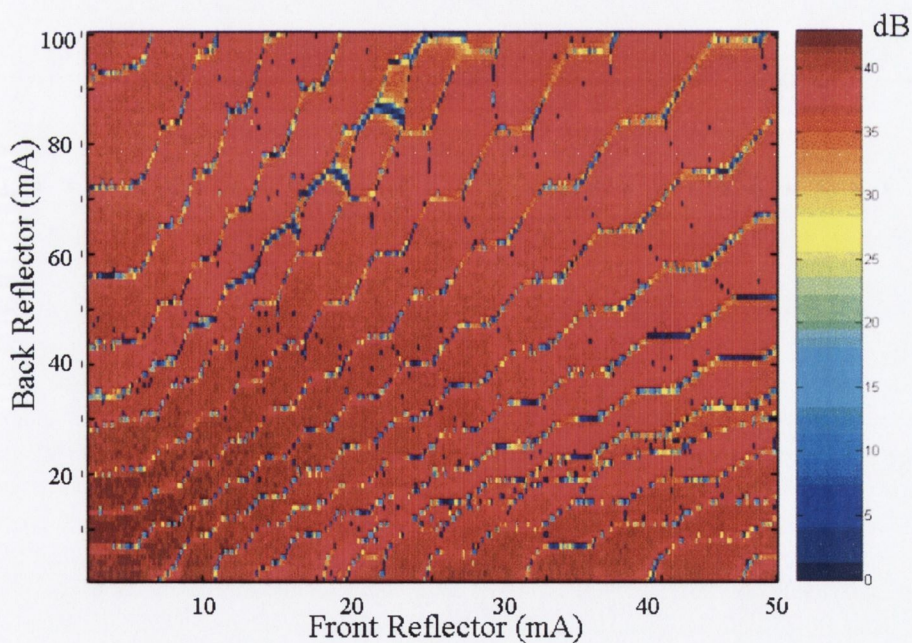


**Figure 6.3** (a) Emission wavelength of the MG-Y laser as a function of the left and right tuning currents,  $I_L$  and  $I_R$ , at fixed phase current  $I_P = 0\text{mA}$  and active section current  $I_G = 150\text{mA}$ . (b) 3-d plot of figure 6.3(a), eight super-modes clearly seen.





(a)



(b)

**Figure 6.4** (a) Measured map of SMSR for the MG-Y laser as a function of the left and right tuning currents,  $I_L$  and  $I_R$ , at fixed phase current  $I_P = 0\text{mA}$  and active section current  $I_G = 150\text{mA}$ . (b) Measured map of SMSR for the SG-DBR laser as a function of the front and back tuning currents,  $I_F$  and  $I_B$ , at fixed phase current  $I_P = 0\text{mA}$  and active section current  $I_G = 120\text{mA}$ .



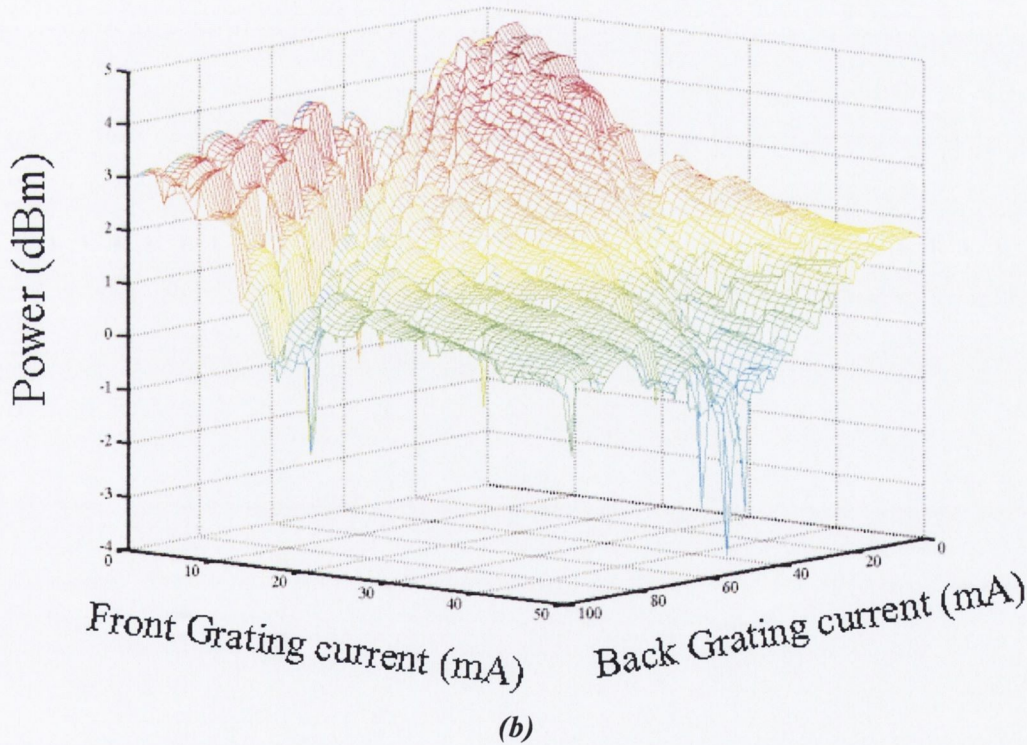
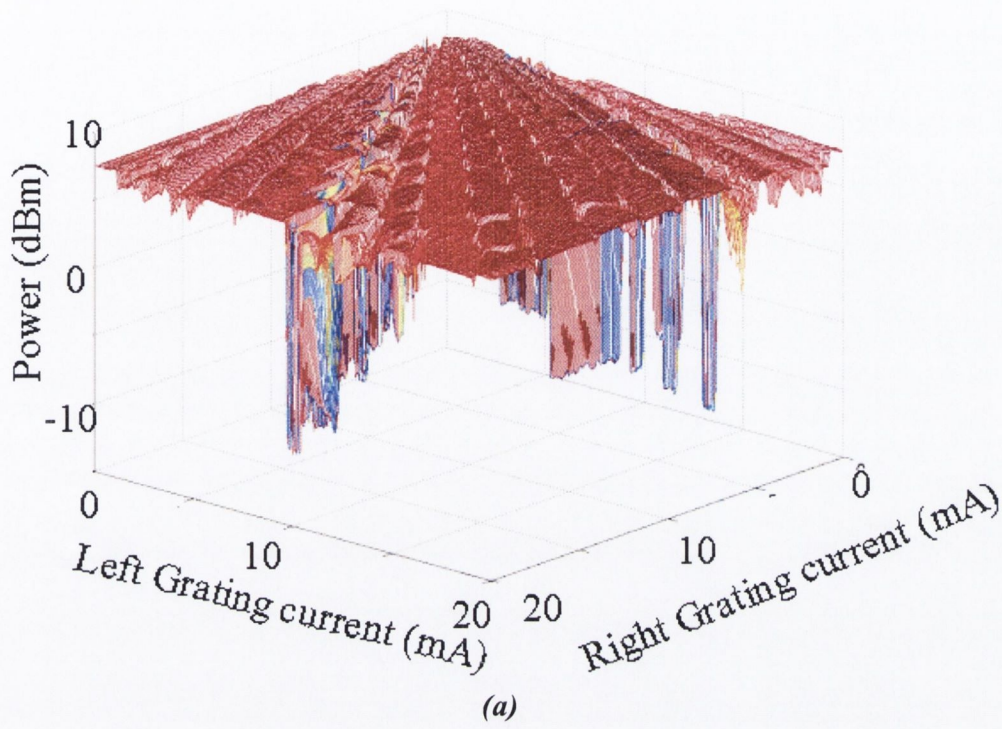


**Figure 6.5** (a) Measured contour map of output power for the MG-Y laser as a function of the left and right tuning currents,  $I_L$  and  $I_R$ , at fixed phase current  $I_P = 0\text{mA}$  and active section current  $I_G = 150\text{mA}$ . (b) Measured contour map of output power for the SG-DBR as a function of the front and back tuning currents,  $I_F$  and  $I_B$ , at fixed phase current  $I_P = 0\text{mA}$  and active section current  $I_G = 120\text{mA}$ .



### 6.2.1 Characterisation methods to generate a frequency look-up tables

In order to tune the widely tuneable laser to a particular wavelength with a certain output power, four control currents have to be adjusted. To make matters worse, any change in a single control current will affect both the wavelength and the power. From a gas sensing point of view it should be possible to tune the laser continuously across a number of gas absorption lines using simple digital commands. For this, a look-up table of operating points is used. The generated look-up tables should naturally yield high wavelength accuracy, high SMSR and preferably a high degree of power uniformity across the tuning range. The aim of this section is to find the correct values of current to inject into each section to tune the emission wavelength quasi-continuously across the extended wavelength tuning range of the devices.

To accomplish this a best-fit line to achieve optimum laser performance is chosen on the basis that the distance to both super-mode jumps is maximised so that mode stability is optimised, as illustrated in Fig. 6.6.

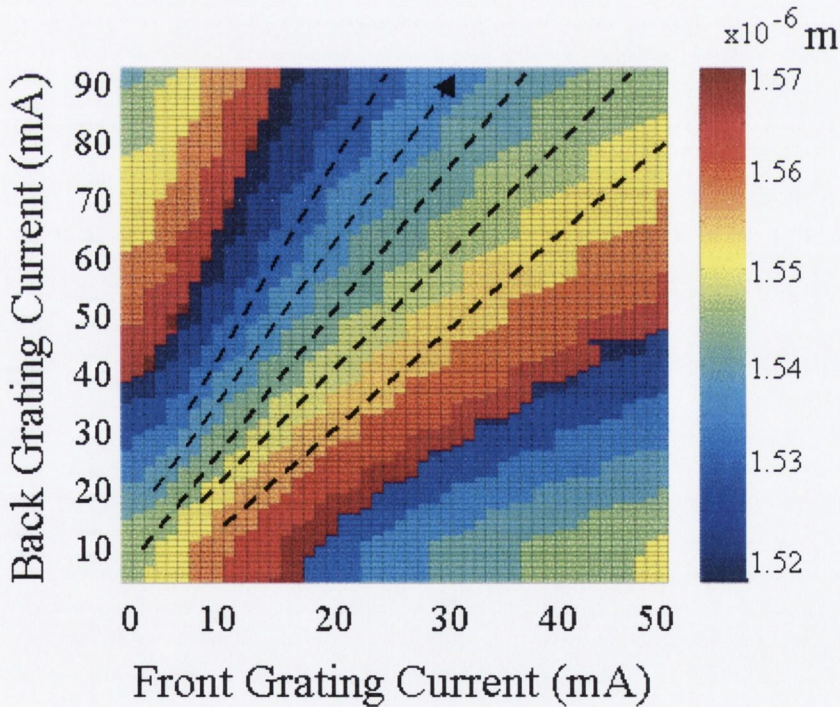


**Figure. 6.6** Measured contour map of the emission wavelength of SG-DBR laser as a function of front and back reflector currents. The dashed lines indicate the  $(I_F, I_B)$ -pairs that represents the best-fit line chosen on the basis that the distance to both super-mode jumps is maximised.



The dashed lines shown in Fig 6.6 clearly follow tracks along the wavelength contour that are situated approximately half-way between the super-modes jumps, indicating that a pair of reflectivity peaks remains reasonably well aligned. Fig 6.7 plots the wavelength as a function of  $(I_F, I_B)$ -pairs along the trace indicated by the arrow in Fig 6.6.

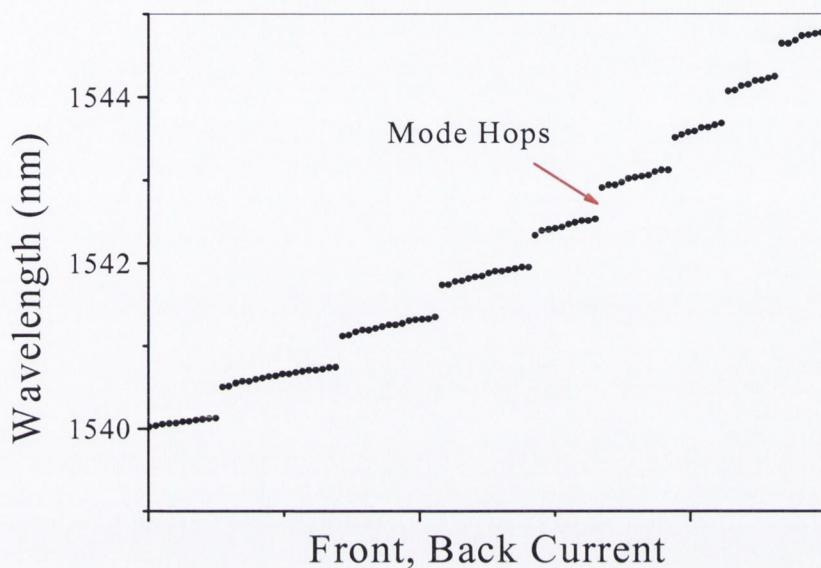


**Figure 6.7** Measured wavelength as a function of  $I_F, I_B$  along the trace indicated by the arrow in Fig 6.6.

When the wavelength of minimal round trip loss is tuned without adjusting the roundtrip phase, the emission wavelength jumps to an adjacent longitudinal mode i.e. when the adjacent mode experiences a lower loss (discontinuous tuning). Fig. 6.8 plots the wavelength as a function of  $I_F, I_B$  for two different values of the phase current to illustrate how to access the wavelengths between the mode hop in Fig. 6.7, by adjustment of the phase section current. Therefore, in order to get mode-hop-free tuning across the super-mode, the front and back grating currents have to be characterized as a function of phase current. The results of which are shown in Fig 6.9, which shows the wavelength as a function of the phase current and linked front and back grating current for one super-mode of the SG-DBR.

Again a number of plateaux are obtained, which now however correspond to individual longitudinal modes. The tuning traces are again located roughly halfway between two

longitudinal mode hops, so these operation points yield a high SMSR. In order to calculate a look-up table covering the full tuning range of the laser, this has to be repeated for each of the  $I_B$ ,  $I_F$  tracks in Fig 6.6.

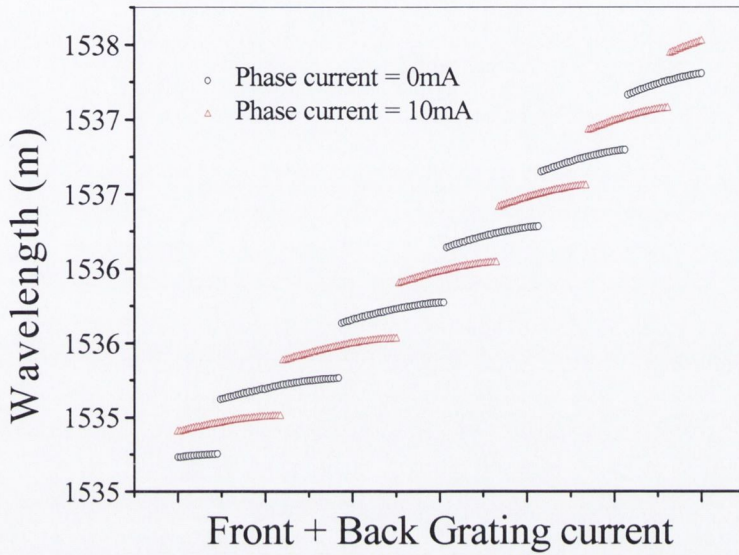


**Figure 6.8** Measured emission wavelength as a function of  $I_F$ ,  $I_B$  as a function of phase section current.

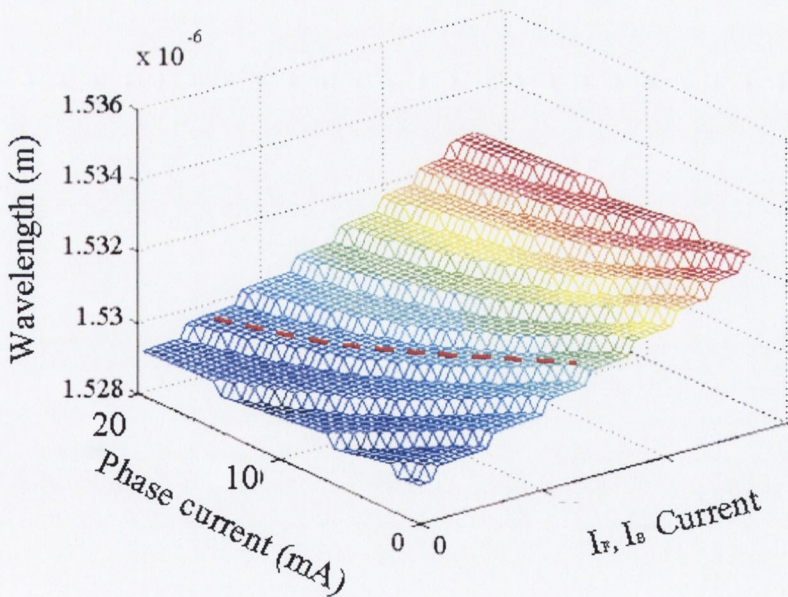


**Figure 6.9** Measured emission wavelength as a function of  $I_F$ ,  $I_B$  as a function of phase section current. The dashed line illustrates the  $(I_L, I_R)$ -pairs that represent the best-fit line chosen on the basis that the distance to both longitudinal mode jumps is maximised.

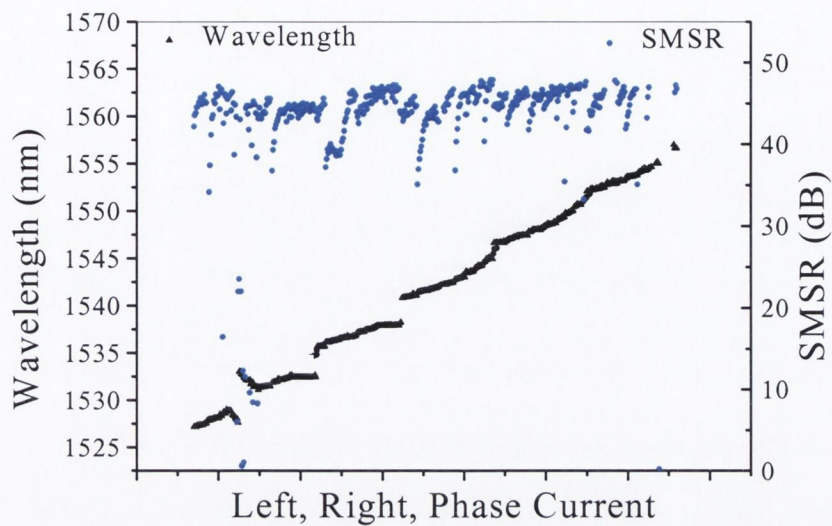


In summary the procedure used to generate the wavelength look-up tables for the SG-DBR consists of the following steps:

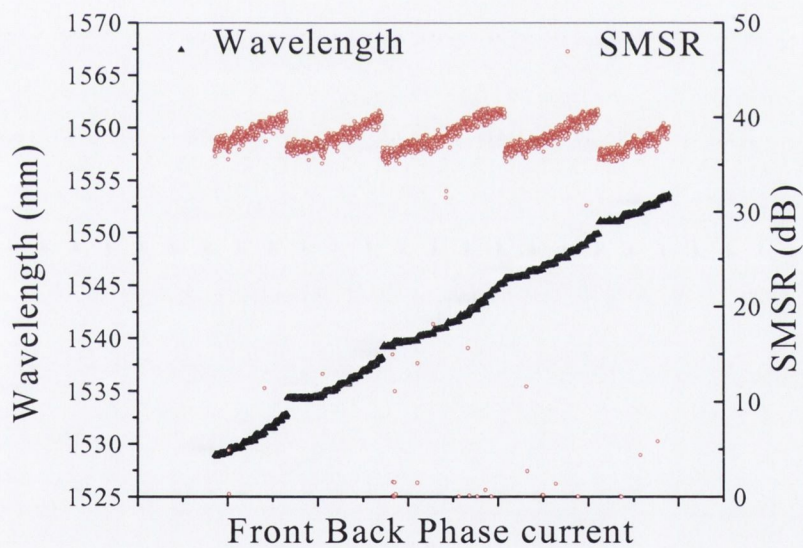
- ❖ Measure the wavelength on a two-dimensional grid of front and rear reflector currents. Phase and active section currents are kept at a constant value.
- ❖ Calculate  $(I_F, I_B)$ -pairs for the best-fit line chosen on the basis that the distance to both super-mode jumps is maximised. This is repeated for each super-mode.
- ❖ Generate a table of front and back reflector currents versus wavelength, which covers the desired tuning range. This table defines a number of tracks in the  $(I_F, I_B)$ -plane.
- ❖ The tracks in the  $(I_F, I_B)$ -plane for each super-mode are scanned as a function of the phase section current.
- ❖ Calculate  $(I_F, I_B \vee I_P)$ -pairs for the best-fit line chosen on the basis that the distance to both longitudinal-mode jumps is maximised. This is repeated for each super-mode.
- ❖ Finally a table of front, back and phase section currents versus wavelength, which covers the desired tuning range is generated.

The same procedure for generating the look-up table is applied to the MG-Y laser.

The look-up tables generated for the SG-DBR and MG-Y laser were then used to scan the emission wavelength across the extended tuning range of the lasers as a function of wavelength and SMSR as illustrated in Fig 6.10. For both lasers a SMSR between 35-45dB is obtained. Irregularities in the wavelength tuning are observed at certain regions. These observations indicate that mode hops occur and it is therefore difficult to tune the laser to these particular modes. On closer inspection of Fig. 6.10 it becomes apparent that in between these mode hops the laser tunes continuously and performs similarly to a single-section DFB.



(a)



(b)

**Figure 6.10** (a) Measured SMSR and emission wavelength for the look-up table generated for the MG-Y laser. (b) Measured SMSR and emission wavelength for the look-up table generated for the SG-DBR laser.



### 6.3 Application to gas sensing

The aim of this section is to detail the detection of multiple gases using widely tuneable laser diodes (SG-DBR, MG-Y) in a WMS detection scheme. Many gas species have overtone and combination bands in the near infrared region of the spectrum. Some of these gases with overtone/combination bands in the near infrared are  $\text{CH}_4$ ,  $\text{HF}$  [1],  $\text{HCN}$  [2],  $\text{NH}_3$  [3],  $\text{H}_2\text{S}$  [4],  $\text{CO}_2$  [5],  $\text{C}_2\text{H}_2$  [6], are shown in Fig. 6.11. All of these gases have been detected using single frequency telecom lasers, using WMS or FMS with harmonic detection. These high sensitivity detection techniques are particularly required in gas sensing applications at near infrared wavelengths since absorption band strengths are significantly less than in the fundamental absorption band regime. However, since the DFB laser diode has a narrow wavelength tuning range, only one gas can be targeted per device except where absorption features overlap [7]. This multiple device system quickly becomes complex and costly which is undesirable for implementation in a sensor for industrial applications as the number of gases to be detected increases [8]. Replacing all of these DFB lasers with a single widely tuneable laser device will reduce the complexity of the detection system. The chosen targeted gases,  $\text{C}_2\text{H}_2$ ,  $\text{HCN}$  and  $\text{NH}_3$  all have overtone and combination bands in the  $1.55\mu\text{m}$  region of the spectrum.

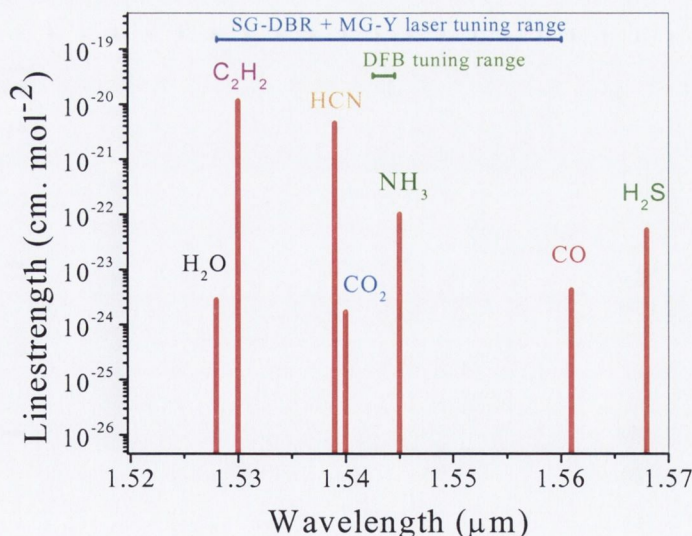


**Figure 6.11** Absorption lines of some environmentally important gases in relation to the tuning ranges of widely tuneable lasers



### 6.3.1 Experimental

A schematic of the experimental set-up for multi-gas detection is shown in Fig 6.12. The set-up includes a system for WMS with second harmonic detection and an etalon for spectral analysis of the widely tuneable laser output. The fibre-coupled output from the laser was split into five paths (referred to as first, second, third, fourth and fifth paths), using two 1x2 and one 1x3 fibre splitter. The first three paths were sent through the individual gas cells and onto InGaAs photodiodes. The gas cells with fibre input and output are 16.5cm in length and contain 50mbar HCN, 50mbar NH<sub>3</sub> and a combination cell containing 5mbar C<sub>2</sub>H<sub>2</sub> and 5mbar HCN, this calibrated gas mixture is thus convenient for demonstrating simultaneous detection of both HCN and C<sub>2</sub>H<sub>2</sub>. It was not possible to include NH<sub>3</sub> in this gas cell due to its polar nature, which makes it a very “sticky” molecule that adsorbs to most surfaces [3]. The fourth path was directed onto a detector to record the reference intensity. The fifth beam was collimated and sent through an etalon with a FSR of 18.61 pm and onto a InGaAs detector to monitor the laser-tuning rate. To reduce back reflections of the laser light from the fibre-to-air interface in the connectors, angle polished connectors (APC) that have a return loss of 60dB were used. Furthermore to reduce Fabry-Perot effects in the fibre-lens-gas cell interface, the cell was equipped with wedged (0.5 degree) glass windows. Also the cell windows are coated with a broadband anti-reflection coating.

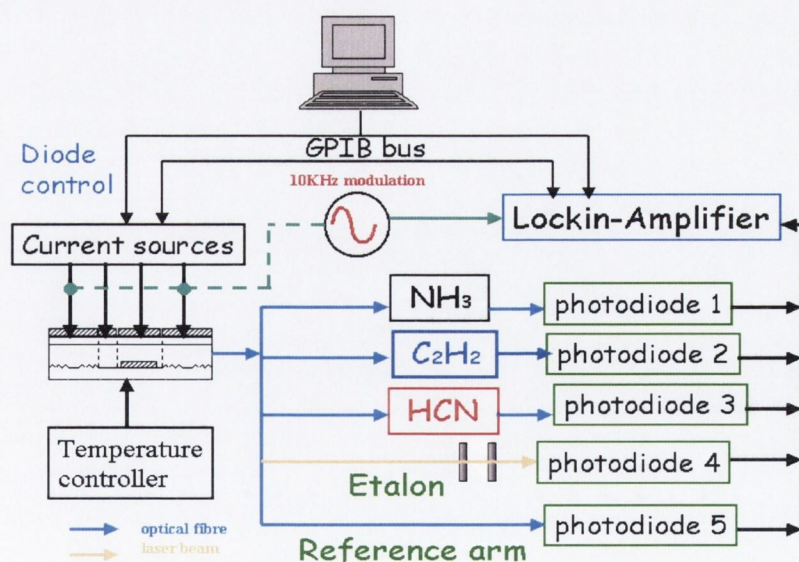


Figure 6.12 Experimental arrangement

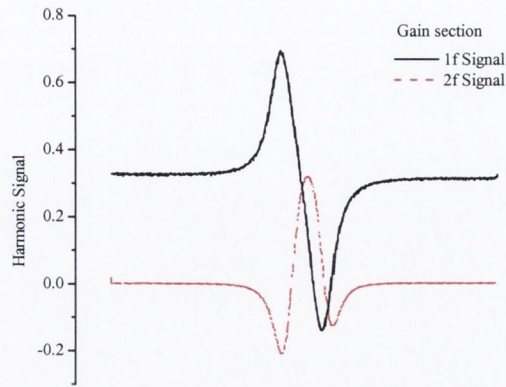


## 6.3.2 Results

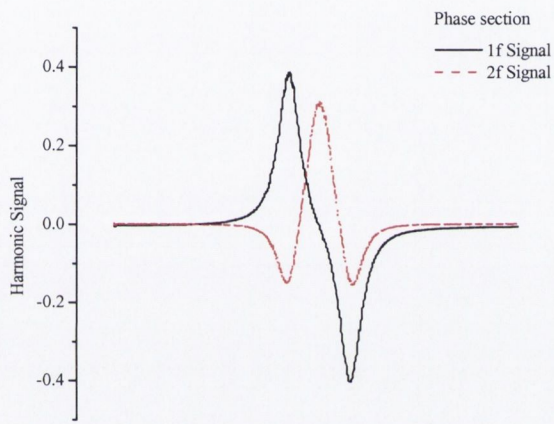
### 6.3.2.1 Grating Modulation

Modulation of the emission wavelength of widely tuneable lasers is normally achieved by modulating the current to the gain section but this is also accompanied by an unwanted residual amplitude modulation (RAM) in the laser output power. Since the harmonic signals are derivative-like in shape the RAM appears as an offset in the  $1f$  baseline and to a lesser extent in the  $2f$  baseline. One possibility for improving existing system configurations is to take advantage of the unique features of widely tuneable devices. For example, with the SG-DBR, modulating the passive front and back grating or the phase sections reduces the large amplitude modulation associated with modulating the gain section.

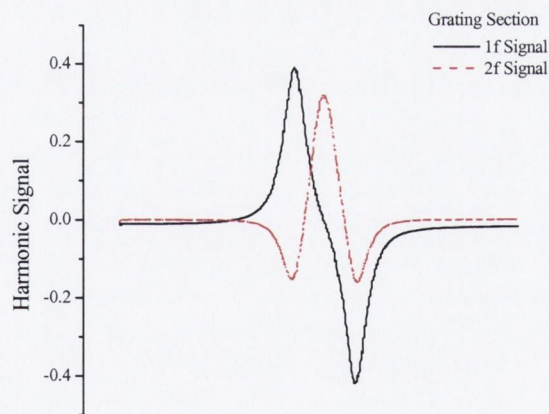
The three modulation schemes, gain, grating and phase modulation, were applied in turn to the SG-DBR and its emission wavelength was scanned across a HCN absorption line at 1529.5 nm. The three modulation techniques are compared and the results shown in Fig 6.13. As expected, a significant DC offset in the  $1f$  trace is observed for when gain modulation is used, the magnitude of this offset is proportional to the laser power incident on the detector. Hence detection at  $1f$  is sensitive to fluctuations in the laser power. In contrast, detection at  $2f$  produces negligible DC offset and further reduces the effect of laser power fluctuations, however an asymmetry in the  $2f$  lineshape is observed when gain modulation is used. It is clear from Fig 6.13 (b, c), that the offset due to the RAM is significantly reduced in  $1f$  harmonic detection, when grating and phase modulation is used, indicating the possibility for improved detection sensitivity. Table 6.1 summarises the results.



(a)



(b)



(c)

**Figure 6.13** Measured 1f, 2f absorption signal of HCN line at 1529.5 nm while modulating the (a) gain (b) phase (c) grating section of a SG-DBR.



<u>Modulation</u>	<u>Gain-section</u>	<u>Grating-section</u>	<u>Phase-section</u>
<i>1f baseline offset</i>	0.315	0.017	0.007
<i>2f baseline offset</i>	0.00095	0.00054	0.00002
<i>Spot noise</i>	0.007	0.0003	0.00026

**Table 6.1** Passive section modulation results for the SG-DBR.

When the passive sections are modulated, frequencies of about 200MHz [9] can be reached compared to at least one order of magnitude greater for the gain section. The reduction in the modulation frequency limit is caused by the longer recombination time in passive sections, compared with the gain section where the stimulated recombination reduces the recombination time. This lower modulation frequency restricts the grating modulation scheme to use in WMS systems, where modulation frequencies much lower than the absorption halfwidth of absorption lines are used. Further work is required to optimise the grating modulation technique hence modulation of the gain section was employed in this work.

### 6.3.2.2 Multiple-species gas sensing

The target gases HCN C<sub>2</sub>H<sub>2</sub> and NH<sub>3</sub> all have overlapping absorption bands within the tuning range of the lasers. The ability to selectively detect three gases with overlapping absorption bands by accurately tuning the emission wavelength of the SG-DBR and MG-Y laser to a position where individual absorption lines do not coincide is now demonstrated. To the best of our knowledge this is the first application of a MG-Y laser in a gas sensing application. The emission wavelength of the SG-DBR and MG-Y laser was tuned across the absorption bands of the three gases from 1529 to 1560nm using the look-up table generated in the previous section and the 2f outputs from the lockin amplifier and displayed in Fig 6.14 for the SG-DBR and Fig. 6.15 for the MG-Y laser respectively. The spectra shown in Fig 6.14 and Fig. 6.15 was not optimised for sensitivity but for selectivity ( $m < 2.2$ ) so as to resolve all the absorption lines as effectively as possible.

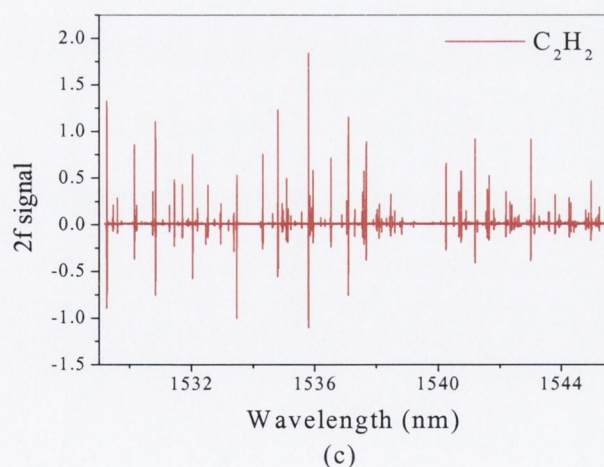
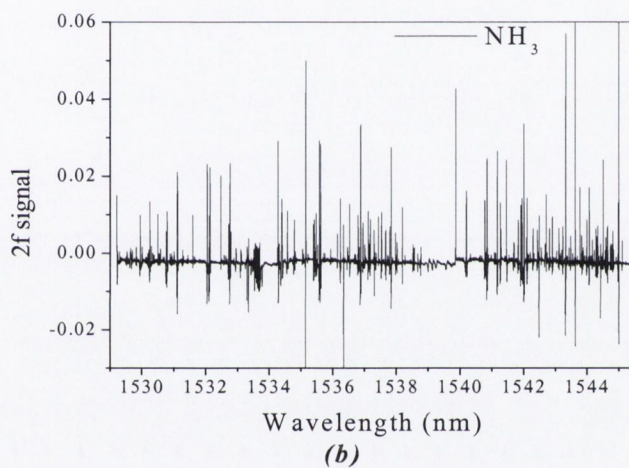
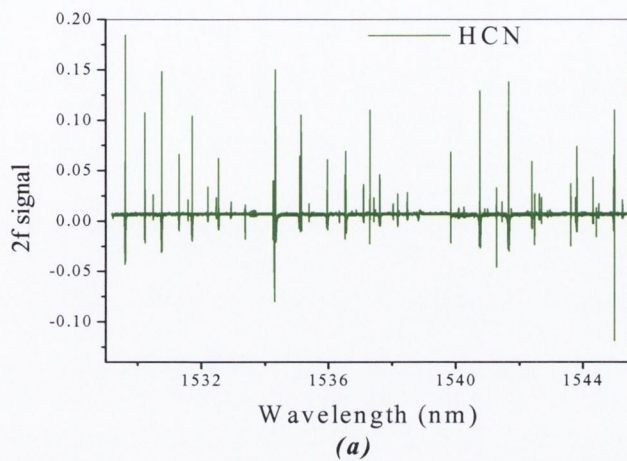
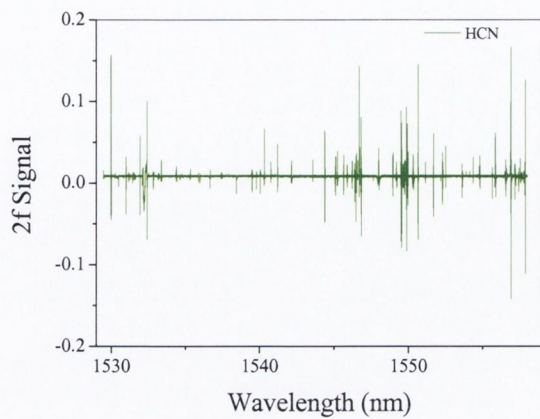
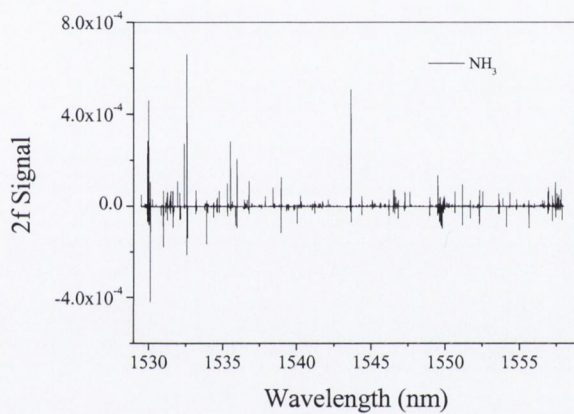


**Figure 6.14** Measured  $2f$  absorption spectra of (a) HCN (b)  $\text{NH}_3$  (c)  $\text{C}_2\text{H}_2$  and HCN when the emission wavelength of the SGDBR was swept from 1529–1545 nm.

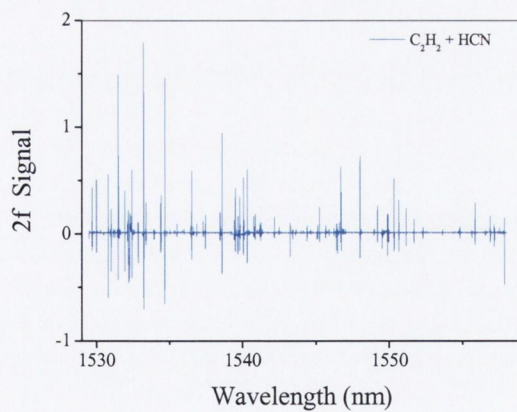




(a)



(b)



(c)

**Figure 6.15** Measured  $2f$  absorption spectra of (a) HCN (b)  $\text{NH}_3$  (c)  $\text{C}_2\text{H}_2$  and HCN when the emission wavelength of the MG-Y laser was swept from 1529–1559 nm.

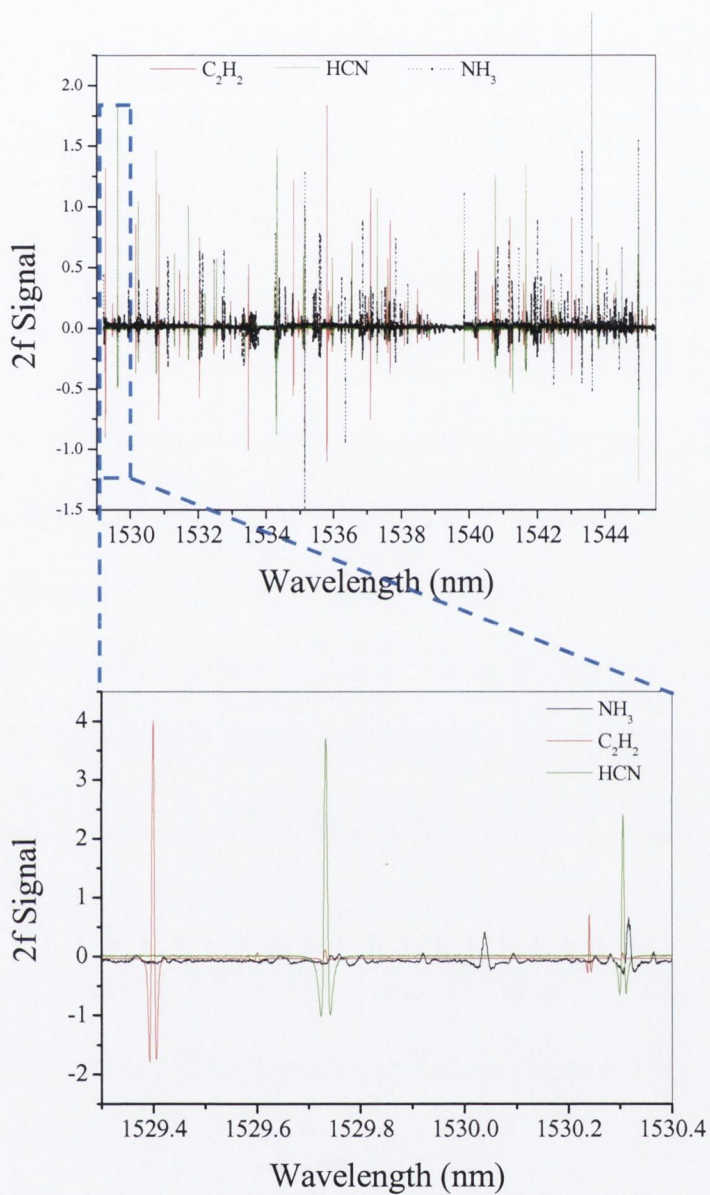


**Figure 6.16** High specificity multi-species gas sensing enabling detection of  $\text{NH}_3$ ,  $\text{C}_2\text{H}_2$  and  $\text{HCN}$  by tuning SG-DBR laser to regions where absorption lines due to individual gases are well resolved.



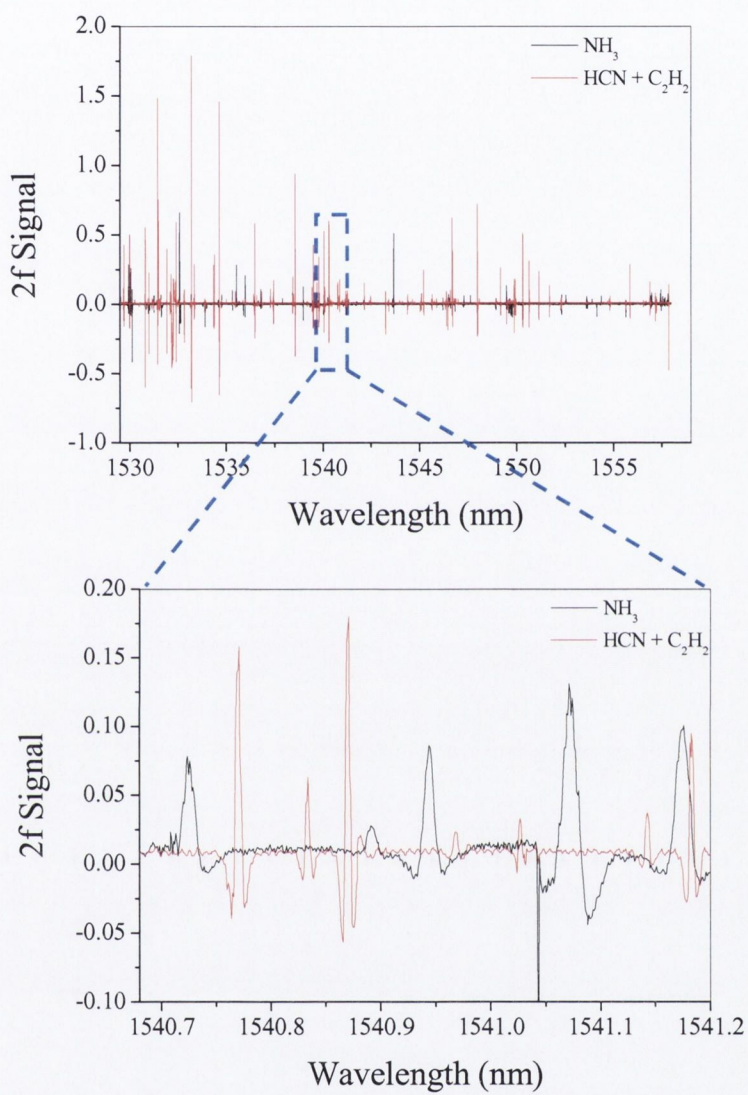


**Figure 6.17** High specificity multi-species gas sensing enabling detection of NH<sub>3</sub>, C<sub>2</sub>H<sub>2</sub> and HCN by tuning MG-Y laser to regions where absorption lines due to individual gases are well resolved.

Over limited tuning regions between mode-hops across the scan, the laser tunes continuously and performs similarly to single-section DFB laser diodes, so we expect detection limits to be similar to those reported in the previous chapter for the SGC-DFB. Fig 6.16 and Fig. 6.17 display regions where overlapping absorption lines do not coincide thus enabling multi-gas sensing. Once the regions where the spectra of the individual gas absorption lines do not coincide are identified, the emission wavelength of the laser can be switched to any number of lines where the peak height can determine the concentration. This is a powerful demonstration of high specificity gas sensing achievable using widely tuneable lasers by probing specific rotational features in the optical absorption spectrum of the target species. As can be seen in Fig 6.14, the three gases contain approximately 50 absorption lines each within the tuning range of the widely tuneable lasers. The choice of which line to use for each gas is an optimisation problem with compounding complexity as the number of target gases increases. Relevant parameters are absorption linestrengths, required sensitivity and laser tuning and modulation characteristics. Also a favourable line may be overlapping with a weaker absorption line of another gas. The approach to this problem was to develop an algorithm to identify gas lines and the particular tuning currents to tune the emission wavelength to each line so the laser can be switched easily and accurately to values that coincide with the unique absorption feature of several gases in a multi-gas environment. The gas absorption lines are identified and are absolute wavelength references that can be applied to applications in DWDM for monitoring the emission wavelength of the laser. A line identification technique and results are outlined in the next section.

## **6.4 Line Identification**

### **6.4.1 Introduction**

Tuneable lasers are important components for next generation dense wavelength division multiplexing (DWDM) fibre optic networks [10, 11]. The wide tuning range and ability for fast wavelength switching make the SG-DBR laser especially attractive for multi-channel WDM networks. The frequencies to be used in wavelength division multiplexing (WDM) systems have recently been standardised by the International



Telecommunications Union. A regularly spaced frequency grid, anchored at 193.1 THz (1555.52 nm), with a channel spacing of 50 GHz (0.4nm) or 100 GHz (0.8 nm), was specified . To keep up with capacity demands the number of channels will probably have to be increased even further, by reducing the channel spacing down to 25 GHz (0.2nm). To manage the channel wavelength of DWDM systems, wavelength-monitoring techniques such as the use of arrayed-waveguide grating [12], fiber grating [13], active-layer junction voltage detection [14], and etalons [15] have been reported. In addition to these techniques with their characteristic advantages and disadvantages, the use of multiple gas absorption lines for wavelength monitoring offers the highest degree of accuracy. The gas absorption lines have a typical FWHM of a few hundred MHz at low pressure, and their wavelength dependence on temperature is such that, active temperature control and stabilisation, which is necessary for other methods, is not required.

The use of reference gases to provide unique wavelength identifiers to characterise the device and provide monitoring of the lasing wavelength have been investigated. We have shown that the tuning behaviour of the SG-DBR can be characterised using a combination of reference gases (acetylene, hydrogen cyanide, ammonia) in a cost effective manner.

#### **6.4.2 Identification of Gas Lines**

The recorded spectroscopic data files that include the 2f absorption scans from the three gas cells, reference intensity, and etalon traces were automatically processed with a LabVIEW programmed algorithm to identify the gas lines. This procedure is capable of recognising the mode hop free regions and identifies the gas absorption lines located in these continuous tuning regions. Etalon transmission peaks are used to get accurate wavelength differences  $\Delta\lambda$  between gas absorption lines. These wavelength differences are then compared with a database of absorption lines [16, 17], to identify the absorption lines and give an absolute wavelength measurement. This is work in progress but the general principle of operation is outlined with some promising initial results.



The line-identification program works by splitting the wavelength scans into segments of continuous tuning regions. This is achieved by monitoring the reference intensity and mode-hops are identified by jumps in the power as illustrated in Fig 6.18.

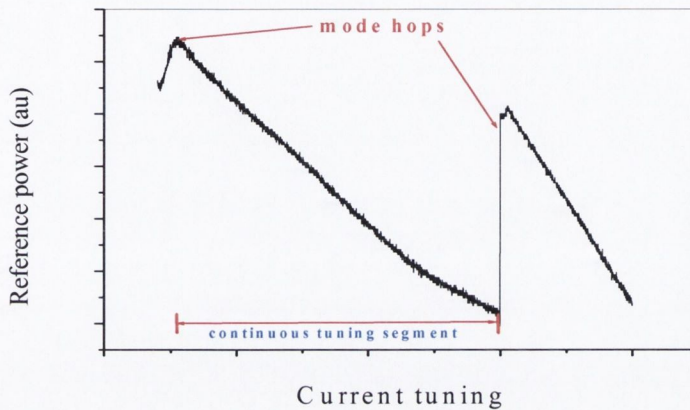


**Figure 6.18** Reference power used to identify mode hops

To calibrate the tuning rate within the segment and measure the separations between the gas absorption lines an etalon with a FSR of 18.61 pm was used. To extract this parameter the number and temporal positions of the maxima on the etalon transmission signal are determined. This is done with a LabVIEW program, which counts the maxima by detecting the peaks as illustrated in Fig 6.19. The dynamic tuning curve of the laser can be depicted by plotting the time at each zero crossing versus fringe mode number multiplied by the FSR of the etalon. Finally a fourth order polynomial was fitted to the tuning curve.

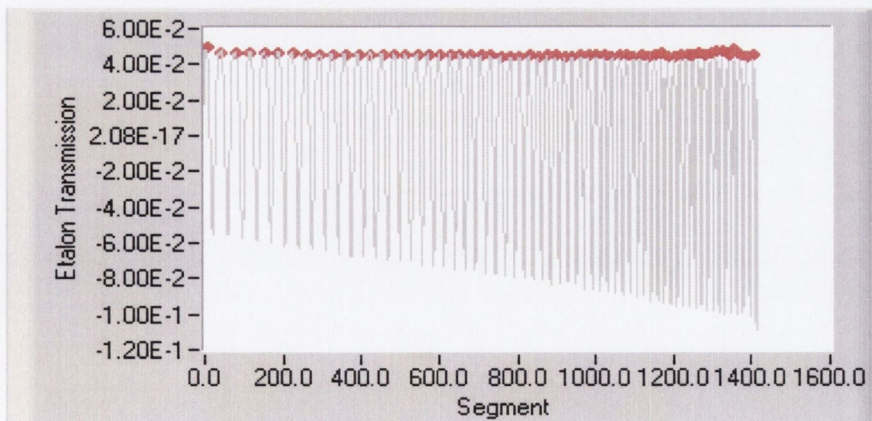
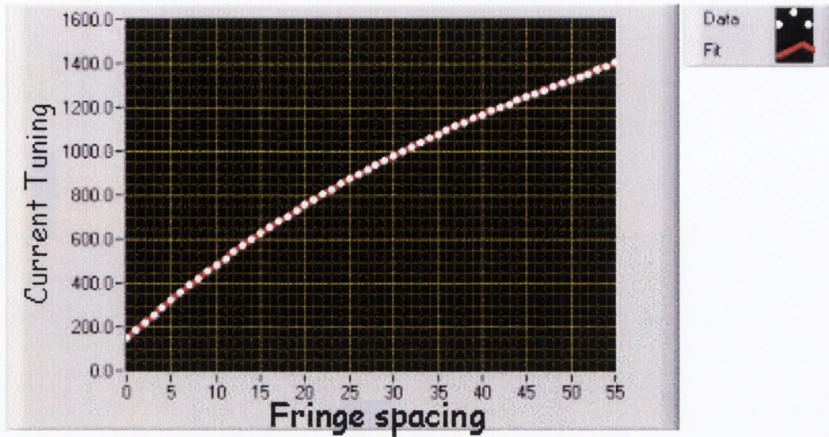
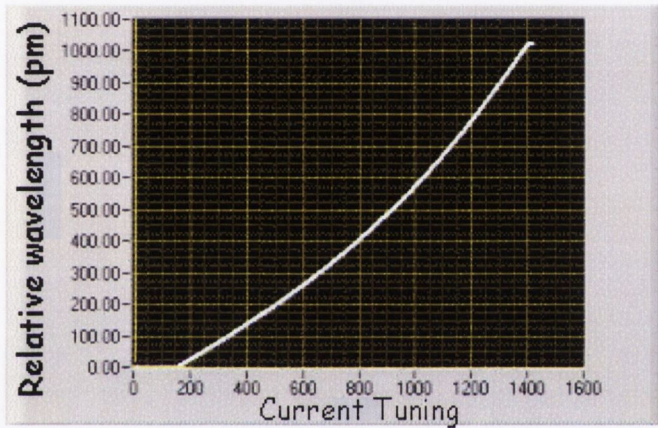


**Figure 6.19 (a)** Etalon transmission signal, red dots indicate positions of the maxima on the etalon





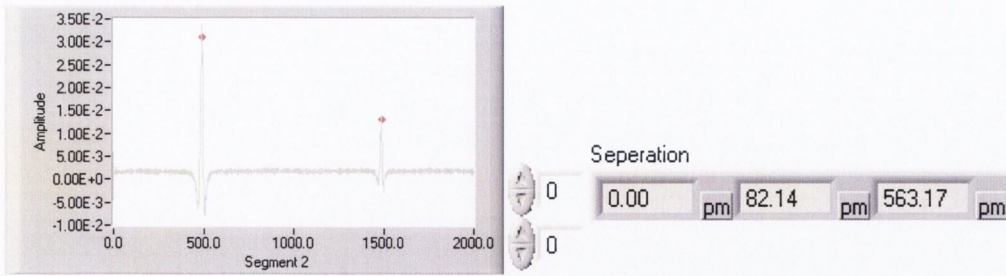
(a)



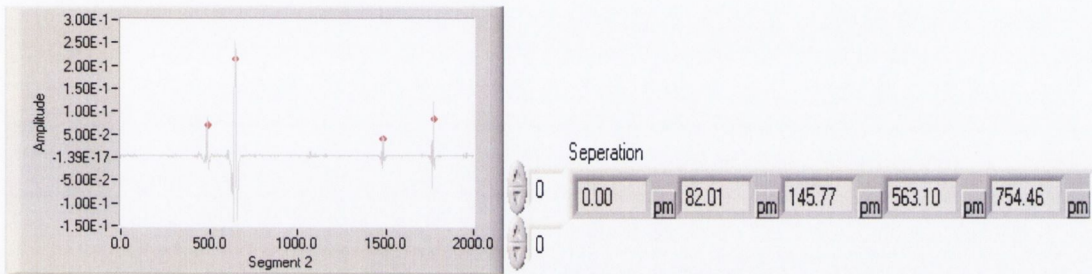
(b)

**Figure 6.20** (a) Fringe spacing versus tuning fitted with a 4<sup>th</sup> order polynomial to extract relative wavelength tuning (b) Etalon fringe spacing multiplied by FSR gives relative tuning curve

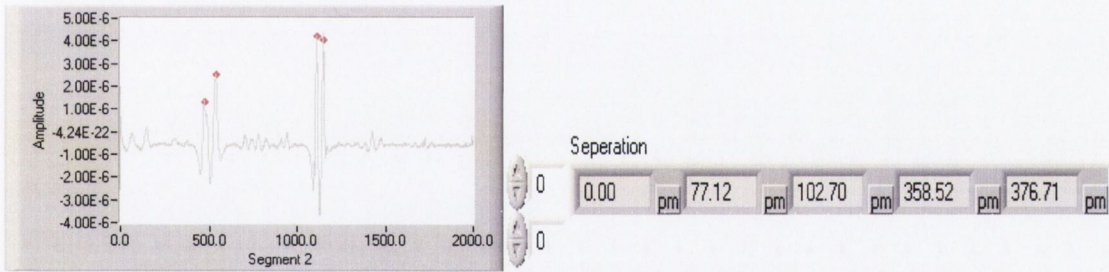
The segments of continuous tuning are then sent through the line-identification algorithm which cross-correlates the 2f scans with a 2f profile to identify the gas line. A peak search algorithm is then used to find the positions and heights of the gas lines. An example of this is illustrated in Fig 6.21 for one segment. The three traces represent the 2f absorption signals from the three different gas cells and the red dot indicates that a gas absorption line has been successfully identified. The separation from the start of the segment to the gas lines, which was calculated from the etalon is displayed in the table.



(a)



(b)



(c)

**Figure 6.21** Plot of line identification for a segment red dots indicate line identified. (a) HCN (b)  $C_2H_2$  and HCN (c)  $NH_3$ . Table represents separation from the start of the segment to the gas lines, which was calculated from the etalon



To obtain an absolute wavelength reference for the starting point in each segment the separations calculated above are correlated with the separations from the gas database as follows,

- The segment with measured separations for one of the gas cells is sent into the algorithm and the start of the segment is referenced to the first gas line in the database.
- The separations between the measured gas lines are then compared to the separations in the database from this first line. A correlation value is obtained for this line depending on the accuracy of the match.
- This procedure is repeated for every gas line in the database building a correlation spectrum.
- The same procedure is applied to the line separations associated with the other gas cells. The correlation spectra from the individual gas cells are multiplied together to give an overall correlation spectrum for the possible start wavelength of the segment.

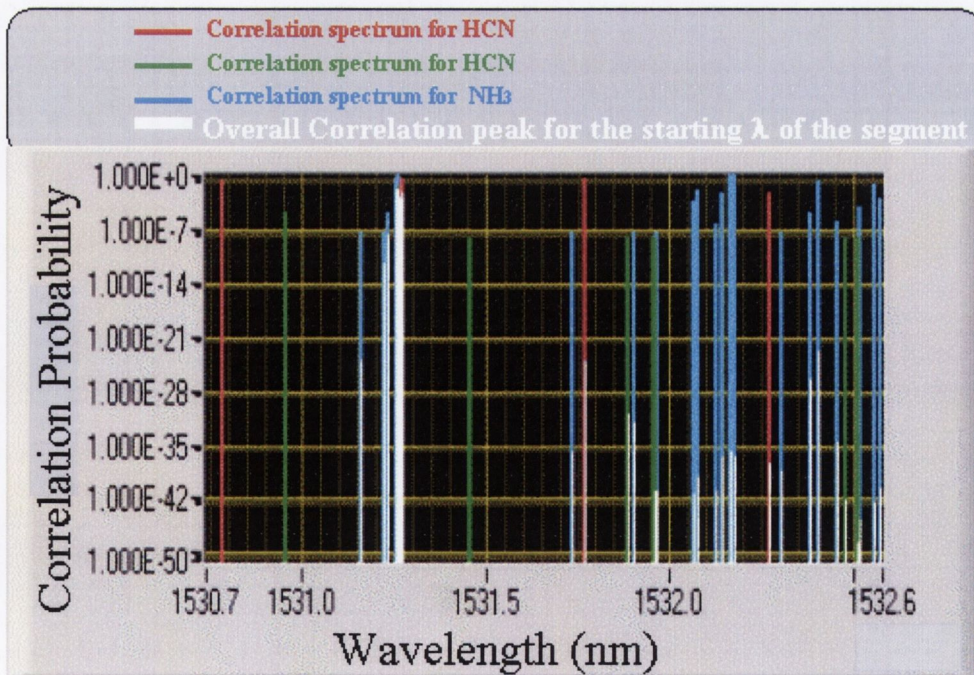


*Figure 6.22 Correlation spectrum for individual gas cells and overall correlation peak.*



Possible Matches	1	2
Probability	6.67E-17	8.29E-19
Computed Wavelength (nm)	1531.561	1529.178

2<sup>nd</sup> place match probability reasonable

**Segment 1 Measured starting  $\lambda$  1529.2 nm**

Possible Matches	1	2
Probability	4.09E-4	2.73E-4
Computed Wavelength (nm)	1530.227	1530.222

1<sup>st</sup> place match good correlation probability

**Segment 2 Measured starting  $\lambda$  1530.5 nm**

Possible Matches	1	2
Probability	1.81E-2	1.08E-2
Computed Wavelength (nm)	1531.264	1531.254

1<sup>st</sup> place match good correlation probability

**Segment 3 Measured starting  $\lambda$  1531.58 nm**

Possible Matches	1	2
Probability	9.30E-60	0.00E+0
Computed Wavelength (nm)	1528.769	1561.749

No match due to mode-hop  
Very low coefficient

**Segment 4 Measured starting  $\lambda$  1532.47 nm**

Possible Matches	1	2
Probability	3.45E-24	1.97E-26
Computed wavelength (nm)	1534.451	1534.401

1<sup>st</sup> place match reasonable probability

**Segment 5 Measured starting  $\lambda$  1534.25 nm**

**Table 6.2** Results from line identification program. Correlation probabilities not normalised to 1.



The results which demonstrate how the algorithm performs on five segments are presented. The SG-DBR emission wavelength for the start of each segment was measured with a wavelength meter (resolution 0.01 nm), for comparison with results from the line identification program. The results for five segments are displayed in table 6.2. Starting wavelength for segment one was measured to be 1529.2 nm and the results from the program indicate that the highest probability of a match is at 1531.56 nm, the second highest probability of 1529.178 nm which is the correct value. The results for segments two, three and five agree well with the measured starting wavelengths, the positions of the lines in these segments were confirmed by manually going through the database comparing relative wavelengths and amplitudes of the measured lines to identify the gas absorption lines. Segment four gives an incorrect value of 1528.769 nm for the starting wavelength compared to 1532.47 nm measured value but this is also confirmed by the low probability  $9.30E-60$  of this line being a match.

A simple and straightforward method using multiple reference gases for wavelength characterisation and monitoring of a SG-DBR has been outlined. This method requires measurements of the gas absorption lines, an etalon trace and comparing the wavelength separations between gas absorption lines and the corresponding wavelength separations from a database to determine the emission wavelength of the SG-DBR. This procedure was not optimised but the general principle of operation is outlined with some initial results. A topic for future research is development of the algorithm to include the relative amplitude variations to increase the accuracy in finding the starting segment wavelengths. This method has the potential of offering a cost effective technique for characterising the spectral emission of the SG-DBR without the need for expensive and time-consuming wavelength meter.



## 6.5 Conclusion

The optical characteristics of the MG-Y and SG-DBR have been investigated, tuning ranges of 50 nm have been achieved and look-up tables which yield high wavelength accuracy and high SMSR across the tuning range have been generated. For both lasers a SMSR between 35-45dB is obtained. Irregularities in the wavelength tuning are observed at certain regions. These observations indicate that mode hops occur and it is therefore difficult to tune the laser to these particular modes. In between these mode hops the laser tunes continuously and performs similar to single-section DFB. Simultaneous multi-species gas sensing of hydrogen cyanide, acetylene and ammonia with a SG-DBR and MG-Y laser to selectively detect three gases with overlapping absorption bands. This measurement is among the first demonstration of simultaneous detection of multiple species using a multi-section, injection current tuned MG-Y laser and is a promising demonstration of the possible usefulness of these lasers. This was the first batch of MG-Y lasers manufactured within the EU-funded project NEWTON, and it can be expected that their operational characteristics will improve with time as manufacturing techniques mature.

A simple and straightforward method using multiple reference gases for wavelength characterisation and monitoring of a SG-DBR has been demonstrated. This method requires measurements of the gas absorption lines and an etalon trace and comparison of the separations between gas absorption lines and the corresponding separations from a database (HITRAN) to determine the emission wavelength of the SG-DBR. Further work is required to optimise the line identification algorithm by including the relative amplitude separations, as linestrength information was unavailable for the acetylene molecule in the 1.5 $\mu$ m region. This extra information will greatly improve the segment identification.



## 6.6 References

- [1] S.-I. Chou, D. S. Baer, and R. K. Hanson, "Spectral Intensity and Lineshape Measurements in the First Overtone Band of HF Using Tunable Diode Lasers," *Journal of Molecular Spectroscopy*, vol. 195, pp. 123-131, 1999.
- [2] H. Sasada, "1.5 $\mu\text{m}$  DFB semiconductor laser spectroscopy of HCN," *Chemical Physics*, vol. 88, 1988.
- [3] M. E. Webber, D. S. Baer, and R. K. Hanson, "Ammonia monitoring near 1.5 $\mu\text{m}$  with diode-laser absorption sensors," *Applied Optics*, vol. 40, pp. 2031-2042, 2001.
- [4] V. Weldon, K. Boylan, B. Corbett, D. McDonald, and J. O'Gorman, "A novel single frequency stabilized Fabry-Perot laser diode at 1590 nm for gas sensing," *Spectrochimica Acta Part a-Molecular and Biomolecular Spectroscopy*, vol. 58, pp. 2433-2438, 2002.
- [5] M. E. Webber, S. Kim, S. T. Sanders, D. S. Baer, R. K. Hanson, and Y. Ikeda, "In situ combustion measurements of CO<sub>2</sub> by use of a distributed-feedback diode-laser sensor near 2.0  $\mu\text{m}$ ," *Applied Optics*, vol. 40, pp. 821-828, 2001.
- [6] H. Tai, K. Yamamoto, M. Uchida, S. Osawa, and K. Uehara, "Long-distance simultaneous detection of methane and acetylene by using diode lasers coupled with optical fibers," *Photonics Technology Letters, IEEE*, vol. 4, pp. 804-807, 1992.

- [7] V. Weldon, P. Phelan, and J. Hegarty, "Methane and carbon dioxide sensing using a DFB laser diode operating at 1.64  $\mu\text{m}$ ," *Electronics Letters*, vol. 29, pp. 560-561, 1993.
- [8] D. S. Baer, R. K. Hanson, M. E. Newfield, and N. Gopaul, "Multiplexed Diode-Laser Sensor System for Simultaneous  $\text{H}_2\text{O}$ ,  $\text{O}_2$ , and Temperature-Measurements," *Optics Letters*, vol. 19, pp. 1900-1902, 1994.
- [9] A. P. Larson, L. Sandstrom, S. Hojer, H. Ahlberg, and B. Broberg, "Evaluation of distributed Bragg reflector lasers for high-sensitivity near-infrared gas analysis," *Optical Engineering*, vol. 36, pp. 117-123, 1997.
- [10] L. A. Coldren, G. A. Fish, Y. Akulova, J. S. Barton, L. Johansson, and C. W. Coldren, "Tunable semiconductor lasers: a tutorial," *Lightwave Technology, Journal of*, vol. 22, pp. 193-202, 2004.
- [11] G. Sarlet, G. Morthier, and R. Baets, "Wavelength and mode stabilization of widely tunable SG-DBR and SSG-DBR lasers," *Photonics Technology Letters, IEEE*, vol. 11, pp. 1351-1353, 1999.
- [12] M. Teshima, M. Koga, and K.-I. Sato, "Performance of multiwavelength simultaneous monitoring circuit employing arrayed-waveguide grating," *Lightwave Technology, Journal of*, vol. 14, pp. 2277-2285, 1996.
- [13] Y. Park, S.-T. Lee, and C.-J. Chae, "A novel wavelength stabilization scheme using a fiber grating for WDM transmission," *Photonics Technology Letters, IEEE*, vol. 10, pp. 1446-1448, 1998.



- [14] S.-L. Lee, Y.-Y. Pisu, and C.-T. Pien, "High-resolution wavelength monitoring using differential/ratio detection of junction voltage across a diode laser," *Photonics Technology Letters, IEEE*, vol. 13, pp. 872-874, 2001.
- [15] H. Nasu, T. Mukaihara, T. Takagi, M. Oike, T. Nomura, and A. Kasukawa, "25-GHz-spacing wavelength-monitor integrated DFB laser module for DWDM applications," *Photonics Technology Letters, IEEE*, vol. 15, pp. 293-295, 2003.
- [16] L. S. Rothman, C. P. Rinsland, A. Goldman, S. T. Massie, D. P. Edwards, J. M. Flaud, A. Perrin, C. Camy-Peyret, V. Dana, J. Y. Mandin, J. Schroeder, A. McCann, R. R. Gamache, R. B. Wattson, K. Yoshino, K. V. Chance, K. W. Jucks, L. R. Brown, V. Nemtchinov, and P. Varanasi, "The HITRAN molecular spectroscopic database and HAWKS (HITRAN Atmospheric Workstation): 1996 edition," *Journal of Quantitative Spectroscopy & Radiative Transfer*, vol. 60, pp. 665-710, 1998.
- [17] N. Jacquinet-Husson, E. Arie, J. Ballard, A. Barbe, G. Bjoraker, B. Bonnet, L. R. Brown, C. Camy-Peyret, J. P. Champion, A. Chedin, A. Chursin, C. Clerbaux, G. Duxbury, J. M. Flaud, N. Fourrie, A. Fayt, G. Graner, R. Gamache, A. Goldman, V. Golovko, G. Guelachvili, J. M. Hartmann, J. C. Hilico, J. Hillman, G. Lefevre, E. Lellouch, S. N. Mikhailenko, O. V. Naumenko, V. Nemtchinov, D. A. Newnham, A. Nikitin, J. Orphal, A. Perrin, D. C. Reuter, C. P. Rinsland, L. Rosenmann, L. S. Rothman, N. A. Scott, J. Selby, L. N. Sinitsa, J. M. Sirota, A. M. Smith, K. M. Smith, V. G. Tyuterev, R. H. Tipping, S. Urban, P. Varanasi, and M. Weber, "The 1997 spectroscopic GEISA databank," *Journal of Quantitative Spectroscopy & Radiative Transfer*, vol. 62, pp. 205-254, 1999.

# Chapter 7

## Conclusions

### 7.1 Overview

Research on tuneable diode laser absorption spectroscopy (TDLAS) already has a fairly long history (more than 30 years) [1]. However until recently widely tuneable laser diodes were considered unsuitable for applications in TDLAS. They were deemed too complex to control and their output characteristics would never live up to the stringent requirements posed for industry applications. About three to four years ago, telecommunication applications began to drive significant investment into the area of widely tuneable lasers, to support the need for dynamic networks and wavelength reconfigurability in WDM systems [2]. Nowadays tuneable laser diodes are considered to be essential components in WDM for the next generation of optical communication systems. TDLAS applications have benefited enormously from the extensive R&D performed in the area of tuneable laser diode development. Recent research results, among which the results reported in this thesis have shown tuneable lasers to have reached specification parity with DFBs, and hence, becoming attractive components in TDLAS applications. The primary aim of this project was to advance the strategic capability required to allow development of TDLAS multi-species gas detection systems using widely tuneable laser diodes. Such a detection systems will enable the real time simultaneous monitoring of multi-gas species, a considerable advantage over the existing arrangement where monitoring is limited to a single gas. In chapter 4, the effects of spectral line shift, line strength and  $N_2$  broadening on the water vapour line at  $1.3928\mu\text{m}$  for temperatures between 300K-1100K, and their impact on the accuracy of optical absorption based gas sensing has been investigated. Significant spectral parameters ( $S$ ,  $2\gamma$ ,  $N$ ,  $\delta$ ) for this absorption line were measured



and were in good agreement with values obtained in the literature. The high temperature gas cell performed well and is a simple and inexpensive apparatus enabling spectral characteristic measurements at elevated temperatures.

Chapter 5 details the first application of a SGC DFB laser cascade to simultaneous multigas sensing by operating the device in a dual wavelength emission regime. The operation to select the desired dual wavelength is simple and straightforward. However a characteristic of operating the SGC laser in a dual wavelength emission mode is the introduction of thermal cross talk between the lasing sections, which complicates somewhat the setting of the emission wavelength of  $S_1$  and  $S_2$ .

Initial measurements described here confirm that SGC lasers developed for telecommunications industry are feasible light sources for sensitive absorption based simultaneous gas detection.

Chapter 6 outlines application of a sampled grating DBR and recently developed MG-Y laser to multi-species gas sensing. The optical characteristics of the MG-Y and SG-DBR have been investigated, tuning ranges of 50 nm have been achieved and look-up tables, which yield high wavelength accuracy and high SMSR across the tuning range, have been generated. For both lasers a SMSR between 35-45dB is obtained. Irregularities in the wavelength tuning are observed at certain regions. These observations indicate that mode hops occur and it is therefore difficult to tune the laser to these particular modes. In between these mode hops the laser tunes continuously and performs similarly to single-section DFB. Simultaneous multi-species gas sensing of hydrogen cyanide, acetylene and ammonia with a SG-DBR and MG-Y laser to selectively detect three gases with overlapping absorption bands. This measurement is among the first demonstration of simultaneous detection of multiple species using a multi-section, injection current tuned MG-Y laser and is a promising demonstration of the eventual power of these lasers. As this MG-Y laser was one of the first batch of MG-Y lasers recently manufactured, it can be expected that their operational characteristics will improve with time as manufacturing techniques mature.

A technique using multiple reference gases for wavelength characterisation and monitoring of a SG-DBR has been demonstrated. This method requires measurements of the gas absorption lines, an etalon trace and comparing the separations between gas absorption lines and the separations from a database (HITRAN) to determine the emission wavelength of the SGDBR. Further work is required to optimise the line



identification algorithm by including the relative amplitude separations; linestrength information was unavailable for the acetylene molecule in the 1.5 $\mu$ m region. This extra information will improve the segment identification greatly.

## 7.2 Suggestions for Further Work

The areas of potential future work fall into the following categories,

1. It will be interesting to see the effect of optimising the line identification algorithm by including the relative amplitude separations. This extra information will significantly improve the accuracy of the program in identifying gas absorption lines and thus providing wavelength identifiers to monitor the emission wavelength of the laser.
2. Investigations into the use of a gas absorption line to act as a FM discriminator. The purpose of an optical FM discriminator is to convert optical fluctuations into intensity variations that can then be measured directly. The laser emission is directed through the gas cell and the laser frequency is set to the side of the gas line, FM variations are converted to amplitude variations in absorption/transmitted signal. A conversion is performed to relate the intensity modulation back to FM. The interpretation of the data will be more difficult and a knowledge of the precise spectroscopic parameters for the individual line will be required.
3. The linestrength of an absorption transition is a key parameter for designing absorption based gas sensors. Though published linestrengths are available for many molecules in the 1.5 $\mu$ m region [3, 4], there are still a considerable number of molecules where no linestrength information is available or are often based on calculations or low-resolution measurements. Thus, high-resolution tuneable laser diodes can be used to improve linestrength estimates. Measuring the linestrength for the acetylene absorption lines in the 1.5 $\mu$ m region, will be valuable for extending the line identification program by allowing inclusion of the relative amplitude variations.

It is clear that gas sensors using laser diodes have indeed a bright future. For species, requiring high sensitivity, mid-infrared lasers will continue to provide a highly specific device to meet the requirements of current and future measurement



challenges. Rapid progress has been reported recently at a TDLAS conference on the applications of quantum cascade lasers in gas sensing applications. Quantum cascade lasers offer the prospect of wide tuning, narrow linewidth, higher cw-power, and room temperature operation. QC-DFB lasers have been reported for various wavelengths between 5.2 and 16  $\mu\text{m}$  and have already been used to study gases [5]. Optical sensors will continue to benefit from success in this area as the available QC-DFB wavelength range expands to cover an increasing number of trace gases.

## 7.3 References

- [1] P. Werle, "A review of recent advances in semiconductor laser based gas monitors," *Spectrochimica Acta Part a-Molecular and Biomolecular Spectroscopy*, vol. 54, pp. 197-236, 1998.
- [2] L. A. Coldren, G. A. Fish, Y. Akulova, J. S. Barton, L. Johansson, and C. W. Coldren, "Tunable semiconductor lasers: a tutorial," *Lightwave Technology, Journal of*, vol. 22, pp. 193-202, 2004.
- [3] N. Jacquinet-Husson, E. Arie, J. Ballard, A. Barbe, G. Bjoraker, B. Bonnet, L. R. Brown, C. Camy-Peyret, J. P. Champion, A. Chedin, A. Chursin, C. Clerbaux, G. Duxbury, J. M. Flaud, N. Fourrie, A. Fayt, G. Graner, R. Gamache, A. Goldman, V. Golovko, G. Guelachvili, J. M. Hartmann, J. C. Hilico, J. Hillman, G. Lefevre, E. Lellouch, S. N. Mikhailenko, O. V. Naumenko, V. Nemtchinov, D. A. Newnham, A. Nikitin, J. Orphal, A. Perrin, D. C. Reuter, C. P. Rinsland, L. Rosenmann, L. S. Rothman, N. A. Scott, J. Selby, L. N. Sinitza, J. M. Sirota, A. M. Smith, K. M. Smith, V. G. Tyuterev, R. H. Tipping, S. Urban, P. Varanasi, and M. Weber, "The 1997 spectroscopic GEISA databank," *Journal of Quantitative Spectroscopy & Radiative Transfer*, vol. 62, pp. 205-254, 1999.
- [4] L. S. Rothman, A. Barbe, D. C. Benner, L. R. Brown, C. Camy-Peyret, M. R. Carleer, K. Chance, C. Clerbaux, V. Dana, V. M. Devi, A. Fayt, J. M. Flaud, R. R. Gamache, A. Goldman, D. Jacquemart, K. W. Jucks, W. J. Lafferty, J. Y. Mandin, S. T. Massie, V. Nemtchinov, D. A. Newnham, A. Perrin, C. P. Rinsland, J. Schroeder, K. M. Smith, M. A. H. Smith, K. Tang, R. A. Toth, J. Vander Auwera, P. Varanasi, and K. Yoshino, "The HITRAN molecular spectroscopic database: edition of 2000 including updates through 2001," *Journal of Quantitative Spectroscopy & Radiative Transfer*, vol. 82, pp. 5-44, 2003.
- [5] K. Namjou, S. Cai, E. A. Whittaker, J. Faist, C. Gmachl, F. Capasso, D. L. Sivco, and A. Y. Cho, "Sensitive absorption spectroscopy with a room-temperature distributed-feedback quantum-cascade laser," *Optics Letters*, vol. 23, pp. 219-221, 1998.